Computational studies of two-dimensional crystals

Thesis presented by

WENDEL SILVA PAZ

for the degree of Doctor in Physics

DEPARTAMENTO DE FÍSICA DE LA MATERIA CONDENSADA
FACULTAD DE CIENCIAS
UNIVERSIDAD AUTÓNOMA DE MADRID

TESIS DOCTORAL

THESIS SUPERVISOR: JUAN JOSÉ PALACIOS

MADRID, 2017

Estudio Computacional de Cristales Bidimensionales

Tesis presentada por

WENDEL SILVA PAZ

para optar al grado de doctor en Ciencias Físicas

DEPARTAMENTO DE FÍSICA DE LA MATERIA CONDENSADA
FACULTAD DE CIENCIAS
UNIVERSIDAD AUTÓNOMA DE MADRID

TESIS DOCTORAL

DIRECTOR DE TESIS: JUAN JOSÉ PALACIOS

MADRID, 2017

Abstract

Nanoscale materials have become a field of high interest in research not only from a fundamental point of view, but also due to the potential of these materials in applied electronics, optoelectronics and spintronics. The present thesis is focused on the study of some of the most promising 2D materials. The research is conducted from an theoretical point of view. However, along the whole thesis we have been supported by experimental colaborations, which have allowed us to get a better comprehension of our results, enriching our understanding of the physics behind.

Semiconductors of atomically thick monolayers, which can be combined to create van der Waals heterostructures where monolayers of multiple 2D materials are stacked vertically layer-by-layer, can also be stitched together seamlessly in-plane to form lateral heterojunctions. Lateral interfacing of atomic monolayers has opened up unprecedented opportunities to engineer two-dimensional heteromaterials. Yet, little is known about the nature of these newly created interfaces. Here we turn our attention to, arguably, the most promising 2D crystal to date, a single layer of MoS_2. In this thesis, we present a theoretical study of the electrical contact between the two most common crystallographic phases of MoS_2 monolayer crystals: 2H (semiconductor) and 1T (metallic).

The fabrication of van der Waals heterostructures, artificial materials assembled by individual stacking of 2D layers, is among the most promising directions in 2D materials research. Until now, the most widespread approach to stack 2D layers relies on deterministic placement methods, which are cumbersome and tend to suffer from poor control over the lattice orientations and the presence of unwanted interlayer adsorbates. Here, we present an extensive theoretical and experimental characterizations of franckeite which is a naturally occurring and air stable van der Waals heterostructure. As the bulk material is already composed of these alternating SnS_2 and PbS layers, the exfoliation process minmizes stacking missorientation and avoids interlayer adsorbates in the isolated nanosheets of franckeite. Hence, franckeite can be considered as a naturally occurring vdW heterostructure analog of its synthetic cousin.

One of the main problems that the scientific community is facing nowadays in nanostructured electronics is the heat dissipation issue that usually leads to device malfunction. Therefore, great efforts are being dedicated to find new materials that could circunvent this problem and to understand the thermal mechanisms working in nanoscale electronics. In this thesis, we investigate the electrical breakdown of TiS_3 nanoribbon-based field-effect transistors (FETs) and the thermal mechanisms that lead to the devices breakdown. Furthermore, these results are compared with thermogravimetric analysis of bulk TiS_3 degradation, as well as with density functional theory and Kinetic Monte Carlo simulations of surface oxidation and the subsequent desorption of sulphur atoms that lead to the creation of defects and could explain the FETs malfunction.

The recent isolation of antimonene, a novel two-dimensional material, pushes even further

the interest for this material which had already been theoretically predicted. Preliminary results on the electronic and electrical properties of few-layer antimonene are presented. Few-layer (> 2 BL) antimonene shows metallic characteristic. In particular, few-layer (> 6 BL) presented the gapless configuration of the surface bands give rise to a single Dirac cone (double degenerate), which is the signature of nontrivial topological order. H_2O molecules on the surface broke the degeneracy of the Dirac cone giving rise to two Dirac cones at the Γ point separated by 60 meV. The experimental electrical properties reported herein are in good agreement with theoretical calculations still ongoing, pointing to a conduction governed by topologically protected surface states in few-layer antimonene.

Resumen

Los materiales a nanoescala se han convertido en un campo de gran interés en la investigación no sólo desde un punto de vista fundamental, sino también debido al potencial de estos materiales en la electrónica aplicada, la optoelectrónica y la espintrónica. La presente tesis se centra en el estudio de algunos de los materiales 2D más prometedores. La investigación se lleva a cabo desde una perspectiva teórica. Sin embargo, a lo largo de toda la tesis hemos sido apoyados por colaboraciones experimentales, que nos han permitido comprender mejor de nuestros resultados, enriqueciendo nuestra comprensión de la física que hay detrás.

Los semiconductores de monocapas atómicamente gruesas, que se pueden combinar para crear heterostructuras de van der Waals, donde las monocapas de múltiples materiales 2D se apilan verticalmente capa por capa, también pueden ser cosidas juntas de forma transparente en el plano para formar heterojunciones laterales. La interfaz lateral de monocapas atómicas ha abierto oportunidades sin precedentes para diseñar heteromateriales bidimensionales. Sin embargo, poco se sabe sobre la naturaleza de estas interfaces recién creadas. Aquí dirigimos nuestra atención a, posiblemente, el más prometedor cristal 2D hasta la fecha, una sola capa de MoS_2. En esta tesis, presentamos un estudio teórico del contacto eléctrico creado entre las dos fases cristalográficas más comunes de los cristales monocapa de MoS_2: 2H (semiconductor) y 1T (metálico).

La fabricación de heterostructuras de van der Waals, materiales artificiales ensamblados por apilamiento individual de capas 2D, está entre las áreas más prometedoras en la investigación de materiales 2D. Hasta ahora, el enfoque más difundido del apilamiento de las capas 2D se basa en métodos de colocación deterministas, que son engorrosos y tienden a sufrir de un control deficiente sobre las orientaciones de la red y la presencia de adsorbidos de intercapa indeseados. Aquí, presentamos extensas caracterizaciones teóricas y experimentales de la Franckeíta que es una heterostructura de van der Waals natural y estable al aire. Como el material a granel ya está compuesto por estas capas alternas de SnS_2 y PbS, el proceso de exfoliación reduce al mínimo la desorientación del apilamiento y evita adsorbatos intercapa y en las monocapas aisladas de la Franckeíta. Por lo tanto, la Franckeíta puede ser considerada como una heteroestructura de van der Waals de origen natural análoga a su primo sintético.

Uno de los principales problemas que enfrenta la comunidad científica hoy en día en electrónica nanoestructurada es el problema de la disipación de calor que suele conducir a un mal funcionamiento del dispositivo. Por lo tanto, se están dedicando grandes esfuerzos a encontrar nuevos materiales que puedan evitar este problema y comprender los mecanismos térmicos que funcionan en la electrónica a nanoescala. En esta tesis, investigamos la descomposición eléctrica de los transistores de efecto de campo (FET) basados en nanocintas de TiS_3 y los mecanismos térmicos que conducen a la avería de los dispositivos. Además, estos resultados se comparan con el análisis termogravimétrico de la estructura granel, así como con los resultados obtenidos a través de la teoría del funcional de la densidad y las simulaciones de Monte Carlo cinético de la

oxidación superficial, y la posterior desorción de átomos de azufre que conducen a la creación de defectos y podrían explicar el mal funcionamiento de los FET.

El reciente aislamiento del Antimoneno, un nuevo material bidimensional, empuja aún más el interés por este material que ya había sido previsto teóricamente. Aquí, presentamos resultados preliminares sobre las propiedades electrónicas y eléctricas del antimoneno de pocas capas. El Antimoneno de pocas capas (> 2 BL) tiene una característica metálica. En particular, el caso (> 6 BL) presentó una configuración sin ranuras de las bandas de superficie dando lugar a un solo cono de Dirac (Doble degenerado), que es la firma del orden topológico no trivial. La presencia de moléculas de H_2O en la superficie rompió la degeneración del cono de Dirac dando lugar a dos conos Dirac en el punto Γ separados por 60 meV. Las propiedades eléctricas experimentales presentadas hasta ahora están en buen acuerdo con los cálculos teóricos aún en curso, apuntando a una conducción regida por estados de superficie topológicamente protegidos en el Antimoneno de pocas capas.

Acknowledgements

The most important influence on the successful completion of this thesis was my advisor, Prof. Juan José Palacios. He has had greatest professional influence on my development as a scientist. He is an amazing scientist and mentor. He pushed me to develop my weaknesses and exploit my strengths. His courage to tackle new and difficult problems and his patience to withstand the many failures that accompany such risks is admirable.

Most importantly, I would like to thank my family for all the support and encouragement during my studies. I want to thank my parents. It is their love and support through the years that brought me to Madrid for proving that there is life and meaning also outside of science.

I would like to thank all collaborators of this work: Aday Molina-mendonza; Pablo Ares and Sahar Pakdel who have been working closely and also for the other collaborators, without her help this study could not be possible. I would like to express my gratitude to the colleagues who helped me a lot during the course of this study: María Soriano, Mohammed, Daniel Bejarano, Manrico and Carlos Salgado.

I am also truly grateful to the Autonomous University of Madrid and like to thank the great support staff and the secretaries that take care of the paperwork and negotiate the grand bureaucracies of the academic world. I would like to the computer resources and assistance provided by the Centro de Computación Científica of the Universidad Autónoma de Madrid and the RES.

I am also thankful to the support from CAPES: Science Without Borders Program, to the Ministry of Education in Brazil, for my scholarship.

Table of Contents

List of Tables

Table **Page**

List of Figures

Figure **Page**

List of Publications in the Period of this Thesis

Part of the contents of this work can be found in the following publications:

Molina-Mendonza, A. J., Giovanelli, E., Paz, Wendel S. *e*t. al., Franckeite as a naturally ocorring van der Waals heterostructure, *Nature Communications*, **8**, 14409 (2017)

Molina-Mendonza, A. J., Island, J. O., Paz, Wendel S. *e*t. al., High Current Density Electrical Breakdown of TiS_3 Nanoribbon-Based Field-Effect Transistors, *Advanced Functional Materials*, **27**(13), 1605647 (2017)

Paz, Wendel S. and Palacios, J. J., A theoretical study of the electrical contact between metallic and semiconducting phases in monolayer MoS_2, *2D Materials*, **4**, 015014 (2016)

Scopel, W. L., Paz, Wendel S. and Freitas, Jair C. C., Interaction between single vacancies in graphene sheet: An ab initio calculation, *Solid State Communications*, **240**, 5-9 (2016)

Freitas, J. C. C., Scopel, W. L., Paz, Wendel S. *e*t. al., Determination of the hyperfine magnetic field in magnetic carbon-based materials: DFT calculations and NMR experiments, *Scientific Reports*, **5**, 14761 (2015)

Preprints

Zhixiang, S., Maldonado, A., Paz, Wendel S., Natalya, Y. Shitsevalova, V. B, Filippov, D. S., Inosov, S, Andreas, P. S., Palacios, J. J. and Peter Wahl, Local Dopping in SmB_6 (2017). (**sent to npj Quantum Materials**)

CHAPTER 1

INTRODUCTION

In 2004, the isolation of graphene, one-atom-thin layer of hexagonally arranged carbon atoms, on an insulating surface [1] gave birth to a new era of atomically thin materials in solid-state electronics, which ultimately led to the search for additional two-dimensional materials[2–6]. These materials have a combination of properties that could make them key enablers for many applications, generating new products that cannot (or may be difficult to) be obtained with current technologies or materials [7]. Moreover, most of the 2D semiconductor families studied so far have also shown interesting phenomena, some of them observed for the first time in these 2D systems [8–11].

One group of such materials is the transition metal dichalcogenides (TMDC's). Unlike graphene, which consists of an individual atom thick layer, TMDC's follow a MX_2 structure, in which M is a transition metal (Mo, W, Re, Nb, etc) and X is a chalcogen atom (S, Se, or Te). Depending on the combination of M and X, the resulting material can vary from semiconducting to metallic and even superconducting [12, 13]. Other semiconducting 2D materials such as silicene [14], germanene [15] and antimonene [16] are also attracting growing interest. The electronic properties of silicene and germanene (the Si and Ge equivalent of graphene) have also been studied theoretically [17] both materials being predicted to be gapless semiconductors with linear energy dispersion relations near the K points, like graphene.

The broad family of layered materials is only so far barely explored and there still exist many members that remain to be investigated [18]. The group IV-V transition metal trichalcogenides (TMTC), for instance, are interesting when compared with the well-studied dichalcogenides (TMDC's) because of their quasi-1D properties stemming from a reduced in-plane structural symmetry. This character gives the TMTC class of materials strong anisotropies in their electrical and optical properties [19–21]. This anisotropy lends an additional degree of freedom in the

fabrication of next generation electronics such as high mobility transistors benefiting from reduced backscattering from hot electrons [22] and novel integrated digital inverters [23]. Titanium trisulfide (TiS_3), in particular, has gained recent attention as it presents a robust direct band gap of ~ 1 eV [24–26] which varies little with layer thickness or stacking order [25].

Table 1.1: Summary of properties of different 2D materials relevant for nanodevices applications.

2D Materials	**Crystal class**	**Electronic structure**	**Bandgap (eV)**	**Mobility (cm^2V^{-1} s^{-1})**
Graphene	Hexagonal	Semimetal	NA	2,000-5,000 (supported)[8] 200,000 (freestanding)[27]
TMDCs (MoS_2)	Hexagonal	Semiconductor	From 1.29 for bulk (indirect) to 1.96 for monolayer (direct)[28]	< 320 for electrons, < 270 for holes [29]
Phosphorene	Orthorhombic	Semiconductor	From 0.3 for bulk (direct) to 1.75 for monolayer (direct)	<10,000-26,000 (monolayer) [30] 400-4,000 (few-layer) [30]
h-BN	Hexagonal	insulator	5.971 (direct)[31]	NA
Silicene	Hexagonal	Semiconductor	0.002 [32]	100 [33]
Antimonene	Hexagonal	Semiconductor	1.6 [16]	800 (value obtained in this work)
Germanene	Hexagonal	Semiconductor	0.003 [32]	

The absence of an energy bandgap makes graphene less desirable for use in FET's switching settings that require high on-state currents but low off-state currents. Hence, the field has expanded into other 2D materials, predominantly semiconducting TMDC's because they possess bandgaps in the range of 1-2 eV, leading to a high degree of electrostatic control [34] and scalability for nanoscale transistors [35], exquisite sensing capabilities [36], high breakdown voltages [37], tunable optical properties [9, 38], a high degree of mechanical flexibility [39] and the possibility of engineering new materials through the realization of van der Waals heterostructures [40]. Many of these results indicate that these crystals give promising perspectives to the next-generation nanoelectronics, spintronics and valleytronics. Yet, still this research area encourages unceasingly wide exploration of TMDC's crytstals' properties and establishes strong motivation for further studies in this matter.

So far, more than ten different 2D semiconductors (with bandgap values spanning from a few millielectronvolts up to several electronvolts) (see Table 1.1) have been experimentally isolated and there are potentially hundreds more that could be isolated in the near future. Because of this broad catalogue of materials, it is always possible to find a 2D semiconductor that is optimal for a certain application. Table 1.1 shows a comparison of some relevant properties of the most studied 2D materials. Moreover, most of the 2D semiconductor families studied so far have also shown interesting phenomena, some of them observed for the first time in these 2D systems.

These recent progress suggests that such atomically thin 2D materials could be one pathway for electronic devices in the future [12, 41, 42].

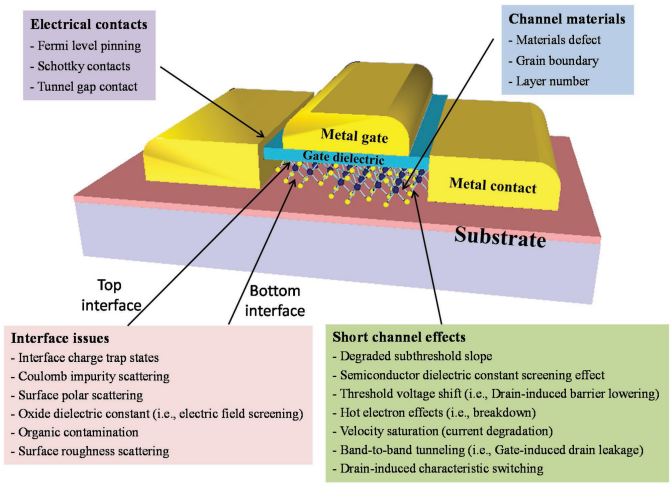

Figure 1.1: Schematic of a typical 2D semiconductor FET. The figure states key issues affecting 2D device performance related to channel materials, metal contact, 2D dielectric interfaces, and short channel effects. (extracted from [43]).

Figure 1.1 illustrates the key issues observed in a typical 2D semiconductor FET. These issues are arranged into four main categories: quality of channel materials, metal contacts, interfacial effects, and short channel effects. Although many of these issues are observed in traditional bulk semiconductor devices, the severity and impact of these issues on the device performance are expected to be different in the case of 2D semiconductors. For instance, because electrons in a 2D FET are confined in close proximity to the gate dielectric and substrate interfaces, the effects of interfacial scattering are more severe in comparison with traditional FETs made of bulk semiconductors. Moreover, there are some differences in the device structure and fabrication processes between 2D FETs and traditional FETs. For example, in most 2D FETs, the source/drain metal contacts the 2D semiconductors directly. On the other hand, highly doped source/drain regions are formed before metal contacts in traditional FETs. As a result, it is important to understand and solve major problems with 2D FETs in unique ways, so that optimized device performance may be achieved.

1.1 Electrical contacts to 2D materials

Making excellent electrical contacts is a prerequisite to obtain high performance for any of the 2D devices. The quality of the electrical contacts - quantified through contact resistance - is a critical issue for many electronic and optoelectronic devices. Their ultrathin nature and inert smooth surface make it difficult. In short-channel devices, the relative contribution of contact

resistance to the whole device resistance will increase when compared to long-channel devices, and eventually contact may even dominate the performance of the whole device.

Therefore, it is critical to achieve low-resistance contacts to 2D semiconductors. However, it is quite a challenge to achieve good contact for 2D semiconductors for the following reasons. First, the pristine surface of 2D materials is usually intact, without unsaturated atoms, which makes it difficult for them to form strong interface bonds with contact metals, leading to an increased contact resistance. Second, the commonly used approach to decrease contact resistance in silicon and III-V semiconductor electronics is degenerate substitutional doping. This doping technique is difficult to apply to 2D semiconductors because it will inevitably modify the properties of the 2D semiconductor channels, due to the ultrathin 2D-semiconductor body. Third, the contact areas between 2D semiconductors and contact electrodes are usually small, especially for small-dimension devices, which results in large contact resistance. In the past several years, researchers have developed several strategies aimed at improving the contacts in 2D semiconductor electronics (Figure 1.2).

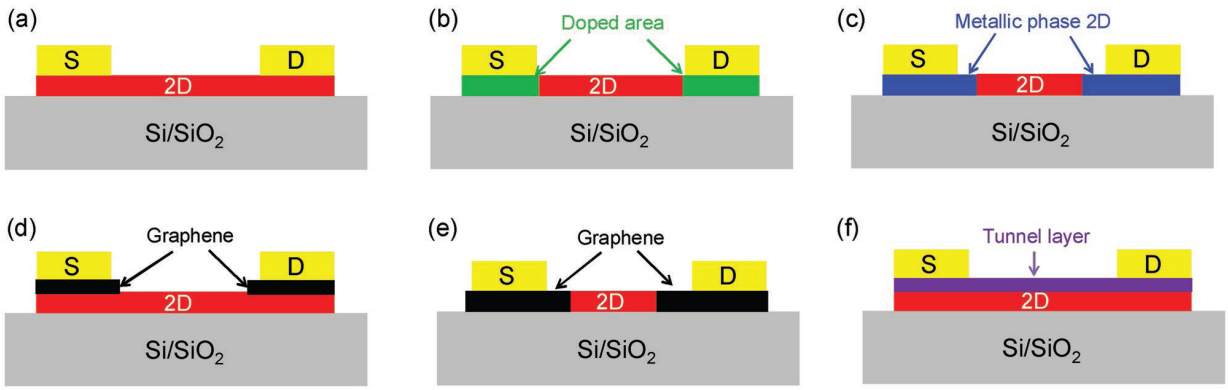

Figure 1.2: Current strategies to improve electrical contacts in 2D semiconductor FETs. a) Play with types of contact metals and processing recipe. b) Doping of contact areas. c) 1T-2H phase-engineered in-plane heterojunctions. d) Graphene top contact. e) Graphene edge contact. f) Inserting a tunnel layer between 2D semiconductors and contact electrodes. (extracted from [43]).

Figure 1.2(a) shows a typical structure of a back-gated FET using 2D semiconductors as channel materials, which are electrically contacted by two contact electrodes (i.e., source (S) and drain (D)). The second approach to reduce Rc is to dope the contact area, as shown in Figure 1.2(b). Figure 1.2(c) shows another approach to achieve low R_c contact in TMDC transistors, i.e., formation of 1T/2H phase junctions. TMDCs have different phases, for example, 1T and 2H, which possess distinct properties. For example, 2H-phase WSe_2 and MoS_2 are semiconductors, while metastable 1T-phase WSe_2 and MoS_2 are metals. It has been noted that 1T and 2H phases have reasonably similar structures and lattice constants, and can transform to each other reversibly. Finally, using graphene is another effective approach to achieve good contacts to 2D

semiconductors. There are two kinds of graphene based contacts, i.e., top contact (Figure 1.2(d)) and edge contact (Figure 1.2(e)).

1.1.1 Lateral heterostructures

Heterojunctions between three-dimensional (3D) semiconductors with different bandgaps are the basis of modern light-emitting diodes [44], diode lasers [45] and high-speed transistors [46]. Creating analogous heterojunctions between different 2D semiconductors would enable band engineering within the 2D plane [6, 47–49] and open up new realms in materials science, device physics and engineering.

Lateral heterostructures can also be grown by a variety of methods. Thus, CVD-grown graphene was lithographically patterned and etched away, and h-BN was grown via CVD, forming lateral 1D heterojunctions. Beyond graphene and h-BN, lateral heterostructures based on 2D TMDCs can be disruptive for integrated optoelectronic devices. Although direct growth favors TMDC alloys because of a similar chemistry and a small lattice mismatch between different TMDCs [50], two-step epitaxial growth. The growth of such lateral junctions will allow new device functionalities, such as in-plane transistors and diodes, to be integrated within a single atomically thin layer.

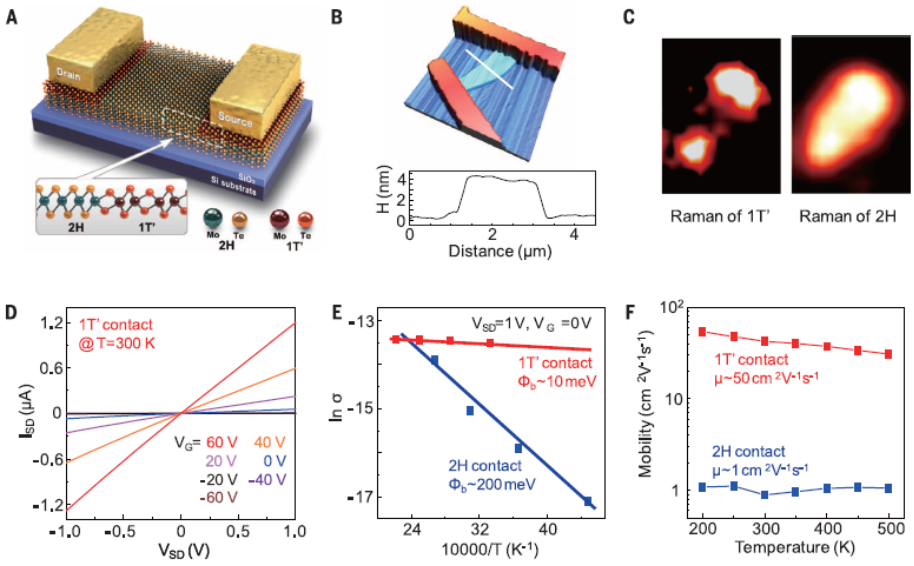

Figure 1.3: Schematic diagrams of a device with a 1T'/2H phase homojunction. (B) AFM image of a device with the 1T'/2H phase homojunction in MoTe2. (C) Raman mapping images of 1T' (A_g) and 2H(E_{2g}) vibrational modes in the device channel in (B). (D) Source-drain current I_{SD} characteristics for gate voltage V_G ranging from -60 V to 60 V. (E) Arrhenius plots of the conductance. (F) Field-effectmobility as a function of temperature (extracted from [51]).

Most of transition metal dichalcogenides possess two typical phases, i.e., semiconducting 2H

and metallic 1T (1T') phases. An alternative approach that makes use of the intrinsic metallic behavior of a metastable phase of MoS_2, based on phase engineering, to design low-resistance contacts to realize FETs is demonstrated by Kappera *et. al.* [6] (see Figure 1.2(c)). They locally modified by chemical means the arrangement of S atoms in the crystalline structure of a few layers of semiconducting MoS_2, and then deposited metallic contacts on these converted regions. This decreased the energy barrier between the external circuit and the semiconducting MoS_2 flakes, a marked improvement towards the theoretical minimum contact resistance value of TMDCs (200 - 300 $\Omega\mu$m at zero gate bias). The low contact resistance is attributed to the atomically sharp interface between the phases and to the fact the work function of the 1T phase and the conduction band energy relative to vacuum level of the 2H phase are similar (~ 4.2 eV) [6]. However, the wet chemical method involved in the device-fabrication process may limit its efficient applications. According to this issue, Cho *et al.* [51] developed a laser-irradiation-induced phasetransformation process to fabricate a 1T'/2H $MoTe_2$ ohmic lateral homojunction contact, as shown in Figure 1.3. The 1T'/2H contact increases the carrier mobility over 50 times than the 2H/2H contact.

1.2 van der Waals heterostructures

Once the atomic layers are attained from whichever method best suits the experiment, it is necessary to assemble them into the desired stacking order to create the desired van der Waals heterostructures. Similar to the synthesis of individual layers, both top-down and bottom-up strategies can be applied to heterostructure assembly [7, 40]. Semiconducting TMDC's could be combined with graphene, h-BN, or other 2D materials, and form hybrid all-2D electronics on flexible substrates [40]. These architectures have already been realized by mechanically transferring one monolayer on top of another. However, the artificial fabrication of van der Waals heterostructures also has major limitations; first, there is little control over crystal orientation while stacking on top of each other and second, the sample can suffer damage by unwanted air bubbles or adsorbates between the stacked layers. Moreover, large scale isolation methods lique chemical or liquid phase exfoliations have problems to provide suspensions whith platelets consisting of van der Waals heterostructures with high quality.

An alternative technique, which potentially allows mass production of such structures (i.e., sequential growth of monolayers) comes with its own limitations and is presently in its infancy. Nevertheless, a large variety of novel experiments and prototypes have already been carried out with van der Waals heterostructures, which indicates that these materials are versatile and practical tools for future experiments and applications.

In this thesis, we present an extensive theoretical and experimental characterizations of franckeite which is a naturally occurring and air stable van der Waals heterostructure. Thin layers of heterostructures based on alternating layers of SnS_2-based and PbS-based 2D layers

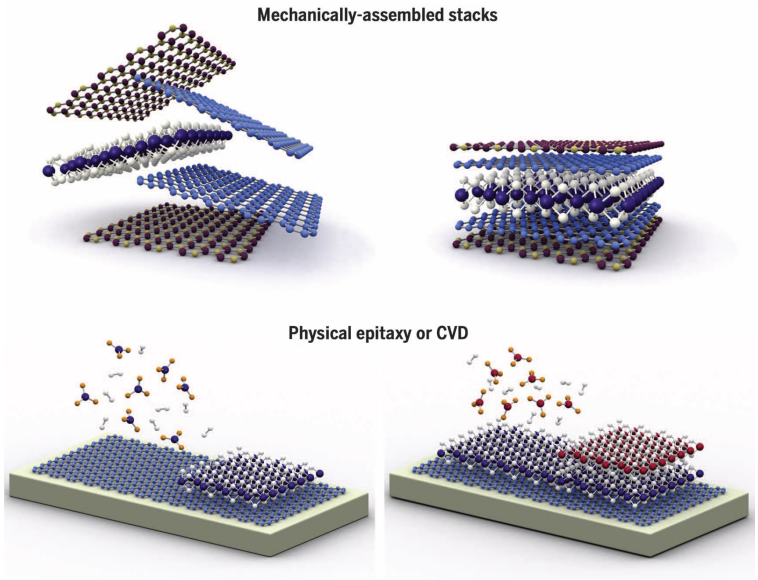

Figure 1.4: Many functional van der Waals heterostructures can be created. What started with mechanically assembled stacks (top) has now evolved to large-scale growth by CVD or physical epitaxy (bottom) (extracted from [52]).

(with remarkably high crystalline and stacking order) by mechanical and liquid phase exfoliation were isolated. As the bulk material is already composed of these alternating SnS_2 and PbS layers, the exfoliation process minimizes stacking missorientation and avoids interlayer adsorbates in the isolated nanosheets of franckeite [53]. Hence, franckeite can be considered as a naturally occurring vdW heterostructure analog of its synthetic cousin.

1.3 New promising 2D materials

1.3.1 Germanene

Graphene's success has shown not only that it is possible to create stable, single-atom-thick sheets from a crystalline solid but that these materials have fundamentally different properties than the parent material. Other group IV layered lattices may maintain appreciable conductivity when the atoms are in the sp^3 hybridized state. Recently, single-layer-thick sp^2 and sp^3 group IV systems have attracted considerable theoretical and experimental interest [54, 55].

The most obvious alternatives for graphene are the group IV elements, i.e. silicon and germanium [56]. The electron configurations of germanium, silicon and carbon are very similar since all three elements have four electrons in their outermost s and p orbitals. The energetically most favourable crystal structure of silicon and germanium is the diamond structure [57]. The diamond lattice consists of two interpenetrating fcc sub-lattices and each atom of these fcc sub-lattices is surrounded by four neighbours. The covalent bonds between the atoms are all

equivalent and have a hybridized s, p_x, p_y, p_z character (sp^3). The first reports on the synthesis of silicene date back to 2010 [58, 59], followed by germanene in 2014 [15, 32, 55].

Free standing germanene does not exist, but it is predicted to be a buckled honeycomb 2D Dirac material [17] with extremely high mobilities of its charge carriers [60]. The spin-orbit coupling along with the ~ 0.64 Å buckling opens up a ~ 24 meV band gap at the Dirac points significantly higher than in silicene (1.55 meV); this, together with the non-trivial topological properties, might result in a quantum spin Hall effect detectable at room temperature [61]. Typically, since germanium is currently used as a performance booster in thin FET channels, perspectives of using germanene for scaling down beyond the 5 nm node while increasing the speed and lowering the energy consumption of electronic devices appear very promising.

1.3.2 Antimonene

The 2D materials of group V elements are gaining considerable interest because of the unique properties. In the last two years phosphorene has generated a considerable attention due to the fact that, as a function of the number of layers, it features a direct optical band gap in the range 0.5-1.8 eV, suitable for THz optoelectronic applications [10, 62]. However, its ambient stability represents a major drawback for the development of the real applications [63]. In contrast, a member of the group V in the periodic table, antimonene, i.e. a single layer of antimony, presents an outstanding stability under ambient conditions [16].

In a recent study, Ares *et. al.* reported both micromechanical exfoliation of antimony down to the single-layer regime and experimental evidence of its stability. They demonstrated that single/few-layer antimony flakes are highly stable in ambient conditions showing mechanical stability upon origami nanomanipulation and no degradation over month periods. Density functional theory (DFT) simulations mimicking ambient conditions confirm the geometrical experimental findings and predict a bandgap of 1.2-1.3 eV within the range of optoelectronics applications [16]. They have used optical microscopy used to study the optical properties of few-layer antimonene flakes and quantitatively estimate their thickness in a fast and nondestructive way. Antimonene has been recently isolated by the liquid phase exfoliation [64], that has been successfully applied to generate single- or few-layer (FL) samples of several 2D materials on large scale [65].

These experimental works were preceded by a considerable number of theoretical calculations that predicted extraordinary physical properties for antimonene such as high carrier mobility, thermal conductivity, and strain induced band transition, among others [66–68]. Moreover, the most stable antimonene holds buckled honeycomb structure with much stronger spin-orbital coupling (SOC), which brings exotic fundamental properties for photonics and spintronics. Up to now, theoretical works on antimonene largely exceeds experimental works.

Theoretical works on antimonene have been subdivided into two fronts, quite clearly separated in time (and in researcher communities), and can be found in the literature. The most recent

works (theoretical and experimental) refer to monolayer antimonene (or occasionally bilayer antimonene) and can be found in the context of new 2D crystals [16, 66]. The second one, which goes a few years back in time, refers to few-layer (FL) antimonene (or Sb thin films), and can be found in the context of 3D topological insulators [69]. The physical properties of antimonene change quite drastically from the monolayer to FL systems (these generally considered to be in the range of 10-100 layers) and both deserve a separate discussion.

CHAPTER 2

THEORETICAL BACKGROUND

2.1 Introduction

Quantum mechanical modeling has become an invaluable tool in materials research being, nowadays, the most accurate computational method used for solving emerging problems in materials science, clean energy, nanotechnology, catalysis, etc. Such simulations provide quantitative predictions and also describe the general trends of physical and chemical properties of a broad range of systems. By solving the quantum mechanical equations of a system, we can achieve a greater understanding of a large number of physical phenomena related to the properties of real material systems.

The properties of a quantum mechanical many-body system are calculated from the many-particle Schrödinger equation: $\hat{H}|\alpha\rangle = E_\alpha|\alpha\rangle$, with $\hat{H} = \hat{T} + \hat{V}$, where $\hat{T}$ and $\hat{V}$ are the kinetic energy operator and the potential energy operator for all the particles of the system, respectively. This equation contains the information about the properties of the physical system in question. The degrees of freedom of this problem are the positions and momentums of all the particles. Considering a quantum physical system with Z electrons per atom and N atoms, the position of the particles is describe by $Z \cdot 3N$ variables. Unfortunately, the many-body nature of the Schrödinger equation makes itself extremely difficult to solve and for large N the solution of it becomes impossible. Hence, to avoid insolubility of the Schrödinger equation is necessary some approximations to render the problem soluble (more details in sec. A.1).

In this sense, the density functional theory (DFT) emerged as a powerful tool for electronic structure calculations [70]. DFT reduces (see sec. A.1) the problem of $Z \cdot 3N$ variable to one with only 3. This theory is the base of the *ab initio* calculations and, in principle, provide information only on the ground state of the system. DFT implementations generally exhibit a good balance

between accuracy and computational cost. Despite the intensive software development, the computational cost of *ab-initio* methods still remains very expensive. This originates from the complexity of electrons represented by wave functions, hence possessing an inner structure with widely variable properties compared to simple particles used in classical molecular dynamics. The requirement of self-consistency is only one consequence of the quantum nature, which slows down such methodology. Although many concepts exist to weaken this impact, there is a practical limitation to sizes of systems, at present 1-2 nm, treatable *ab-initio*. This, however, is not the length scale on which one discusses functional materials.

If one is interested in the electronic structure of large systems or if interatomic potentials are not accurate enough for the desired application, one option is to turn to semiempirical methods, which lie conceptually between empirical force fields and first principles methods and allow for the treatment of tens of thousands of atoms. Semiempirical electronic structure methods can be understood as direct approximations to more accurate methods (usually DFT or Hartree-Fock), but additionally include empirical parameters that can be tuned to reproduce reference data (experimental or theoretical). One particular example of a semiempirical method is the tight-binding (TB) electronic structure method.

The tight-binding model is a simple and computationally feasible single-particle model that provides a reasonable description of occupied states in any type of crystal (metals, semiconductors, and insulators) and often also of the lowest lying conduction states [71]. The Hamiltonian matrix is then readily constructed and diagonalized. Tight-binding method is specially relevant in the study of nanoscopic systems, for instance graphene [72, 73], graphene-related materials and nanostructures [74–76] and the transition metal dichalcogenides (TMD) [77–79].

The tight-binding method is an efficient formalism used to create Hamiltonians in localized basis. This Hamiltonian can be used to compute ballistic quantum transport within the coherent transport approximation *i.e* no inelastic events. Landauer formalism and the partitioning scheme require a localized representation of the electronic structure. We have seen that tight-binding is very efficient dealing with big systems. Therefore, with both methodologies it is posible to explore the electronic transport in a great number of systems. In this thesis, we have compute the tight-binding quantum transport, aided by DFT calculations, of the lateral heterostructure formed by two most commom crystallographic phases of MoS_2 monolayer crystals: the stable semiconducting 2H phase and the metastable metallic 1T phase. All the transport calculations have been done using the code **ANT.1D** [80].

Other theoretical method used in this thesis is the technique called "Monte Carlo Simulation" or kinetic Monte Carlo (KMC). KMC algorithms are powerful techniques to study the dynamics of a system of particles when the different events that those particles can perform are known as well as their probabilities [81]. The KMC simulations were employed together with DFT calculations to study the thermal stability and the vacancy generation mechanism of the single layer TiS_3 with differents oxygen concentrations on the surface.

2.2 Tight-binding model

The goal of this section is introduce the basic concepts of the tight-binding model and the terminology and definitions used in this work. The TB model assumes that the electrons are tightly bound to atoms, such that the confining atomic potentials in a crystal are strong. Then, the atomic orbitals of isolated atoms can be used as the single-particle basis, and the tight-binding states are written as linear combinations of them. Moreover, the atomic orbitals of nearby atoms are coupled by small overlaps and tunneling matrix elements that are the relevant parameters of the model.

The starting point for all semi-empirical approaches is the physics. In metals, for example, the electrons are almost free and so we can treat the single particle states in terms of plane waves. We could also take a very different approach and assume the states in a crystal look like combinations of the wavefunctions of isolated atoms. We might imagine this is more likely to be the case in insulators or semiconductors.

2.2.1 Electrons is solids

The motion of electrons moving in a solid is governed by:

$$\hat{H} = \hat{T}_e + \hat{V}_{ee} + \hat{V}_{en}. \tag{2.1}$$

A mean-field approach simplifies the system mapping the N-electron equation to a set of single-electron equations for the motion of an electron in the mean field of the nuclei and the other $N-1$ electrons. We represent the electron-electron and the electron-nuclei interactions with an effective one-electron potential $V(\mathbf{r})$ which has the same periodicity of the lattice

$$V(\mathbf{r}) = V(\mathbf{r}+\mathbf{R}), \tag{2.2}$$

for all Bravais lattice vectors $\mathbf{R}$. In this way, we have to find solutions of a Schrödinger equation of the form

Here, we will solve the single particle Schrödinger equation for the states in a crystal by expanding the Bloch states in terms of a linear combination of atomic orbitals.

2.3 Linear Combination of atomic orbital (LCAO)

2.3.1 Crystal and atomic hamiltonians

In a crystal, we take the single particle hamiltonian to be

$$H = H_{at} + \Delta U \tag{2.3}$$

where H_{at} is the hamiltonian for a single atom and ΔU encodes all the differences between the true potential in the crystal and the potential of an isolated atom. We assume $\Delta U \to 0$ at the center of each atom in the crystal.

The single particle in the crystal are then $\psi_{n\mathbf{k}}(\mathbf{r})$, where

$$H\psi_{nk}(\mathbf{r}) = E_{nk}\psi_{nk}(\mathbf{r}), \tag{2.4}$$

the band index is labelled by n and $\mathbf{k}$ is a wavevector in the first Brillouin zone.

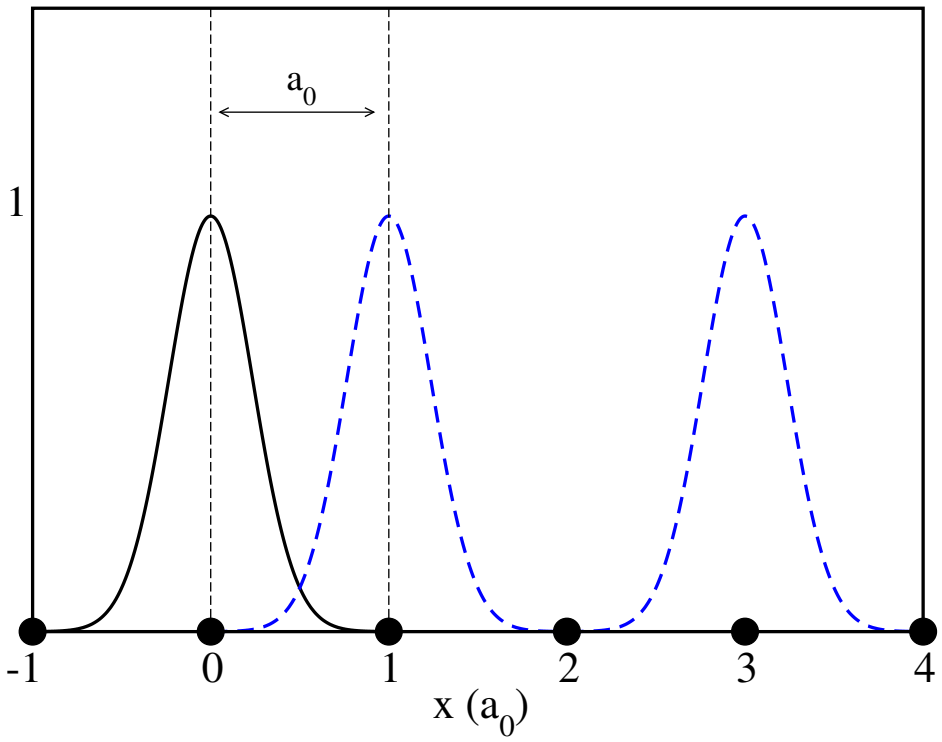

Figure 2.1: Schematic of the atomic orbitals in a 1D crystal with atoms separated by a_0. The translation vectors are $\mathbf{R} = 0, \pm a_0\mathbf{i}, \pm 2a_0\mathbf{i}, \pm 3a_0\mathbf{i}, ...$, where i is a unit vector in the x direction. The vertical dotted lines denote the edges of the unit cell which contains a single atom. The solid curve shows an example atomic orbital centred on an atom at $\mathbf{r} = 0$, while dashed blue lines show orbitals centred on $\mathbf{r} + a_0\mathbf{i}$ and $\mathbf{r} + 3a_0\mathbf{i}$. The orbitals decay rapidly so the overlap, $\phi_i^*(\mathbf{r})\phi_i(\mathbf{r}+R)$, is small.

2.3.2 The atomic wavefunctions

The atomic wavefunctions, $\phi_i(r)$ are eigenstates of H_{at},

$$H_{at}\phi_i(r) = \epsilon_i\phi_i(r) \tag{2.5}$$

where ϵ_i is the energy of the i energy level in an isolated atom. These wavefunctions decay rapidly away from r = 0 and so the *overlap* integral, $\gamma(|\,\mathbf{R}\,|) = \int \phi_i^*(\mathbf{r})H\phi_i(\mathbf{r}+\mathbf{R})d(\mathbf{r})$, between wavefunctions located on separate atomic sites (R ≠ 0) in the crystal is small (see Fig. 2.3.1).

Throughout these notes we will use orthonormal atomic orbitals that have zero direct overlap between dierent lattice sites,

$$\int \phi_i^*(\mathbf{r})\phi_i(\mathbf{r}+\mathbf{R})d(\mathbf{r}) = \begin{cases} 1 & \text{if i = j} \quad \text{and} \quad \mathbf{R} = 0 \\ 0 & \text{otherwise} \end{cases}$$

This gives a simple orthogonal tight-binding formalism but it is relatively easy to generalise from this to more complex forms.

2.3.3 Bloch's theorem

The single particle states must obey Bloch's theorem,

$$\psi_{n\mathbf{k}}(\mathbf{r}+\mathbf{R}) = e^{ik\cdot\mathbf{R}}\psi_{n\mathbf{k}}(\mathbf{r}), \tag{2.6}$$

where $\mathbf{R}$ is a real space translation vector of the crystal.

Clearly, a single atomic orbital does not satisfy Bloch's theorem, but we can easily make a linear combination of atomic orbitals that does,

$$\psi_{n\mathbf{k}} = \frac{1}{\sqrt{N}}\sum_{\mathbf{R}} e^{ik\cdot\mathbf{R}}\phi(\mathbf{r}-\mathbf{R}) \tag{2.7}$$

where there are N lattice sites in the crystal and the factor of $1/\sqrt{N}$ ensures the Bloch state is normalised.

2.3.3.1 Proof that $\sum_{\mathbf{R}} e^{ik\cdot\mathbf{R}}\phi(\mathbf{r}-\mathbf{R})$ satisfies Bloch's theorem

If **R'** is a real space translation vector and $\psi_{n\mathbf{k}}(\mathbf{r}) = \sum_{\mathbf{R}} e^{ik\cdot\mathbf{R}}\phi(\mathbf{r}-(\mathbf{R})$ then,

$$\psi_{n\mathbf{k}}(\mathbf{r}+\mathbf{R}') = \frac{1}{\sqrt{N}}\sum_{\mathbf{R}} e^{ik\cdot\mathbf{R}}\phi_n(\mathbf{r}-(\mathbf{R}-\mathbf{R'})) \tag{2.8}$$

But, $\mathbf{R}-\mathbf{R} = \mathbf{R}''$ is simply another crystal translation vector and, because the sum over $\mathbf{R}$ goes over all of the translation vectors in the crystal, we can replace it by another equivalent translation vector, **R"**. Then, substituting for $\mathbf{R} = \mathbf{R}' + \mathbf{R}''$ in the complex exponential we have

$$\begin{aligned}
\psi_{n\mathbf{k}}(\mathbf{r}+\mathbf{R}') &= \frac{1}{\sqrt{N}}\sum_{\mathbf{R}} e^{i\mathbf{k}\cdot(\mathbf{R}'+\mathbf{R}'')}\phi_n(\mathbf{r}-\mathbf{R}''), \\
&= e^{i\mathbf{k}\cdot\mathbf{R}'}\frac{1}{\sqrt{N}}\sum_{\mathbf{R}} e^{i\mathbf{k}\cdot\mathbf{R}''}\phi_n(\mathbf{r}-\mathbf{R}''), \\
&= e^{i\mathbf{k}\cdot\mathbf{R}'}\psi_{n\mathbf{k}}(\mathbf{r}).
\end{aligned}$$

In order to classify the atomic orbitals of the whole crystal we need to especify three indexes: $\mathbf{R}$, the lattice vector that determines the unit cell in the crystal; r_i, the atom place in the position r and o, the corresponding orbital of each atom. We label which atomic orbital with these three indices, $|\mathbf{R}, i, o\rangle$.

A general state, $|\alpha\rangle$, that describes an electron in a crystal, can be expressed as the linear combination of all the atomic orbitals of the crystal

$$|\alpha\rangle = \sum_{\mathbf{R},i,o} c^{\alpha}_{i,o}(\mathbf{R})|\mathbf{R}, i, o\rangle. \tag{2.9}$$

Using Bloch theorem we can show that the coefficients $c^{\alpha}_{i,o}$, are related to the coefficients of a reference unit cell, $\mathbf{R} = 0$ by a Bloch phase factor

$$c^{\alpha}_{i,o}(\mathbf{R}) = e^{i\mathbf{k}\cdot\mathbf{R}} c^{\alpha}_{i,o}(\mathbf{0}). \tag{2.10}$$

Combining (2.3.3.1) and (2.3.3.1) into the single-particle Schrödinger equation

$$\hat{H}^{sp}|\alpha\rangle = \epsilon^{\alpha}|\alpha\rangle \tag{2.11}$$

$$\hat{H}^{sp}\left[\sum_{\mathbf{R}',i',o'} c^{\alpha}_{i',o'} e^{i\mathbf{k}\cdot\mathbf{R}'}(\mathbf{0})|\mathbf{R}',i',o'\rangle\right] = \epsilon^{\alpha}\left[\sum_{\mathbf{R}'',i'',o''} c^{\alpha}_{i'',o''}()e^{i\mathbf{k}\cdot\mathbf{R}''}(\mathbf{0})|\mathbf{R}'',i'',o''\rangle\right] \tag{2.12}$$

If we project over the bra state of the basis set $\langle\mathbf{R},\alpha,o$, we obtain

$$\sum_{\mathbf{R}',i',o'} c^{\alpha}_{i',o'}(\mathbf{0}) e^{i\mathbf{k}\cdot\mathbf{R}'}\langle\mathbf{R},i,o|\hat{H}|\mathbf{R}',i',o'\rangle = E^{\alpha} c^{\alpha}_{i'',o''}(\mathbf{0}) e^{i\mathbf{k}\cdot\mathbf{R}} \tag{2.13}$$

where $\langle\mathbf{R},i,o|\hat{H}|\mathbf{R}',i',o'\rangle$ is the Hamiltonian matrix element between two different atomic orbitals. Since each unit cell is equivalent to the others, we can set $\mathbf{R} = \mathbf{0}$, which, without loss of generality can be placed in any unit cell. Hence, the Schrödinger equation in a crystal reads

$$\sum_{\mathbf{R}',i',o'} c^{\alpha}_{a',o'}(\mathbf{0}) e^{i\mathbf{k}\cdot\mathbf{R}'}\langle\mathbf{0},a,o|\hat{H}|\mathbf{R}',a',o'\rangle = E^{\alpha} c^{\alpha}_{a'',o''}(\mathbf{0}) \tag{2.14}$$

defining the matrix $H_R = \langle\mathbf{0},i,o|\hat{H}|\mathbf{R}',i',o'\rangle$ that describes the coupling between different unit cells in the crystal, and ψ^{α} the column vector of coefficients $c^{\alpha}_{i,o}$, we can rewrite the equation (2.3.3.1) in a compact form as

$$\left[\sum_{\mathbf{R}} e^{i\mathbf{k}\cdot\mathbf{R}} H_{\mathbf{R}}\right]\phi^{\alpha} = \epsilon^{\alpha}\phi^{\alpha} \tag{2.15}$$

This equation shows how powerful Bloch theorem is. We have reduced the infinity eigenvalue problem to an infinite sum of finite matrices. The sum of matrices $\sum_{\mathbf{R}} e^{i\mathbf{k}\cdot\mathbf{R}} H_{\mathbf{R}}$, is usually called the Bloch Hamiltonian, $H(\mathbf{k})$. Notice that the label α stands for, $\mathbf{k}$, the wave vector, and n, the band index. Finally, the Schrödinger equation of a crystal can be written in momentum space as:

$$H(\mathbf{k})\phi^{n}(\mathbf{k}) = \epsilon^{n}(\mathbf{k})\phi^{n}(\mathbf{k}) \tag{2.16}$$

Therefore, we can define a set of n eigenvalues at each $\mathbf{k}$ solving equation (2.3.3.1), in this way we can obtain the band structure of the crystal maaping the whole Brillouin zone.

2.4 The Slater-Koster approximation

In order to solve the Schrödinger equation, it is necessary to evaluate all the matrix elements in the atomic orbitals basis set, $\langle a,o|\hat{H}|a',o'\rangle = \int \psi_0(\mathbf{r}-\tau_a)^* \hat{H}\psi_0(\mathbf{r}-\tau_{a'})d\mathbf{r}$. Tight Binding

parametrizes these elements and do not compute them directly, but they are chosen to fit experiments or *ab-initio* calculations. However, it is not useful to have a theory with such amount of parameters. It is possible to reduce the number of parameters taking into account the symmetries of the atomic orbitals. J. C. Slater and G. F. Koster [82] showed that it is possible to reduce drastically the number od parameters neglecting the three-center interactions. In this section we describe the Slater-Koster approximation and give explicit expressions to evaluate the matrix elements among different atomic orbitals.

The first step in the Slater-Koster approximation is to consider the effective potential $\hat{V}^{eff}$ as a sum of the atomic potentials centred on each atom

$$\hat{V}^{eff}(\mathbf{r},\tau_i) = \sum_i U(\mathbf{r}-\tau) \tag{2.17}$$

Then, the single-particle Hamiltonian can be divided in two terms

$$\begin{aligned} \hat{H}^{sp} &= -\frac{\hbar}{2m}\nabla^2 + \sum_i U(\mathbf{r}-\tau) && (2.18)\\ &= \left(-\frac{\hbar}{2m}\nabla^2 + U(\mathbf{r}-\tau_a)\right) + \left(\sum_{i\neq a} U(\mathbf{r}-\tau_i)\right) && (2.19)\\ &= \hat{H}_0 + \hat{H}' && (2.20) \end{aligned}$$

Where, $\hat{H}_0$ is the single-particle Hamiltonian of the isolated j atom and $\hat{H}'$ the difference between the real potential of the crystal and the isolated atomic potential of site j. The representation of the matrix elements of both contributions in the real vector space are

$$\begin{aligned} \langle a,o \mid \hat{H}_0 \mid a',o'\rangle &= \int \psi_0(\mathbf{r}-\tau_a)^* \hat{H}_0 \psi_0(\mathbf{r}-\tau_{a'}) d\mathbf{r} && (2.21)\\ \langle a,o \mid \hat{H}' \mid a',o'\rangle &= \int \psi_0(\mathbf{r}-\tau_a)^* \hat{H}' \psi_0(\mathbf{r}-\tau_{a'}) d\mathbf{r} && (2.22) \end{aligned}$$

To evaluate the first equation is trivial using the Schrödinger equation

$$\langle a,o \mid \hat{H}_0 \mid a',o'\rangle = \epsilon_{a',o'}\gamma_{ao,a'o'} \tag{2.23}$$

where $\epsilon_{a',o'}$ is the energy of the atomic orbital o'. Thus, the diagonal elements of the Hamiltonian matrix are on-site energies of the atomic orbitals, which will be considered as parameters. These kind of therms are call one-center integrals because both, the atomic orbitals and potential energy, are evaluated in same atom.

The second term of (2.4) give rise to two-center integrals.

$$\langle a,o \mid \hat{H}' \mid a',o'\rangle = \int \psi_0(\mathbf{r}-\tau_a)^* \sum_{a''\neq a'} U(\mathbf{r}-\tau_{a'})\psi_0(\mathbf{r}-\tau_{a'}) d\mathbf{r} \tag{2.24}$$

Firstly, we consider two-center integrals. We can distinguish two types. On the one hand intra-atomic matrix elements ($a = a'$)

$$\langle a,o \mid \hat{H}' \mid a,o'\rangle = \int \psi_0(\mathbf{r}-\tau_a)^* \sum_{a''\neq a'} U(\mathbf{r}-\tau_{a''})\psi_0(\mathbf{r}-\tau_{a'}) d\mathbf{r} \tag{2.25}$$

They are two-center integrals because both orbitals are placed in the same atom a, while the potential is evaluated in a different atom $a'' \neq a$. These elements are known as crystal field integrals, they introduce the effects od the crystal enviroment, and break the degeneracy of the atomic orbitals with the same orbital quantum number. In our calculations, we neglect this kind of coupling.

On the other hand, the second type of two-center integrals are:

$$\langle a,o \mid \hat{H}' \mid a',o' \rangle = \int \psi_0(\mathbf{r}-\tau_a)^* U(\mathbf{r}-\tau_a)\psi_0(\mathbf{r}-\tau_{a'})d\mathbf{r} \tag{2.26}$$

These matrix elements give the probability that one electron in atom a may jump to other atom a', mediated only by the atomic potential of these two atoms. This kind of integrals are usually called hopping integrals.

In transport calculations, the inclusion of higher neighbour hopping terms implies in an increase in the size of the unit cell. Hence, trading a larger number of bands with nearest-neighbour hopping for a simpler model with longer range hopping is not necessarily advantageous.

Finally, the three-center integrals are those where $a \neq a' \neq a''$. They also compute the transition amplitude of jump from a site a to a' but mediated by the atomic potentials located in different site of lattice. Normally, these integrals are small compared with the two-center integrals.

In the Slater-Koster approximation, three-center integrals are neglected. Thus, in this approximation, when we evaluate each matrix element between two different atoms, we are considering that the rest of atoms not interact. Therefore, the problem is equivalent to consider an electron is a diatomic molecule. Most of the Hamiltonian matrix element are zero due to symmetry. To represent the Hamiltonian we can use both basis sets $\mid a,l,m\rangle$, complex, or, $\mid a,o\rangle$, real orbitals. The Slater-Koster parameters are those matrix elements expressed in the real atomic basis set. In this way, if the ordering of the basis set is: $s, p_x, p_y, p_z, d_{xy}, d_{yz}, d_{zx}, d_{x^2-y^2}, d_{z^2}$. The definition of the parameters is

$$\langle a,o \mid \hat{H}' \mid a',o' \rangle = \begin{pmatrix} V_{ss\sigma} & 0 & 0 & V_{sp\sigma} & 0 & 0 & 0 & 0 & V_{sd\sigma} \\ 0 & V_{pp\pi} & 0 & 0 & 0 & 0 & V_{pd\pi} & 0 & 0 \\ 0 & 0 & V_{pp\pi} & 0 & 0 & V_{pd\pi} & 0 & 0 & 0 \\ -V_{sp\sigma} & 0 & 0 & V_{pp\sigma} & 0 & 0 & 0 & V_{pd\sigma} & \\ 0 & 0 & 0 & 0 & V_{dd\sigma} & 0 & 0 & 0 & 0 \\ 0 & 0 & -V_{pd\pi} & 0 & 0 & V_{dd\pi} & 0 & 0 & 0 \\ 0 & -V_{pd\pi} & 0 & 0 & 0 & 0 & V_{dd\pi} & 0 & 0 \\ 0 & 0 & 0 & 0 & 0 & 0 & 0 & V_{dd\sigma} & 0 \\ V_{sp\sigma} & 0 & 0 & -V_{sp\sigma} & 0 & 0 & 0 & 0 & V_{dd\sigma} \end{pmatrix} \tag{2.27}$$

The notation of the Slater-Koster parameters is $V_{ll'm}$. Where l and l' stad for the orbital quantum numbers of the atomic orbitals involved and m magnetic quantum number on the $\hat{z}'$

axis. The only terms different from zero are those with $m = m'$. Also notice that, the sign of some Slater-Koster parameters change following the rule $V_{ll'm} = (-1)^{l+l'} V_{l'lm}$, due to parity of orbitals.

In general, in solids or molecules, the orbitals are quantized in arbitrary directions. Usually, all the orbitals are referenced to a commom cordinate system. Thus, in order to exploit in this manner the Slater-Koster parametrization it is compulsory to rotate the orbitals for each pair of atoms. We must express the arbitrary oriented orbitals into a linear combination of orbitals oriented along the direction of the bond.

The hopping integral between different orbitals is expressed as a linear combination of the Slater-Koster parameters using the director cosines as coefficients. In the Table (5.1) are summarized the expressions for s, p and d orbitals.

In this way, the matrix elements $\langle a, o \mid \hat{H}^{sp} \mid a', o' \rangle$, in the Slater-Koster approximation only depend on the relative vector $\rho_{aa'}$. The angular dependence is given by the director cosines of the bond vector that connects both atoms a and a'.

However, there are several methods to describe the distance dependence of the Slater-Koster parameters. Generally, they have to decrease very quickly with the distance due to the local nature of the orbitals. In our calculations, we have assumed the model proposed by W. A. Harrison [83]

$$V_{ll'm} \propto \frac{1}{\mid \rho \mid^2} \tag{2.28}$$

This is a rude approximation that is valid for small deviations of the equilibrium positions of the atoms, with the advantage that do not introduce new parameters in the model.

Owing to the local character of the orbitals, the tight-binding method only considers the interaction of each atom with the rest of system. Instead, it only consider interactions among the closet neighbour atoms, neglecting the interaction with atoms placed beyond a certain cut-off distance.

2.5 Electronic transport

2.5.1 Landauer formalism

One of the most active research fields in nanoscience is the one focusing on understanding and controlling the charge transport between bulk electrodes when these are connected by an atomic- or a molecular-size region and a bias voltage is applied between them[84]. The electronic ballist transport in nanoscopic systems can be described within the quantum theory of transport as a one dimensional scattering problem in quantum mechanics [85]. The scattering region or device (S) is connected to two electron reservoir, called left (L) and right(R), throught perfect leads (See Figure 2.2). These reservoirs provide the electrons to travel trough the system. In general, each reservoir can be in equilibrium but have different chemical potential, μ_L and μ_R. Each electron coming from the reservoir travels with momentum $\mathbf{k}$, through the lead toward the scattering region. The area of the lead is assumed to be much smaller than the propagation direction. Therefore,

Table 2.1: Hopping integrals for s, p, and d orbitals. The hopping integrals not given in this table can be found by cyclically permuting the directos cousines.

$H_{s,s}$	$V_{ss\sigma}$
H_{s,p_x}	$lV_{sp\sigma}$
H_{p_x,p_x}	$l^2V_{pp\sigma}+(1-l^2)V_{pp\pi}$
H_{p_x,p_y}	$-lmV_{pp\sigma}-lmV_{pp\pi}$
H_{p_x,p_z}	$-lnV_{pp\sigma}-lnV_{pp\pi}$
$H_{s,d_{xy}}$	$\sqrt{3}lmV_{sd\sigma}$
$H_{s,d_{x^2-y^2}}$	$\frac{\sqrt{3}}{2}(l^2-m^2)V_{sd\sigma}$
$H_{s,d_{z^2}}$	$[n^2-\frac{1}{2}(l^2-m^2)]V_{sd\sigma}$
$H_{p_x,d_{xy}}$	$\sqrt{3}l^2mV_{pd\sigma}+m(1-2l^2)V_{pd\pi}$
$H_{p_x,d_{yz}}$	$\sqrt{3}lmnV_{pd\sigma}-2lmnV_{pd\pi}$
$H_{p_x,d_{zx}}$	$\sqrt{3}l^2nV_{pd\sigma}+n(1-2l^2)V_{pd\pi}$
$H_{p_x,d_{x^2-y^2}}$	$\frac{\sqrt{3}}{2}l(l^2-m^2)V_{pd\sigma}+l(1-l^2-m^2)V_{pd\pi}$
$H_{p_y,d_{x^2-y^2}}$	$\frac{\sqrt{3}}{2}m(l^2-m^2)V_{pd\sigma}-m(1+l^2-m^2)V_{pd\pi}$
$H_{p_z,d_{x^2-y^2}}$	$\frac{\sqrt{3}}{2}n(l^2-m^2)V_{pd\sigma}-n(l^2-m^2)V_{pd\pi}$
$H_{p_x,d_{z^2}}$	$l[n^2-\frac{1}{2}(l^2+m^2)]V_{pd\sigma}-\sqrt{3}ln^2V_{pd\pi}$
$H_{p_y,d_{z^2}}$	$m[n^2-\frac{1}{2}(l^2+m^2)]V_{pd\sigma}-\sqrt{3}mn^2V_{pd\pi}$
$H_{p_z,d_{z^2}}$	$n[n^2-\frac{1}{2}(l^2+m^2)]V_{pd\sigma}-\sqrt{3}n(l^2+m^2)V_{pd\pi}$
$H_{d_{xy},d_{xy}}$	$3l^2m^2V_{dd\sigma}+(l^2+m^2-4l^2m^2)V_{dd\pi}+(n^2+l^2m^2)V_{dd\delta}$
$H_{d_{xy},d_{yz}}$	$3lm^2nV_{dd\sigma}+ln(1-4m^2)V_{dd\pi}+ln(m^2-1)V_{dd\delta}$
$H_{d_{xy},d_{zx}}$	$3l^2mnV_{dd\sigma}+mn(1-4l^2)V_{dd\pi}+mn(l^2-1)V_{dd\delta}$
$H_{d_{xy},d_{x^2-y^2}}$	$\frac{3lm(l^2-m^2)}{2}V_{dd\sigma}+2lm(m^2-l^2)V_{dd\pi}+\frac{lm(l^2-m^2)}{2}V_{dd\delta}$
$H_{d_{yz},d_{x^2-y^2}}$	$\frac{3mn(l^2-m^2)}{2}V_{dd\sigma}-mn[1+2(l^2-m^2)]V_{dd\pi}+mn[1+\frac{(l^2-m^2)}{2}V_{dd\delta}$
$H_{d_{zx},d_{x^2-y^2}}$	$\frac{3}{2}nl(l^2-m^2)V_{dd\sigma}-nl[1-2(l^2-m^2)]V_{dd\pi}-nl[1-\frac{1}{2}(l^2-m^2)]V_{dd\delta}$
$H_{d_{xy},d_{z^2}}$	$\sqrt{3}lm[n^2-\frac{(l^2+m^2)}{2}]V_{dd\sigma}-2\sqrt{3}lmn^2V_{dd\pi}+\frac{\sqrt{3}}{2}lm(1+n^2)V_{dd\delta}$
$H_{d_{yz},d_{z^2}}$	$\sqrt{3}mn[n^2-\frac{(l^2+m^2)}{2}]V_{dd\sigma}+\sqrt{3}mn^2(l^2+m^2-n^2)V_{dd\pi}-\frac{\sqrt{3}}{2}mn(l^2+m^2)V_{dd\delta}$
$H_{d_{zx},d_{z^2}}$	$\sqrt{3}ln[n^2-\frac{(l^2+m^2)}{2}]V_{dd\sigma}+\sqrt{3}ln(l^2+m^2-n^2)V_{dd\pi}-\frac{\sqrt{3}}{2}ln(l^2+m^2)V_{dd\delta}$
$H_{d_{x^2-y^2},d_{x^2-y^2}}$	$\frac{3}{4}(l^2-m^2)^2V_{dd\sigma}+[l^2+m^2-(l^2-m^2)^2]V_{dd\pi}+[n^2+\frac{1}{4}(l^2-m^2)^2]V_{dd\delta}$
$H_{d_{x^2-y^2},d_{z^2}}$	$\frac{\sqrt{3}(l^2-m^2)[l^2+m^2-(l^2-m^2)^2]}{2}V_{dd\sigma}+\sqrt{3}n^2(m^2-l^2)V_{dd\pi}+\frac{\sqrt{3}(1+n^2)(l^2-m^2)}{4}V_{dd\delta}$
$H_{d_{z^2},d_{z^2}}$	$[n^2-\frac{1}{2}(l^2+m^2)]^2V_{dd\sigma}+3n^2(l^2+m^2)V_{dd\pi}+\frac{3}{4}(l^2+m^2)^2V_{dd\delta}$

the transverse momentum is quantized giving rise to a set of subbands $\psi_n(\mathbf{k})$. The number of propagating channels on each lead, $N_L(E)$ and $N_R(E)$, depends on the energy E of the particles.

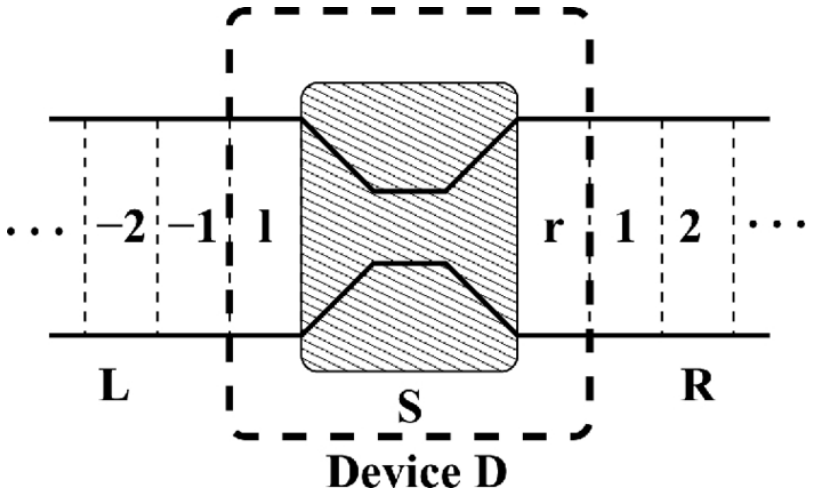

Figure 2.2: Sketch of transport problem for the case of one-dimensional nanowires as electrodes. The system is divided into three parts: L, D, and R. Extracted from [80]

Eventually, the electrons will find an elastic and coherent scattering source like constriction, molecules, deformation. The specific nature of the source is not important. Therefore, an incoming electron travelling through the propagating mode $\psi_n^L(\mathbf{k},E)$ from left reservoir, will be scatter into outgoing modes. It could be either re ected into outgoing modes $\psi_{n'_L}^L(-\mathbf{k},E)$ in the left lead with refection probability amplitude, r_{n_L,n'_L} or transmitted into outgoing modes $\psi_{n_R}(\mathbf{k},E)$ with a transmission probability amplitude t_{n_L,n_R}. In this way, the total wave function of the electron is a coherent superposition of the incoming and all the outgoing states

$$\psi_{n_L}(\mathbf{k},E)+\sum_{n'_L}^{N_L(E)} r_{n_L,n'_L}(E)\psi_{n'_L}^L(-\mathbf{k},E)+\sum_{n_R}^{N_R(E)} t_{n_L,n_R}(E)\psi_{n_R}(\mathbf{k},E) \tag{2.29}$$

An incoming electron in the nL mode will be transmitted into the right lead with a probability

$$T_{n_L}(E)=\sum_{n_L}^{N_L}\|t_{n_L,n_R}(E)\|^2 \tag{2.30}$$

We can define the density current associated to each mode n

$$j_n(\mathbf{k})=\frac{e}{\lambda}=\frac{e}{\lambda\hbar}\frac{dE_n(K)}{d\mathbf{k}} \tag{2.31}$$

where λ is the length of the conductor, and $v_n(\mathbf{k}$ is the group velocity of the mode n. The electrons travelling from the left reservoir to the right reservoir fill $N_L(E=\mu_L)$ modes. The amount that

each mode contributes to the current is

$$I_{N_L \to N_R} = \int_{E(\mathbf{k})<\mu_L} d(\mathbf{k}) j^t_{N_L}(\mathbf{k}) = \int_{E(\mathbf{k})<\mu_L} d\mathbf{k} j_{n_R}(\mathbf{k}) \| t_{n_L,n_R}(E) \|^2 j_{n_R} \tag{2.32}$$

$$= \int_{-\infty}^{\mu} \rho_{n_R}(E) \| t_{n_L,n_R}(E) \|^2 \frac{e}{\hbar} \frac{dE_{n_R}(\mathbf{k})}{d\mathbf{k}_{n_R}} \tag{2.33}$$

considering that the density of states can be writes as $\rho_{n_R} = \frac{1}{2\pi} \frac{d\mathbf{k}_{nR}}{dE}$ we can rewrite (2.32) as

$$I_{N_L \to N_R} = \frac{2e}{h} \int_{-\infty}^{\mu_L} \| t_{n_L,n_R}(E) \|^2 dE \tag{2.34}$$

The total contribution to the current by a mode n_L to the right reservoir is

$$I_{N_L \to R} = \sum_{n_R}^{N_R} \frac{2e}{h} \int_{-\infty}^{\mu_L} \| t_{n_L,n_R}(E) \|^2 dE = \frac{2e}{h} \int_{-\infty}^{\mu_L} T_{n_L}(E) dE \tag{2.35}$$

Where we have used (2.30) in the last step. So considering all the contributions of the N_L we can find the total current flow from the left reservoir to the right.

$$I^{tot}_{L \to R} = \sum_{n_R}^{N_R} \frac{2e}{h} \int_{-\infty}^{\mu_L} T_{n_L}(E) dE \tag{2.36}$$

At the same time, the right reservoir also can produce a current flow of electrons into the left reservoir. Assuming that the chemical potential of the right reservoir in thermal equilibrium is μ_R, the current from right to left reservoir is

$$I^{tot}_{R \to L} = \sum_{n_L}^{N_L} \frac{2e}{h} \int_{-\infty}^{\mu_R} T_{n_R}(E) dE \tag{2.37}$$

It is possible to show that if time reversal symmetry is preserved $t_{n_L,n_R}(E)$ is equal to $t_{n_R,n_L}(E)$ Hence, the total transmission for both right and left-moving electron are the same, i.e. $T(E) = \sum_{n_L} T^{L \to R}_{n_L} = \sum_{n_R} T^{R \to L}_{n_R}$.

Considering that the systems is based $\mu_L = \mu_R + eV$, the net current $I = I^{L \to R}_{tot} - I^{R \to L}_{tot}$ that flows thought the system is

$$I = \sum_{n_L}^{N_L} \frac{2e}{h} \int_{\mu_R}^{\mu_L} T_{n_L}(E) dE \tag{2.38}$$

This current depends on the bias voltage V in the upper limit of the integrand. Thus, the conductance through the scattering region is

$$G(V) = \frac{\partial I}{\partial V} = \frac{e^2}{h} \sum_{n_L}^{N_L} T_{n_L}(eV) \tag{2.39}$$

obtaining the Landauer result [86] . It shows that the conductance is a quantized value times the transmissions probability. The quantum of conductance is $G_0 = \frac{2e^2}{h}$ where the factor two came from the spin degeneracy. In the derivation it implicit because we have not considered spin degenerate propagating modes.

2.5.2 Green's functions and partitioning technique

It is possible to solve the scattering problem using single-particle Green's functions [80, 85, 87]. It is specially useful to use a localized atomic orbital basis set to represent the Hamiltonian. Usually, to compute the transmission and obtain the properties of the system by solving the Schrödinger equation is a difficult task. However, Green's formalism allows to obtain information about the systems without solving the eigenvalue problem.

The green function is defined by the equation $(E-H)G(E)=I$, where E is the energy of the system, H the Hamiltonian and I is the identity matrix. It give the response of the whole system, $|\psi\rangle$, to a constant perturbation $|u\rangle$.

$$H|\psi\rangle = E|\psi\rangle + |u\rangle \tag{2.40}$$

$$(E-H)|\psi\rangle = -|u\rangle \tag{2.41}$$

$$|\psi\rangle = -G(E)|u\rangle \tag{2.42}$$

Using Green's function we can get the response of the system $|\psi\rangle$ by (2.40) without solving the differential equation (2.41).

In analogy with the scheme in the scattering problem, the system is partitioned in three regions, see Fig. 2.5. A central region, where the scattering source is placed, here we called device (D), and two leads on the right (R) and left (L) where the electrons move in or out of the device. Thus, the Hamiltonian of the whole systems is

$$H = \begin{pmatrix} H_L & V_{LD} & 0 \\ V_{DL} & H_D & V_{DR} \\ 0 & V_{RD} & H_R \end{pmatrix} \tag{2.43}$$

Where H_L, H_D and H_R are the Hamiltonians of the isolated leads and device. They are interconnected by the hopping matrices, V_{LD} and $V_{DL}=V_{LD}^{\dagger}$ for the left lead and the device and V_{DR} and $V_{RD}=V_{DR}^{\dagger}$ for the right lead and the device. Here we are assuming that there is no coupling between the leads.

We can get the Green's function of each individual parts using the definition

$$\begin{pmatrix} E-H_L & -V_{LD} & 0 \\ -V_{DL} & E-H_D & -V_{DR} \\ 0 & -V_{RD} & E-H_R \end{pmatrix} \cdot \begin{pmatrix} G_L & G_{LD} & G_{LR} \\ G_{DL} & G_D & G_{DR} \\ G_{RL} & G_{RD} & G_R \end{pmatrix} = \begin{pmatrix} I & 0 & 0 \\ 0 & I & 0 \\ 0 & 0 & I \end{pmatrix} \tag{2.44}$$

For example, the Green's function for the device can be obtained selecting the equations in B.7 produced by the central column in the Green's function matrix.

$$(E-H_L)G_{LD} - V_{LD}G_D = 0 \tag{2.45}$$

$$-V_{DL}G_{LD} + (E-H_D)G_D - V_{DR}G_{RD} = I \tag{2.46}$$

$$(E-H_R)G_{RD} - V_{RD}G_D = 0 \tag{2.47}$$

To obtain G_D from the second equation we need G_{RD} and G_{LD}, that we obtain from the first and third equations

$$G_{LD} = g_L V_L G_D \tag{2.48}$$
$$G_{RD} = g_R V_R G_D \tag{2.49}$$

where we have defined $g_L = (E - H_L)^{-1}$ and $g_R = (E - H_R)^{-1}$, the Green's functions of the isolated leads. In this way, the second equation in (2.47) reads

$$-V_{DL} g_L V_{LD} G_D + (E - H) G_D - V_{DR} g_R V_{RD} G_D = I \tag{2.50}$$

from which we obtain the Green's function for the Device

$$G_D = (E - H_D - \Sigma_L - \Sigma_R)^{-1} \tag{2.51}$$

Where $\Sigma_L = V_{DL} g_L V_{LD}$ and $\Sigma_R = V_{DR} g_R V_{RD}$ are the self-energies which describe the influence of the leads on the electronic structure of the device. They are calculated iteratively solving the Dyson equations [88].

Now, that we can obtain the Green function of the whole sytem, we can try to solve the problem of an electron passing thought the system. To this end, we have to compute the response of the system, $|\psi\rangle$ to an incoming electron $|\psi_i\rangle$. In this way, using the nonequilibrium Green's function it is possible to obtain the Landauer formula (2.39), where the transmission is given in terms of the Green function of the device by the Caroli formula [89].

$$T(E) = \left[G_D^\dagger \Gamma_L G_D \Gamma_R \right] \tag{2.52}$$

with $\Gamma_L = i(\Sigma_L - \Sigma_L^\dagger)$ and $\Gamma_R = i(\Sigma_R - \Sigma_R^\dagger)$ the coupling matrices of the device with the left and right leads.

CHAPTER 3

A THEORETICAL STUDY OF THE ELECTRICAL CONTACT BETWEEN METALLIC AND SEMICONDUCTING PHASES IN MONOLAYER MoS_2

3.1 Introduction

Present research surge on two-dimensional (2D) crystals[2, 11, 90–92] will soon translate into devices with new or enhanced capabilities. Layered materials such as transition-metal dichalcogenides (TMDs), in particular, are drawing attention because they easily exfoliate into 2D semiconductors and due to their manifold of electrical, optical, mechanical, and chemical properties[93, 94]. These properties make them viable candidates for future nanoscale electronics [95–102], including field-effect transistors (FET's) which promise to surpass expectations of present silicon-based ones. A low contact resistance, R_c, is, however, critical for achieving high on/off current ratios[2], large photoresponse[103], and high-frequency operation[104], among others. However, a large R_c at the interface between the 2D semiconductors and any bulk metallic electrode is commonplace and drastically affects their functionality [86, 100, 105]. For TMDs, R_c values in the range of 10^4 - 10^7 $\Omega\mu$m have been reported[106]. Contacting 2D crystals presents not only experimental challenges, but also poses novel conceptual issues. To begin with, traditional concepts that have shaped our understanding of conventional metal-semiconductor contacts break down in the limit where the semiconductor thickness is smaller than the depletion and transfer lengths. In the 2D limit the chemical interaction or hybridization between the metal and the 2D crystal determines the interface contact resistivity, but also affects the sheet resistivity of the 2D crystal underneath the metal. Furthermore, the dimensionality mismatch between the 3D metal and the 2D semiconductor relegates most of the contact area to a secondary role, in favour of the electrode edge were current crowding takes place[106].

Theoretical works, typically based on density functional theory (DFT) calculations, have tried

to gain insight into the electronic structure of the top metal-2D crystal junction in order to identify avenues leading to a reduction of R_c. Khomyakov et al.[107], for instance, have extensively studied the electronic properties of graphene deposited on metals. Gong et al. [108] have carried out similar studies for metal/phosphorene interfaces. While the information obtained from these works might be relevant to understand the interface resistivity, it gives little insight as far as the actual R_c is concerned. For instance, a pure edge contact to graphene has been experimentally shown to achieve R_c values similar or lower than most top contacts [109], challenging the naive view that having a large contact area will result in a decreased value of the contact resistance and downplaying the role of the interface between the metal and the 2D crystal.

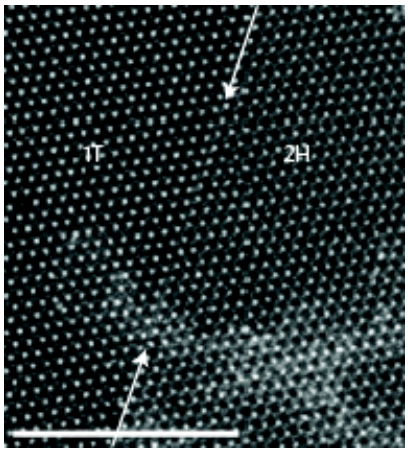

Figure 3.1: High-resolution transmission electron microscope image of an atomically thin phase boundary (indicated by the arrows) between the 1T and 2H phases in a monolayered MoS_2 nanosheet. Scale bar, 5 nm. (Extracted from [110])

Here we turn our attention to, arguably, the most promising 2D crystal to date, a single layer of MoS_2, and a radically new proposal for reducing R_c[110]. This 2D material consists of a 6.7 Å thick S-Mo-S trilayer sandwich [93]. Polymorphism is one of the unique features of layered TMDs such as MoS_2[111–113]. A monolayer of MoS_2 presents two crystallographic phases: a trigonal prismatic (2H), the most common one[111–113], and a trigonal antiprismatic (1T) phase, which is metastable and persists after exfoliation until subject to heating or aging. The two phases exhibit substantially different electronic structures due to the changes in the crystal symmetry. The former is semiconducting and the latter is metallic.

Recently, the possibility of controlling the coexistence of the two phases in the same crystal has been exploited to create low resistance contacts[110] to the technologically relevant semiconducting phase. The metallic 1T phase of MoS_2 can be locally induced on semiconducting 2H phase nanosheets (see Fig. 3.2), thus decreasing R_c to 200-300 $\Omega\mu$m at zero gate bias. The contact resistances were measured using the transfer length method (TLM), as shown in Fig. .

FETs with 1T phase electrodes fabricated and tested in air exhibit mobility values of $\approx$50 cm^2

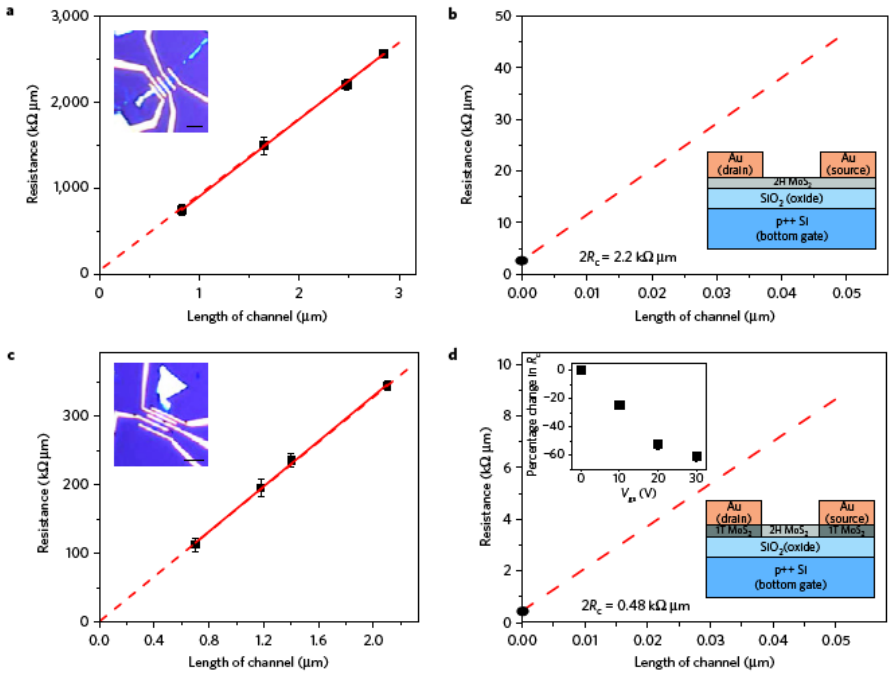

Figure 3.2: Resistance versus 2H channel lengths for Au deposited directly on the 2H phase (a,b) and on the 1T phase (c,d). (Extracted from [110])

V^{-1} s^{-1}, subthreshold swing values below 100 mV per decade, on/off ratios of $> 10^7$, drive currents approaching 100 μA μm $^{-1}$, and excellent current saturation. The mobility values reported can be further improved by elimination of any organic residues that might be present on the surface of MoS_2 as well as optimization of dielectric deposition and annealing procedures.

A key factor in the context of edge contacts is the Schottky barrier (SB) formed at the interface between the metallic phase and the semiconducting one. In the simplest Mott-Schottky picture for metal-semiconductor interfaces, the potential barrier of electron injection is primarily dictated by the difference between the metal Fermi level E_F and the electron affinity χ or bottom of the conduction band of the semiconductor. The barrier for hole injection is likewise determined by the difference between E_F and the top of the valence band. This simple picture needs to be supplemented by a three-fold detailed analysis of the interface. First, in-gap interface states or metal-induced states play a key role in the equilibration of the chemical potentials, hosting the charge transferred between the metal and the semiconductor and actually determining the Schottky barrier. Second, the dipole created by the charge transfer, one-dimensional in nature, is expected to decay away from the interface[114], reducing its impact on the Schottky barrier. Finally, the transparency for electrons and holes need not be identical, actually depending on wave-function hybridization details at the interface. In this work we present a full theoretical analysis of all these sides to the problem using density functional theory (DFT) as well as tight-binding models with Slater-Koster parametrization.

3.2 Methods

The DFT calculations were performed using the plane-wave pseudopotential method as implemented in Quantum Espresso code[115]. The exchange correlation potential was approximated by a generalized gradient approximation (GGA-PBE)[116]. An ultrasoft pseudopotential description of the electron-electron interaction was used with valence electrons $4d^5$, $5p^1$ and $3s^2$, $3p^4$ of Mo and S atoms, respectively. Kinetic energy cutoffs were set to 56 Ry and 560 Ry for plane waves and charge density, respectively, and a Monkhorst-Pack [117] scheme with a $4\times12\times1$ k-mesh for the Brillouin zone integration (BZ). We also construct a tight-binding Hamiltonian in the Slater-Koster approximation[118]. The model includes the three p orbitals of the S atom (p_x, p_y, p_z) and the five d of the Mo atoms ($d_{3z^2-r^2}$, d_{xz}, d_{yz}, d_{xy}, $d_{x^2-y^2}$). Considering that the unit cell contains one Mo atom and two S atoms, we thus expand the Hilbert space by means of the 11-fold vector:

$$\begin{aligned}\phi_i^\dagger &= (p_{i,x,t}^\dagger, p_{i,y,t}^\dagger, p_{i,z,t}^\dagger, d_{i,3z^2-r^2}^\dagger, d_{i,xz}^\dagger, d_{i,yz}^\dagger, \\ &\quad d_{i,xy}^\dagger, d_{i,x^2-y^2}^\dagger, p_{i,x,b}^\dagger, p_{i,y,b}^\dagger, p_{i,z,b}^\dagger)\end{aligned} \tag{3.1}$$

where $d_{i,\mu}^\dagger$ creates an electron in the orbital μ of the Mo atom in the i-unit cell, $p_{i,\mu,t}^\dagger$ creates an electron in the orbital μ of the top (t) layer atom S in the i-unit cell, and $p_{i,\mu,b}^\dagger$ creates an electron in the orbital μ of the bottom (b) layer atom S in the i-unit cell. All the information about hopping processes are encoded in the Slater-Koster parameters, $V_{pd\sigma}$, $V_{pd\pi}$ (Mo-S bonds), $V_{dd\sigma}$, $V_{dd\pi}$, $V_{dd\delta}$ (Mo-Mo bonds) and $V_{pp\sigma}$, $V_{pp\delta}$ (S-S bonds). Additional relevant parameters are the crystal fields Δ_0, Δ_1, Δ_2, Δ_p and Δ_z. The TB parameters, as reported in Ref. [79], are shown in Table 3.1.

The electronic transport at the interface is addressed by a standard Green's function (GF) approach as implemented in our code ANT.1D[80]. In regards to this, we consider a finite-width ribbon divided into two semi-infinite segments by the 2H/1T interface. We then split the system into three parts (see Fig. B.7), namely a central region containing the interface which is connected to the perfect left (1T) and right (2H) lead (see details below).

The Hamiltonian can thus be written as

$$H = H_I + H_{2H} + H_{1T} + h_{1T} + h_{2H} \tag{3.2}$$

where H_I, H_{1T}, and H_{2H} are the Hamiltonians of the central portion containing the interface, and the semiinfinite left and right leads, respectively. h_{1T} and h_{2H} are the hopping matrices between these leads and the central region. The GF of the latter is

$$G_I = (E - H_I - \Sigma_{1T} - \Sigma_{2H})^{-1} \tag{3.3}$$

where $\Sigma_l = h_l g_l h_l^\dagger$ is the self-energy due to the lead l = 1T, 2H, and $g_l = (E - H_l)^{-1}$ is the GF of the semi-infinite lead l.

Table 3.1: Tight-binding parameters for single-layer MoS_2. All the hoppings terms V_α and crystal fields Δ_α are in unit of eV.

Crystal fields	Δ_0	-1.512
	Δ_1	0.419
	Δ_2	-3.025
	Δ_p	-1.276
	Δ_z	-8.236
Intralayer Mo-S	$V_{pd\sigma}$	-2.619
	$V_{pd\pi}$	-1.396
Intralayer Mo-Mo	$V_{dd\sigma}$	-0.933
	$V_{dd\pi}$	-0.478
	$V_{dd\delta}$	-0.442
Intralayer S-S	$V_{pp\sigma}$	0.696
	$V_{pp\delta}$	0.278

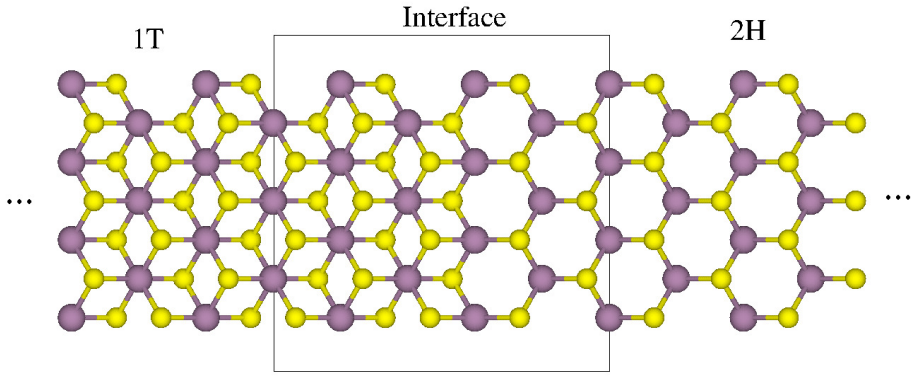

Figure 3.3: (color online). Sketch of the model used to calculate the electronic transport properties of 2H/1T monolayer with armchair and zigzag interfaces.

3.3 Results and discussion

The crystal structures of a MoS_2 monolayer has one Mo atom and a pair of S atoms in the unit cell. In the 2H phase the S-Mo atoms are in an eclipsing configuration from the top view so the atomic stacking sequence is AB, while the 1T phase has an atomic stacking sequence ABC where the top S atoms occupy the hollow center of the 2H hexagon lattice as shown in Figure 6.1.

The DFT study of the interface is performed by constructing a supercell with 12 units cells for each 2H and 1T phases along the x-direction (perpendicular to the interface), with a single unit in the infinite y direction (along the interface). Two natural crystallographic boundaries or junctions are considered in what follows: Armchair and zigzag (see Fig. 3.8 below). A vacuum layer of at least 15 Å between plane is in order to suppress the interaction between the periodic images. The electronic properties of a monolayer of MoS_2 are sensitive to its lattice parameters[119] and we fix this and the bond length to their experimental values a = 3.16 Å[120] and d = 2.42 Å[121],

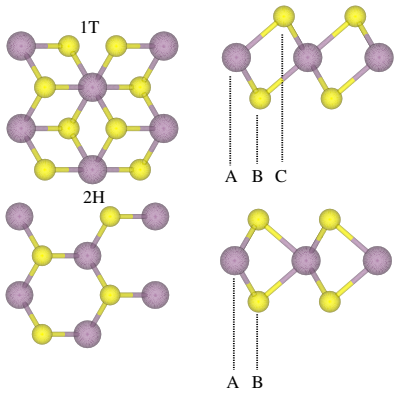

Figure 3.4: (color online). Atomic structure of semiconducting phase (2H) and a metallic phase (1T). The 2H phase shows hexagon lattice and an atomic stacking sequence of AB. The 1T phase shows the atomic stacking sequence of ABC.

respectively. We thus avoid the instability of the 1T phase towards the 1T' phase, (predicted to be a topological insulator[122]), which we also obtain if we allow relaxation of the 1T phase atoms. This is justified on the basis of the experimental evidence.

To later understand the influence of the type of interface on the electronic and transport properties of the 2H/1T heterostructure, we first discuss the electronic band structure of (unpassivated) 1T and 2H nanoribbons with zigzag and armchair edges. The band structure of 1T-nanoribbons reveals metallic behavior for both type of edges, zigzag and armchair [see Fig. 3.5(a) and (c)]. The metallic behavior also is observed for 2H-zigzag nanoribbons [see Fig. 3.5(b)]. In this case, the metallicity comes from the presence of edge states (blue lines) composed of the $4d$ electrons of edge Mo atoms and $3p$ electrons of edge S atoms which expand the whole gap (the black lines correspond to bulk states). In contrast, as shown in Fig. 3.5(d), 2H-armchair nanoribbons feature a semiconducting character, but also presenting edge states. In this case the edge state bands are rather flat and do not cross the entire gap as in the zigzag case. The number of edge bands remains constant and their general character is weakly dependent on the ribbon width in both cases. These results are in agreement with previous studies [123, 124]. The charge neutrality level (CNL) separating occupied (solid lines) from empty (dashed lines) edge states is set to zero. The edge states here will play an important role when the 2H/1T interface is formed since they give rise to a finite density of states in the gap and a reservoir for charge transfer. Figure 3.6 schematically illustrates the band alignment of the metallic phase and the semiconducting phase before they are brought into contact (left) and after the contact (right). The work function of the metallic phase and the electron affinity and band gap of the semiconducting one are obtained from bulk DFT calculations. In the simplest Mott-Schottky picture (without charge transfer and interface dipoles) the Fermi level of the 1T phase roughly lies in the middle of the gap of the 2H phase and the electrons see a potential or Schottky barrier Φ_B^e against their

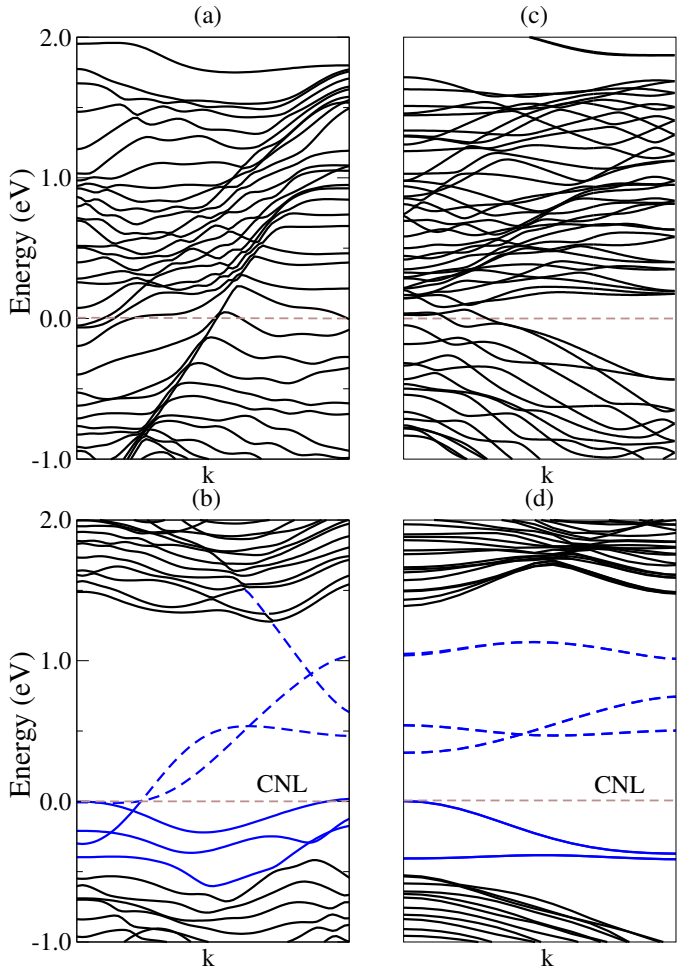

Figure 3.5: (color online). (a) Band structure of a 1T and (b) 2H-zigzag nanoribbon (3.1 nm); (c) 1T and (d) 2H-armchair nanorribon (2.5 nm) of MoS_2. Blue lines correspond to the edges states while dashed lines represents empty bands. The CNL is at zero.

migration from the 1T phase into the 2H phase of ≈ 0.8 eV (which is fairly similar for holes). This barrier changes upon charge transfer. When the metallic phase and the semiconducting phase are actually brought into contact, the chemical potentials of the two phases must equilibrate. Strictly speaking, in our zero temperature calculations, we should refer to the Fermi level of the 1T phase and the CNL of the 2H phase. From Fig. 3.5 we anticipate a lower CNL of the 2H phase with respect to the Fermi level of the 1T phase also once brought into contact. The large density of edge states on the 2H phase will pin the Fermi level close to the CNL and therefore closer to the valence band for both edge terminations. Actually, a potential step, as schematically shown in Fig. 3.6 (on the right), will develop at the interface region as a result of the expected electron transfer from the 1T phase into the 2H phase. Note however that, since the interface dipoles are one-dimensional, the potential step must eventually decay away from the interface[114]

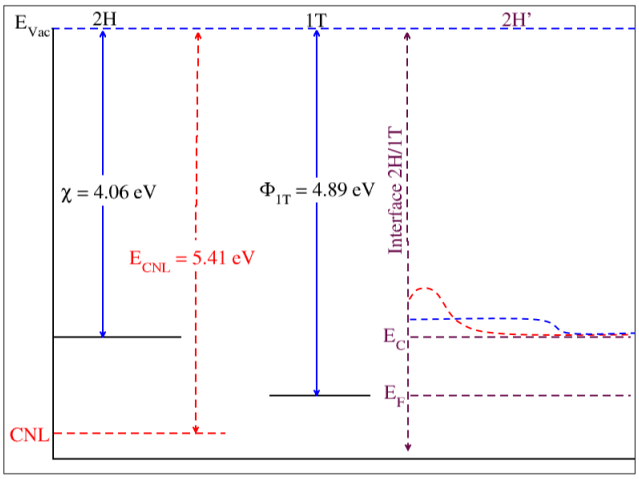

Figure 3.6: (color online). Schematic energy diagram at the 1T/2H interface. On the left the Mott-Schottky band-alignment is represented. On the right, the band-bending due to the charge dipole and their expected decay away from the interface is shown for both crystallographic orientations of the interface.

in a logarithmic fashion. The schematic digram in Fig. 3.6 is confirmed by our layer-by-layer projected density of states (pDOS) near the 1T/2H interface. As shown in Fig. 6.9, the common Fermi level (placed at zero) lies above the CNL (black dashed line) at the interface layer and layers nearest to the interface, indicating that unoccupied edge states have been filled after the contact. Consequently, since the CNL lies closer to the top of the valence band, the Fermi level is also pinned closer to the top of the valence band for both interfaces. The actual position of the Fermi level in the gap near the interface depends on the details of the pDOS. The pinning is particularly strong at the armchair interface, where the pDOS presents a peak [see Fig. 6.9(a)] which comes from the flat bands shown in Fig. 3.5(b). We can also appreciate how the dipole potential quickly decays into the bulk since the edge states hosting the charge transferred are strongly localized at the interface (see also Fig. 3.8). Sufficiently away from the interface the Fermi level must lie in the middle of the gap as schematically shown in Fig. 3.6. Pinning also occurs for the zigzag interface [see Fig. 6.9(b)], but the edge states penetrate more into the bulk (see Fig. 3.8) and sustain the dipole potential further away from the interface. In summary, the Schottky barrier near the interface is lower for holes than for electrons for both cases. This difference penetrates more into the bulk for the zigzag interface than for the armchair one until eventually the Mott-Schottky limit given by $\Phi_B^h \approx \Phi_B^e = \chi - \phi_{1T}$) is recovered.

We finally discuss the results of the transport calculations. These have been performed for zigzag and armchair ribbons with a 1T/2H interface separating two semi-infinite segments

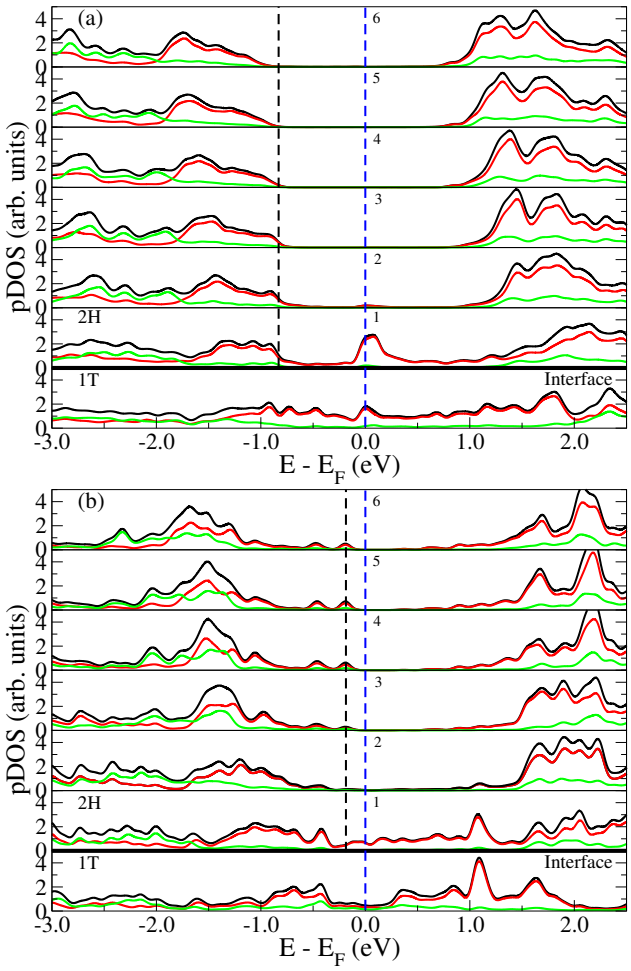

Figure 3.7: Partial density of states (pDOS) for the 2H/1T (a) armchair interface and (b) zigzag interface. (Red lines) Mo atom; (green lines) S atoms; (black lines) Mo + S atoms. The indices 1-5 represent the unit cell of the 2H phase from the interface. The Fermi level is to zero and the dashed black lines represent the CNL.

(see Fig. B.7 for an armchair example). Two different widths of ≈ 2.2 and ≈ 4.4 nm have been considered in both cases. In order to incorporate the relevant information of the DFT calculations into the tight-binding methodology we have added the DFT dipole potential to the on-site energies on both sides of the interface. The central region where the interface is located is long enough as to contain this dipole potential which, as explained above, vanishes for sufficiently long distances away from the interface.

The total transmission for the four cases is shown in Figure 3.9 along with the transmission of the perfect 2H ribbons [Fig. 3.9(a) and Fig. 3.9(c)]. The states close to the Fermi level for a 2H nanoribbon (zigzag and armchair) are edge states, as shown in Fig. 3.5 in blue color. In Figure 3.9, we removed the contribution of these edge states to the transmission curves for clarity and

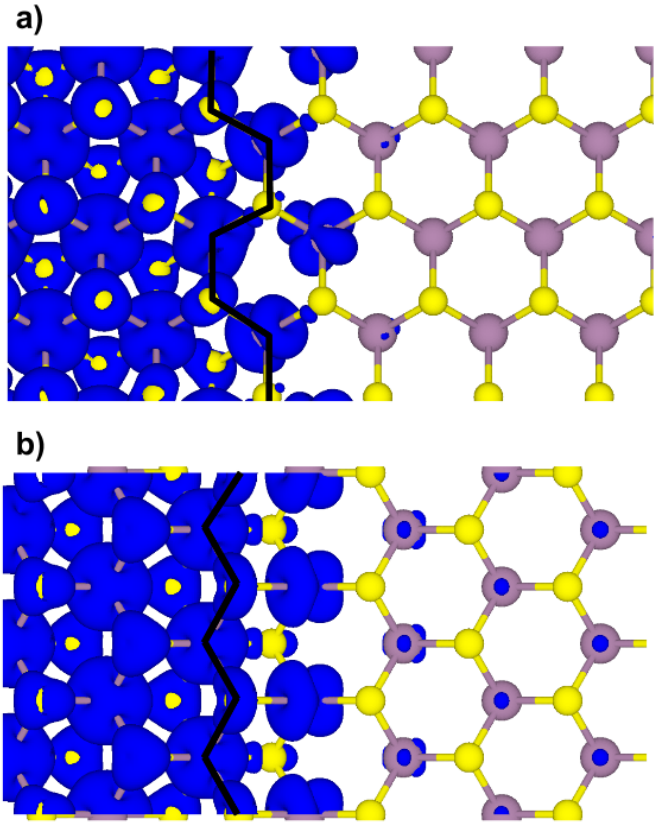

Figure 3.8: (color online). Isosurface (0.015 e/Å^{-3}) of the DOS at the Fermi energy for zigzag (a) and armchair (b) interfaces showing the larger extension into the bulk of the edge states for the zigzag case.

because their contribution to the contact resistance for infinitely wide ribbons (i.e. the 2D case) should be insignificant. The number of channels is larger for electrons than for holes for both crystallographic directions [see Fig. 3.9(a) and Fig. 3.9(c)], but with the interface this difference is reduced [see Fig. 3.9(b) and Fig. 3.9(d)]. Also note that the location of the Fermi energy in the gap corresponds to the Mott-Schottky limit since the dipole potential and the change in the bare Schottky barrier, although incorporated in the on-site elements, cannot be directly noticed in the position of the Fermi energy in the gap. It reflects, however, in the transmission function, as shown in Fig. 3.10, where the details of this function near the gap is shown for the bare tight-binding parameters and the corrected ones due the interface dipole. We further compute the interface contact resistance from the transmission curves by using the Landauer formula [125],

$$I = \frac{2e}{h}\int dE[f(E-E_F-eV/2)-f(E-E_F+eV/2)]T(E) \tag{3.4}$$

where f represents the Fermi distribution function, E_F is the Fermi level and $T(E)$ is the

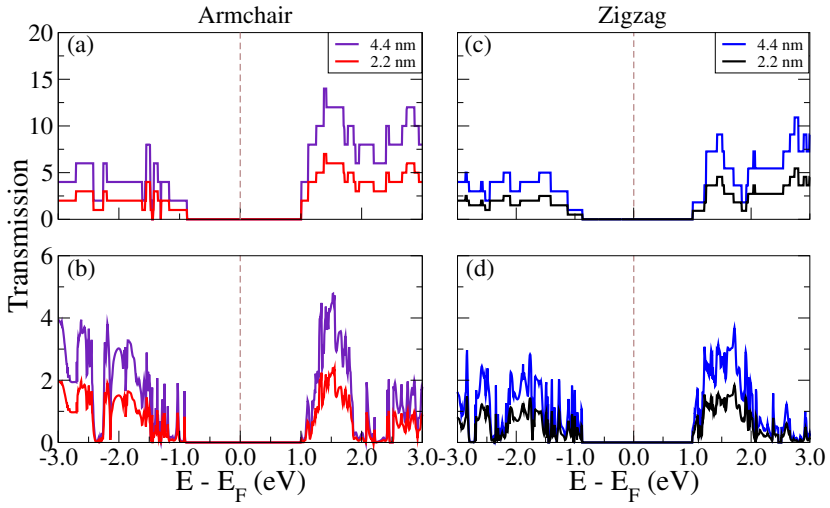

Figure 3.9: (color online). Trasmission curves for 2H-MoS_2 nanoribbons with transport direction perpendicular to armchair direction (a), the same for the 2H/1T armchair interface (b), the same for 2H-MoS_2 nanoribbons with transport direction perpendicular to zigzag direction, and similarly for the 2H/1T zigzag interface.

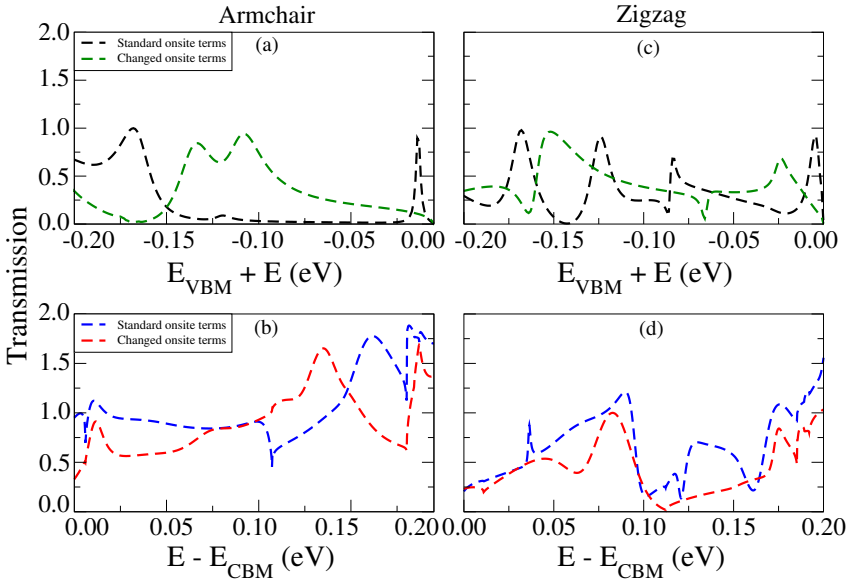

Figure 3.10: (color online). Transmission curves for holes (a,c) and electrons (b,d) close to conduction band maximum (CBM) and valence band maximum (VBM), respectively. The dashed black lines represent the transmission curves for standard onsite terms as shown in Table 3.1 and the dashed green lines represent the transmission curves after adding the DFT dipole potential to the on-site energies.

transmission function. Thus, the contact resistance may be defined as

$$R_c(E_F) = [R_{2H/1T}(E_F) - R_{2H}(E_F)] \times w \tag{3.5}$$

were R is the 'resistance × contact width' (in units of Ω m) and subindices $2H1T$ and the $2H$ refer to hybrid structure and semiconducting phase of the MoS_2, respectively. Assuming that, for $V \to 0$ we have $[f(E-E_F-eV/2)-f(E-E_F+eV/2)] \approx \frac{df}{dE}$ in Eq. 3.4, the Eq. 5.3 can be rewritten as:

$$R_c(E_F) = \frac{k_B T}{\int\int \frac{e^{(E-E')/k_B T}}{(1+e^{(E-E')/k_B T})^2} T_{1T/2H}(E) w(E'-E_F;\delta E)\, dE\, dE'} - \frac{k_B T}{\int\int \frac{e^{(E-E')/k_B T}}{(1+e^{(E-E')/k_B T})^2} T_{2H}(E) w(E'-E_F;\delta E)\, dE\, dE'}, \tag{3.6}$$

which incorporates an effective broadening function $w(E-E_F;\delta E)$ to account for irregularities and impurities along the interface (δE quantifies this disorder). The broadening function could in principle have any shape, but in the simplest situation it is described by a Lorentzian function centered around $E' = E_F$

$$w(E'-E_F;\delta E) = \frac{\delta E/\pi}{(E'-E_F)-(\delta E)^2}. \tag{3.7}$$

The result is shown in Fig. 3.11 and Fig. 3.12 for interfaces with two different disorder strengths at room temperature. The Fermi energy is assumed to vary without changing the electronic structure at the interface. Fig. 3.11 shows the behaviour of contact resistance near

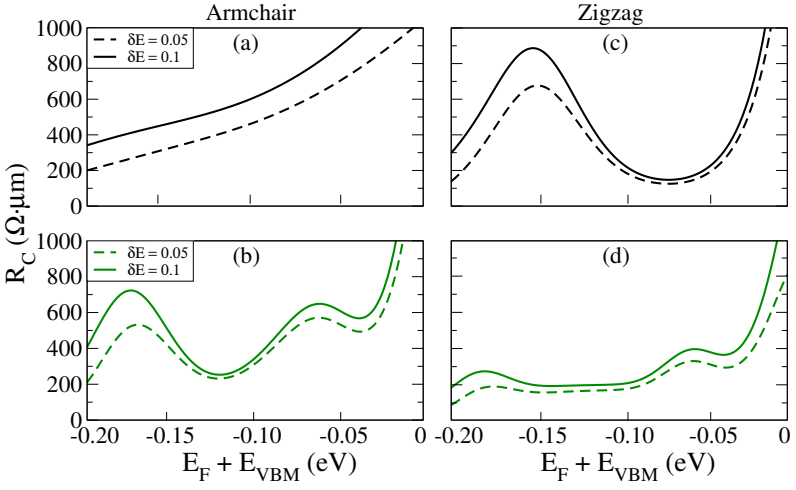

Figure 3.11: (color online). Contact resistance for holes with standard onsite energies (a,c) (black lines) and changed onsite energies (b,d) (green lines). δE indicates the disorder.

the valence band for both interfaces. The addition of the dipole potential to the on-site energies significantly reduces (in average) the values of the contact resistance for both cases. This can be

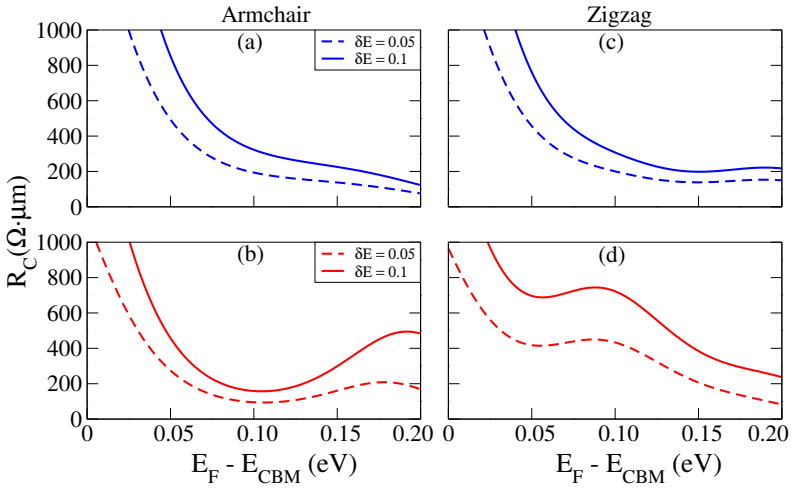

Figure 3.12: (color online). Contact resistance for electrons with standard onsite energies (a,c) (blue lines) and changed onsite energies (b,d) (red lines). δE indicates the disorder parameter.

attributed to the Fermi level pinning near the valence band and the local upward bending of the valence band near the interface which increases the DOS at the interface for hole injection.

For electron injection, on the contrary, the dipole potential increases the contact resistance with respect to the bare tight-binding results because of the upward band bending near the interface which suppresses the DOS near the interface. Interestingly we observe that the contact resistance is larger for the zigzag interface. We attribute this, in part, to the longer penetration of the dipole potential and concommitant increased Schottky barrier width (see scheme in Fig. 3.6). Notice that we have normalized the resistance to the width of nanoribbons. Still differences due to the finite size might be expected, but they are insignificant. Despite the implicit approximations behind Eq. 3.6, our result for R_c for energies near the edge of the conduction band (see Fig. 3.12) agrees quite nicely with the experimental value reported in [110], which was obtained for doped MoS_2.

3.4 Conclusion

In summary, we have presented a complete theoretical study of the electrical contact between the two most common crystallographic phases of MoS_2 monolayer crystals: the stable semiconducting 2H phase and the metastable metallic 1T phase. Our DFT results have shown that, due to the Fermi level pinning to a large density of states at the edge, there is a higher Schottky barrier for electrons than for holes (in the case of undoped MoS_2). Charge transfer from the 1T to the 2H phase occurs, but, as expected for a one-dimensional contact, the generated dipole potential decays away from the interface and the naive Schottky-Mott band-alignment picture is recovered away from the interface. Tight-binding quantum transport calculations aided by the DFT results

have confirmed low contact resistance values in the range of ≈ 200 - 400 $\Omega\mu$m, as experimentally reported. Furthermore, the contact resistance is predicted to be smaller at the armchair interface for electron injection and, on the contrary, smaller for hole injection at the zigzag interface.

CHAPTER 4

FRANCKEITE: A NATURALLY OCCURRING STACKED VAN DER WAALS HETEROSTRUCTURE WITH A NARROW BANDGAP

4.1 Introduction

The demonstration of the deterministic placement of 2D crystals has opened the door to fabricate more complex devices[126], but more importantly, it has started the investigation to tailoring the properties of designer materials by stacking different 2D crystals to form so-called van der Waals heterostructures[40]. One approach to produce such heterostructures is to use epitaxially grown materials assembled sheet by sheet[127]. This method, however, remains challenging and has only been demonstrated for a few van der Waals heterostructures so far[128–130]. Another approach is the manual assembly of individual layers obtained by mechanical exfoliation from bulk and the deterministic placement of one layer on top of another[131–136]. This method also presents issues that remain to be solved, such as controlling the exact crystalline alignment between the stacked lattices and avoiding the presence of interlayer atmospheric adsorbates.

In this chapter, we present an extensive theoretical and experimental (carried out by our collaborators) study of ultrathin layers of franckeite, a naturally occurring sulfosalt with a structure formed by alternated stacking of tin disulfide-based (SnS_2) and lead sulfide-based (PbS) layers. Interestingly, the individual layers present a larger bandgap than the naturally formed van der Waals heterostructure (0.7 eV), which is among the narrowest found in 2D semiconductors. We also find that franckeite is a *p*-type material, a very rare feature in two-dimensional semiconductors, only found so far in a few materials such as black phosphorus and tungsten diselenide[10, 137–140] but, unlike black phosphorus, franckeite is air-stable. We combine density functional theory (DFT) calculations with the experimental characterization of the optical and

electrical properties of ultrathin franckeite, which we isolate both by micromechanical cleavage and liquid-phase exfoliation, to offer a complete picture of its unique properties.

This work has been performed in collaboration with Andrés Castellanos-Gomez, Emilio M. Pérez and Lúcia Abelle groups from IMDEA-Nanociencia and ALBA Synchrotron. Dr. Aday Molina-Mendonza and Dr. Joshua O. Island performed the optoelectronic characterization of the photodetectors and the p-n junction, fabricated by Dr. Andrés Castellanos-Gomez. Dr. Emerson Giovanelli performed the SEM, TEM, SAED characterization of the material and the liquid-phase exfoliation with the corresponding characterization. Dr. Andrés Castellanos-Gomez and Lucía Abelle groups performed the micro-XPS measurements on mechanically exfoliated flakes at Circe beamline (BL24-CIRCE) at ALBA Synchrotron with the collaboration of ALBA staff. Dr. Charalambos Evangeli and Nicolás Agrait performed the thermopower measurements of the bulk material.

4.2 Experimental setup and characterization

4.2.1 Crystal structure

Franckeite is a layered material from the sulfosalt family formed by the stacking of pseudohexagonal (H) and pseudotetragonal (Q) layers that interact by van der Waals forces[141–143]. The Q layer is composed of four atomic layers of sulfide compounds with the formula MX, where M = Pb^{2+}, Sn^{2+} or Sb^{3+} and X = S. The H layer consists of octahedrons of disulfide compounds with the formula MX2, where M=Sn^{4+} or Fe^{2+} and X = S. In Fig. 4.1, we show the crystal structure of the material, indicating the different atomic layers present in the crystal. In Fig. 4.1(a), the black solid line indicates the unit cell of this system that is characterised by the lattice parameters: $a = 5.80$ Å, $b = 5.84$ Å, $c = 17.27$ Å, $\alpha = 94.97°$, $\beta = 88.45°$and $\gamma = 89.94°$.

In Figure 4.2 we can see photographs of franckeite mineral taken with a zoom lens incorporated in a digital camera. The exfoliated material is obtained by either grinding of cleaving the bulk piece of material. Bulk franckeite mineral from mine San José, Oruro (Bolivia) was used for both mechanical and chemical exfoliation. All the experiments were carried out with flakes obtained from the same crystal.

4.2.2 X-ray diffraction characterization

Franckeite powder was studied by means of X-ray diffraction in a Xpert PRO $\theta/2\theta$ diffractometer (Panalytical) at room temperature in the facilities of Servicio Interdepartamental de Investigación (SIdI), Universidad Autónoma de Madrid. The measured spectra is shown in Figure 4.3, together with a fit for each peak. The diffraction peaks are in good agreement with previously reported values [144] resembling a P2/m space group.

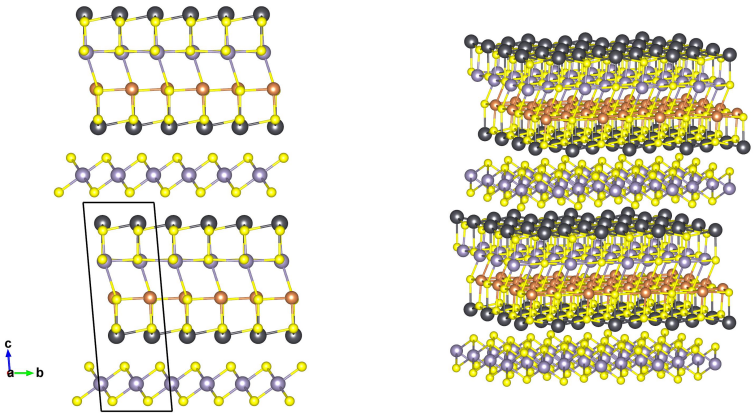

Figure 4.1: (color online). (left) 2D and (right) 3D sketches of the crystal structure of franckeite: the Q layer includes MX compounds, where M = Pb^{2+}, Sn^{2+} or Sb^{3+} and X = S, while the H layer includes MX_2 compounds, where M = Sn^{4+} (M can also be Fe^{2+} or Sb^{4+} replacing Sn^{4+}) and X = S.

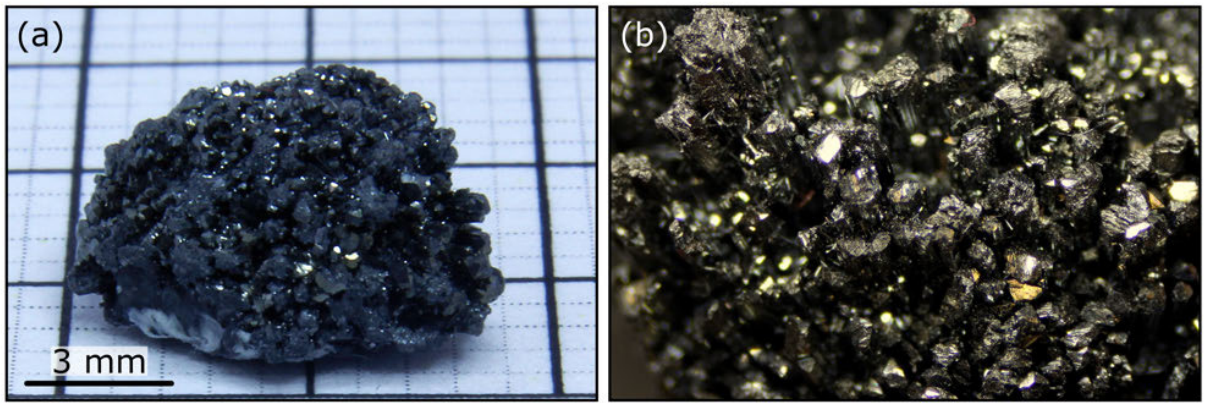

Figure 4.2: Photograph of the franckeite mineral. (b) Zoom-in of the mineral shown in (a).

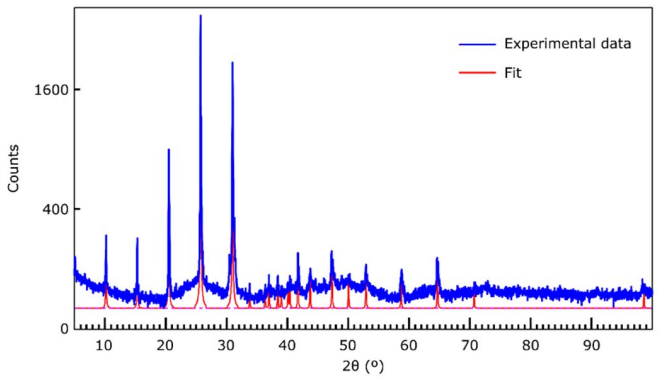

Figure 4.3: (color online). X-ray diffraction pattern measured in powder franckeite.

4.2.3 TEM and XPS of mechanically exfoliates flakes

Transmission electron microscopy (TEM) of mechanically exfoliated franckeite flakes reveal both the high degree of orientation in the stacking of the H and Q layers and its misfit structure. Figure 4.4(a) shows a low magnification TEM image of a flake with regions of different thicknesses, as inferred from the difference in TEM contrast. The TEM image shows regularly spaced fringes which are due to the corrugation of the crystal induced by the interaction between the misfit Q and H layers, as demonstrated by Makovicky et al[141] with cross-sectional TEM in bulk franckeite. Figure 4.4(b) shows a high resolution (HRTEM) image where the atoms of both the Q and H layers can be resolved. The corresponding selected area electron diffraction (SAED) diagram (Fig. 4.4(c)) has consequently been indexed considering franckeite as a stacking of the Q and H layers, respectively described as tetragonal and orthohexagonal[145]. The transmission electron microscopy (TEM) and of mechanically exfoliated franckeite flakes presented here have been carried out by Dr. Emilio M. Pérez group (Universidad Autónoma de Madrid, Spain).

Mechanically exfoliated franckeite flakes using synchrotron micro-X-ray photoemission spectroscopy (XPS) with lateral resolution of B20nm in a photoemission electron microscope (PEEM) have been characterized (ref. [146]). The flakes were transferred onto a metallic Pt surface to avoid sample charging. XPS-PEEM spectra of the four main components of franckeite Sb $3d$, Sn $3d$, S $2p$ and Pb $4f$ are displayed in Fig. 4.4(d) and (e). From the core level fits we distinguish two components for each element: for Sn, we assign the two components to Sn^{2+} and Sn^{4+} from the Q and H structural layers of franckeite, respectively. The Sb 3d core level also presents two components: Sb^{3+} appears in the Q layer with an extra Sb in a different environment. The ratio between Sb and Sn intensities, after normalization to the photoemission cross section and to the microscope transmission, results in an excess of 33% of Sb over Sn. The S $2p$ core level also indicates two different environments, PbS and SnS_2, while Pb $4f$ has a strong doublet (PbS) and another minor component, possibly due to some lead oxide. In the inset of Fig. 4.4(d) we show a low energy electron microscopy (LEEM) image of the flake, appearing as a bright stripe crossing the field of view, with some steps running nearly parallel to one of its edges. From the XPS-PEEM chemical images (inset of Fig. 4.4(e), measured at the Pb $4f$7/2 core level peak), we conclude that franckeite is chemically homogeneous: the image shows a uniform bright stripe through the whole flake, with the same behaviour for all the other chemical constituents.

In addition to the local spectroscopy on a single flake we have performed (in collaboration with Dr. Miguel Ángel Niño, IMDEA Nanociencia, Madrid, Spain) the chemical characterization of the franckeite mineral with standard XPS, using the Al Kα line from a conventional monochromatized X-ray source described elsewhere [147]: several fragments of a few millimeters in size of mineral chips covering a platinum surface were analyzed. There are no photoemission data in the literature about franckeite, but the overview photoemission spectrum (not shown) of the mineral gives the atomic components and contaminants of the franckeite surface: Sb, Sn, Pb and S, as well as the other typical minor components of franckeite Fe and Ag [141, 145, 148] appearing as

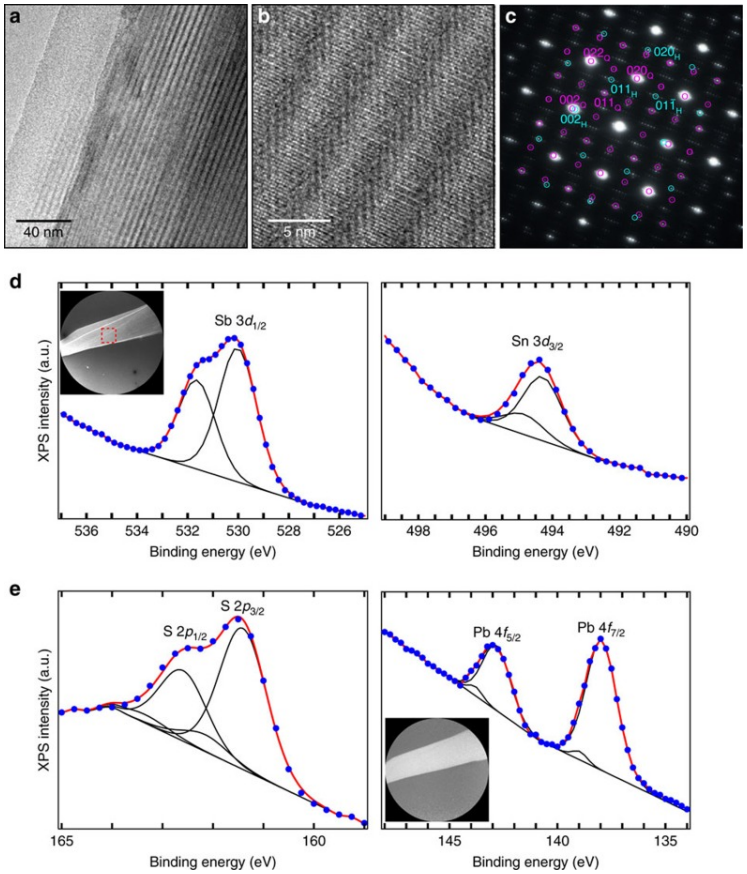

Figure 4.4: (a) HRTEM micrograph of a franckeite sheet exhibiting the characteristic fringes of franckeite due to the corrugation induced by the misfit between Q and H layers. The scale bar is 40 nm. (b) Representative atomic scale HRTEM of an ultrathin franckeite layer. The scale bar is 5 nm. (c) SAED diagram consistent with a misfit layer compound made of PbS and SnS_2 layers: Q (purple) and H sublattices (light blue) lead to the most intense reflections on which superlattice rows of weak intensity are centred. The diagram has been indexed using tetragonal and orthohexagonal vectors for the Q and H phases respectively, according to the orientation and nomenclature defined in ref. 23. (d) Sb $3d3/2$ and Sn $3d3/2$ XPS spectrum acquired with photon energy hν = 600 eV. Inset: LEEM image (the field of view is 50 mm and the electron energy is 0.12 eV), the red square indicates the region of integration where the XPS spectra has been acquired. (e) S $2p1/2$ and $2p3/2$ and Pb $4f5/2$ and $4f7/2$ XPS spectrum acquired with photon energy hν = 230 eV. Inset: XPEEM image at Pb $4f7/2$ core level (the field of view is 50 mm and the photon energy is 230 eV). The strong background in the XPS spectra is due to the tail of secondary electrons cascade.

contaminants oxygen and carbon. The XPS narrow scans give information on the oxidation state and the possible adscription to the different structural layers of the franckeite.

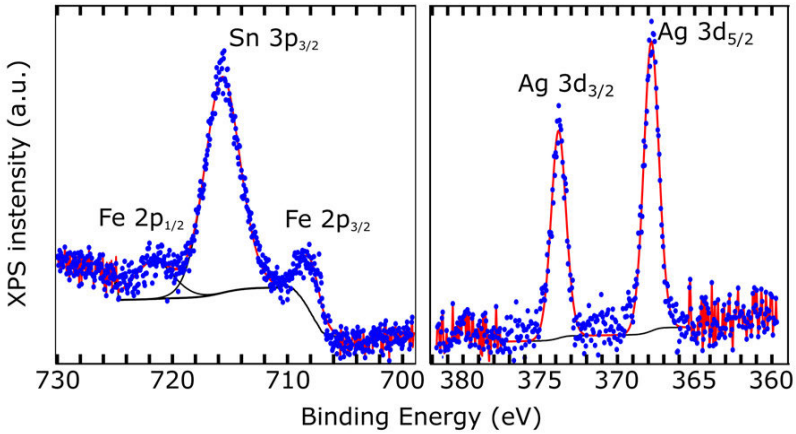

Figure 4.5: XPS spectra of Fe $2p$ region (left), coincident with Sn $3p3/2$ core level and Ag $3d$ region (right).

In the minor components of franckeite, iron is present in a very small concentration, although it appears in the Sn $3p3/2$ narrow scan (Figure 4.5). The broad shape and the position of Fe $2p3/2$ at 708 eV in binding energy, and the distance of 13.8 eV from Fe $2p1/2$, suggest the Fe^{2+} or Fe^{3+} valence state, similar to some iron sulfides (Fe_7S_8, FeS_2). Silver is typical in the cylindrite group of minerals like incaite and potosiite, and it is present in this sample in a small amount: the Ag $3d5/2$ core level (Figure 4.5) appears at 367.8 eV binding energy, which could be compatible with Ag inclusions in an oxide state.

Mechanically exfoliated flakes of franckeite by scanning electron microscopy (SEM) in which the layered structure with large terraces can be depicted in (Figure 4.6).

4.2.4 Absorption spectroscopy

UV-Vis-NIR spectroscopy (Fig. 4.7) of the colloidal suspension prepared from the 100 mg·mL^{-1} powder dispersion in NMP was performed after drop-cast-ing and drying of the liquid sample on a glass slide. This allows the elimination of the solvent C-H bonds which result in intense absorption that hinders light transmission measurements in a wide NIR range. The resulting spectrum shows a continuous decrease of the absorption as the wavelength increases from 300 nm to 2750 nm, followed by a wide absorption band from 2750 nm to 3300 nm, reaching a maximum at ~ 2900 nm (0.43 eV). Together with the absorption onset in the NIR region, the existence of this band is consistent with the narrow bandgap energy determined for franckeite.

obtaining the same shape for the absorption with the maximum at ~ 2900 nm, further confirming the presence of this absorption peak.

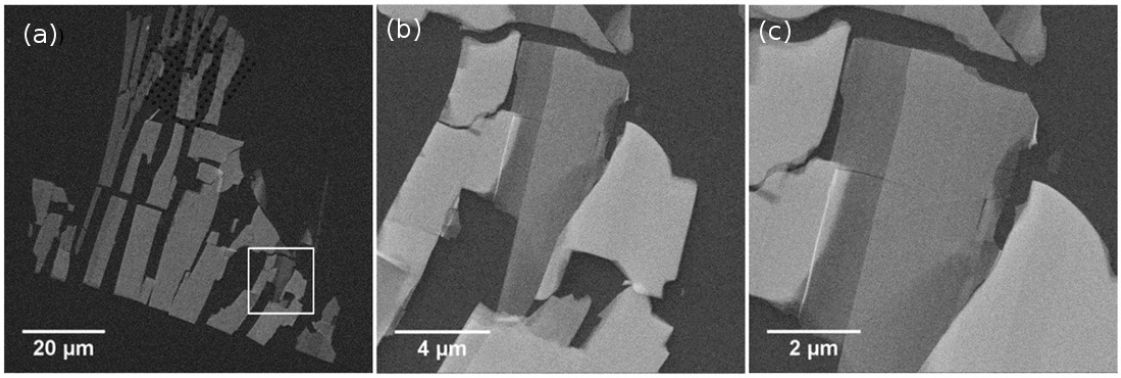

Figure 4.6: (a) SEM image of several ultrathin franckeite layers deposited on a TEM grid. (b), Zoom in on the white squared area marked in a, showing layers of various thicknesses. Conditions: 15 kV, 11 pA, working distance 6.5 mm. c, Zoom in on the image shown in (b).

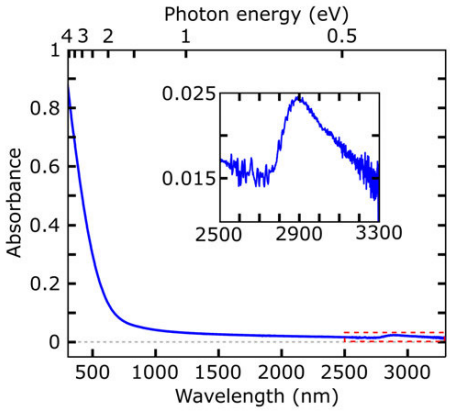

Figure 4.7: UV-Vis-NIR spectrum of a thin film of franckeite colloidal suspension deposited on a glass slide; the sample originates from the liquid-phase exfoliation of a 100 mg·mL^{-1} franckeite powder dispersion. Inset: zoom of the region indicated by a dashed red line that highlights the absorption peak around 2900 nm.

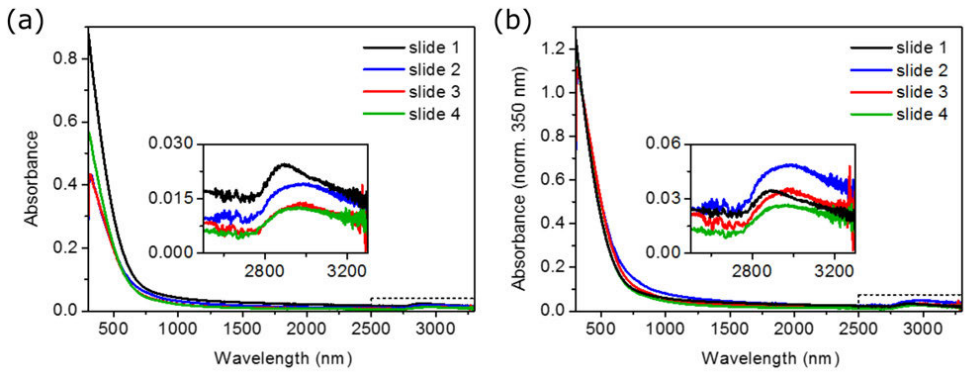

Figure 4.8: (a) Absorption spectra of the sample shown in Figure 4.7 and three replicates performed with other three different glass slides. Inset: zoom in the 2500 nm-3300 nm region. (b) Absorption spectra normalized at 350 nm for the four samples presented in (a). Inset: zoom in the 2500 nm-3300 nm region.

4.2.5 Scanning tunneling spectroscopy

Further characterization of the bulk material has been carried out by means of scanning tunneling microscopy (STM) in order to determine the electronic bandgap of the material. For this purpose, a piece of franckeite (Figure 4.9(a)) is placed on a Au substrate which serves as electrode (indium is used to ensure electrical contact between the two of them), and a mechanically cut Au wire is used as a tip.

Franckeite is then exfoliated to obtain a clean surface. Figure 4.9(b) shows an STM topographic image of the franckeite surface taken with an applied bias voltage of V_{bias} = 1 V at room temperature and ambient pressure, where a step-edge can be identified with a height of ~ 2.3 nm (~ 1 or 2 layers).

The average of a set of 200 STS current-voltage characteristics is shown in Figure 4.9(c), depicting a clear semiconducting p-doped behavior: there is a zero conductance zone around zero bias voltage which extends between two well-defined values, corresponding to the valence band (BV) and conduction band (BC) of the material; the doping of the material can be determined from the fact that the curve is “shifted to the left”, meaning that the Fermi level (corresponding to the zero bias voltage) is closer to the valence band than to the conduction band. The whole set of 200 current-voltage curves is shown in the inset in logarithmic scale where the BV and BC values can be extracted, obtaining BV = -0.25 eV and BC = 0.35 eV, yielding and electronic bandgap of $E_{g,el}$ = 0.6 eV. At this point, the thermal broadening of the bands due to the temperature of the sample must be considered in the calculation, adding $E_t \approx 3.5$kBT = 90 meV at room temperature [149], therefore, the electronic bandgap of franckeite is $E_{g,el}$ = 0.7 eV.

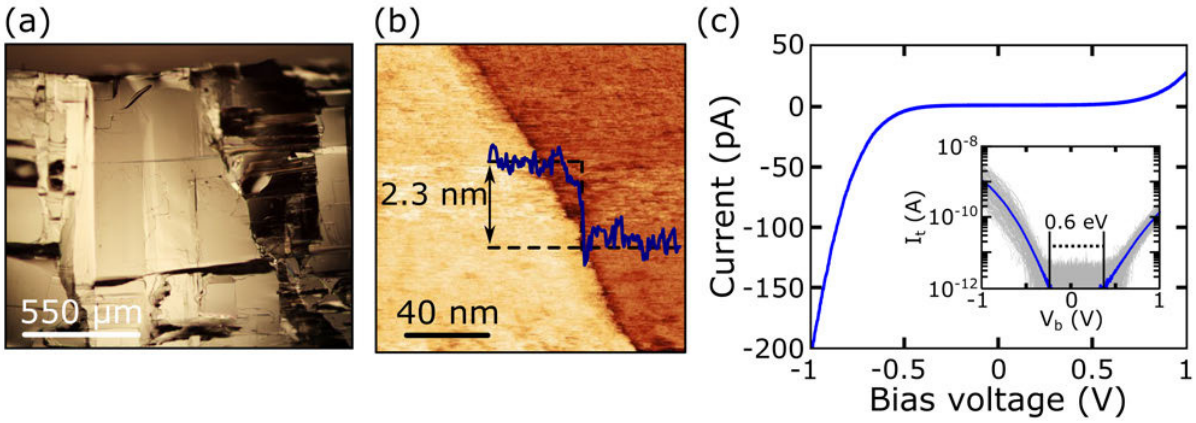

Figure 4.9: Optical microscopy photograph of a piece of franckeite. The material presents large area flat terraces after mechanical exfoliation. (b) STM topographic image of bulk franckeite. (c) STS characterization of franckeite, here we show the average curve obtained from a set of 200 current-voltage curves, which clearly shows a semiconducting p-doped since the zero bias voltage (coinciding with the Fermi level) is closer to the valence band than to the conduction band. Inset: STS current-voltage curves in logarithmic scale, the valence and conduction bands values (-0.25 eV and 0.35 eV, respectively) are highlighted with arrows, yielding an electronic bandgap of ~ 0.6 eV (~ 0.7 eV after correction of the thermal broadening).

4.3 Electronic structure of Franckeite

Calculations of the electronic properties of franckeite are based on the framework of DFT, as implemented in the Quantum ESPRESSO package [115]. The GGA of Perdew-Burke-Ernzerhof (GGA-PBE) was adopted for exchange-correlation functional [116]. Part of the calculations were also performed using the hybrid nonlocal exchange-correlation treatment that incorporated 25% screened Hartree-Fock exchange, the HSE06 functional [150, 151]. The HSE functional, with its fraction of screened short-ranged Hartree-Fock exchange, yields reasonably accurate predictions for energy band gaps in semiconductors [152]. The electron-ion interaction employed in the calculations is described using the norm-conserving Troullier-Martins pseudopotentials [153]. The energy cut-off for the plane wave basis set is set to 60 Ry with a charge density cut-off of 240 Ry. We have used a Monkhorst-Pack scheme with a 5 × 5 × 3 k-mesh for the Brillouin zone integration for the supercell (22 atoms). In some cases, the spin-orbit coupling, important for the heavy elements considered here, is included in the self-consistent calculations of electronic structure.

4.3.1 (PbSnS) and SnS_2-based franckeite

The franckeite structure exhibits a long-range one-dimensional transversal wave-like modulation and a non-commensurate layer match in two dimensions [141]. This will not be taken into

account since it would be computationally too expensive and it is expected to only introduce minor corrections to the results.

In this sense, we first investigate the band structure of individual H and Q layers (Fig. 4.10(a) and (b), respectively). In these calculations we consider PbSnS and SnS_2 compounds, ignoring the influence of substitutional Sb or Fe atoms. For the H layer (Fig. 4.10(a)), using the standard generalized gradient approximation (GGA) to the functional, we obtain an indirect bandgap at X of ~ 1 eV that increases to 2 eV using HSE06. For the Q layer (Fig. 4.10(b)), our calculations yield a semimetal with a gap at X of ~ 0.5 eV using GGA and ~ 0.7 eV with HSE06.

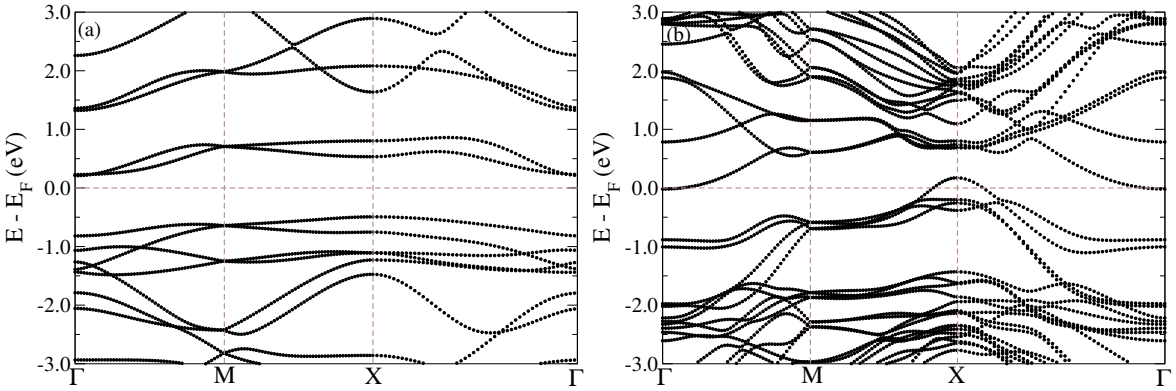

Figure 4.10: (a) GGA band structure of the H and (b) Q layers.

The band structure of the bulk crystal formed by alternate stacking of Q and H layers with the same composition as that of the individual layers, results in two sets of bands separated by a small gap of ~ 0.5 eV at X point (Figure 4.14(c)). Although the Fermi level lies below the valence band, a further investigation of the role played by substitutional Sb atoms (discussed in the next section) shows that the Fermi level is shifted upwards when the material is doped with Sb. These results can be compared with the electronic bandgap measured by means of scanning tunneling spectroscopy (STS) on bulk franckeite crystals, where we observe an electronic bandgap of ~ 0.7 eV with the valence band edge closer to the Fermi level, further confirming the *p*-type doping of the material (also confirmed by the thermopower measurements).

4.3.2 Semiconductor heterostructure

Most interesting semiconductor devices usually have two or more different kinds of semiconductors. These heterostructures show properties that cannot be achieved with only one component. In this sense, one question to be answered is: how does one figure out the relative alignment of the bands at the junction of two different semiconductors? The answer can be obtained if one measures all band energies with respect to one value. This value is provided by the vacuum level (shown by the dashed line in the Figure bellow). The vacuum level is the energy of a free electron (an electron outside the semiconductor) which is at rest with respect to the semiconductor. The

electron affinity, denoted by χ (units: eV), of a semiconductor is the energy required to move an electron from the conduction band bottom to the vacuum level and is a material constant. The electron affinity rule for band alignment says that at a heterojunction between different semiconductors the relative alignment of bands is dictated by their electron affinities, as shown in the Figure bellow. The electron affinity rule implies that the conduction band offset at a heterojunction interface is equal to the difference in the electron affinities between the two semiconductors. This is shown in the band diagram below. According to the electron affinity rule the conduction band offset ΔE_c is given as

$$\Delta E_c = q(\chi_2 - \chi_1) \tag{4.1}$$

where χ_2 and χ_1 are the electron affinity of semiconductors 2 and 1, respectively. The valence band offset is then,

$$\Delta E_V = q(E_{g_1} - E_{g_2}) - \Delta E_c \tag{4.2}$$

Note that,

$$\Delta E_c + \Delta E_V = \Delta E_g \tag{4.3}$$

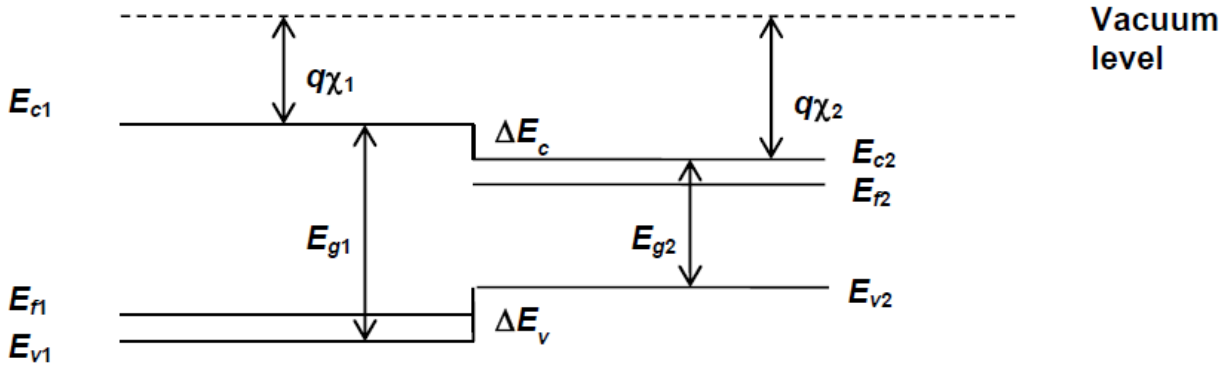

Figure 4.11: Relative positions of valence/conduction band, gap energy and Fermi level for two generics semiconductors.

Depending upon the difference between χ_1 and χ_2 we could have type I, type II, or type III heterojunction interfaces, as shown below.

In Type I heterostructures, the band gap of one material entirely overlaps that of the other and the potential discontinuities for the conduction band, ΔE_c, and for the valence band, ΔE_v. In Type-II heterostructures, $E_{v_1} > E_{v_2}$ and ΔE_c may or may not be larger than E_{g_1}. Also, E_{g_2} is not necessarily smaller than E_{g_1}. Heterostructures of Type-II, with $\Delta E_c < E_{g_1}$ have been named Type II-staggered. Both the conduction-band edge and the valence-band edge of one material being lower than the corresponding band edges of the other material, electrons are confined in one material, while holes are confined in the other material. Type III heterostructures are formed by the combination of a semimetal with inverted bands and a semiconductor.

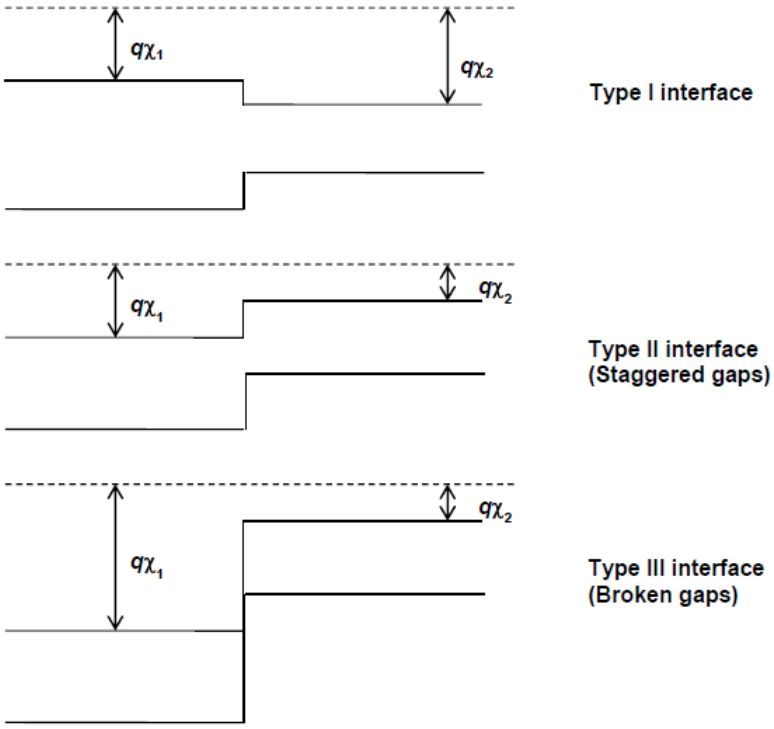

Figure 4.12: Energy band diagram of type I, type II, and type III heterojunction interfaces.

In order to investigate the band alignment on the franckeite, first, we calculate the charge transfer between the Q and H phases, using the Bader charge analysis method [154] with the code developed by the Henkelman's group [155].

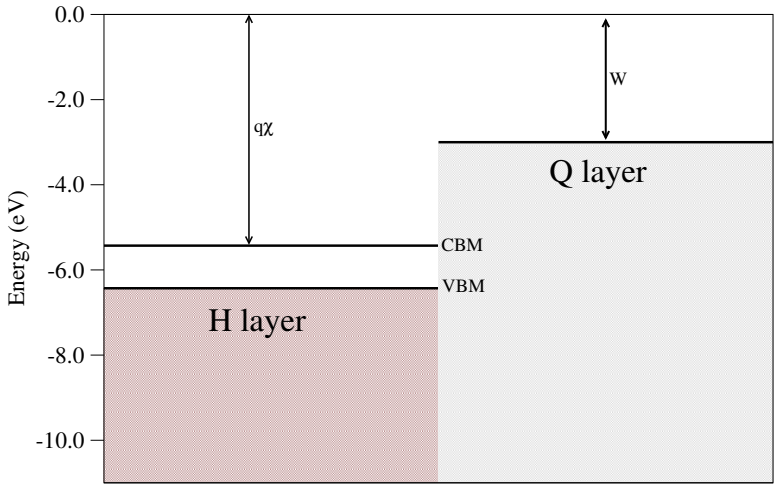

Figure 4.13: Band alignment based on the work function (W) of Q layer (semimetal) and electron affinity χ of H layer (semiconductor). (q is the electron charge).

The amount of charge transfer between Q phase and H phase is about 0.5 electrons (per unit cell) from Q phase to the H phase. We employ the average electrostatic potential technique [156] to compute the valence band maximum (VBM) and conduction band minimum (CBM) of the isolated components (4.13). The energy positions are aligned with respect to the vacuum level. For the H phase we find an electronic affinity of ~ 5.4 eV. The work function for the Q phase is ~ 3.0 eV. The finding that Q-H is metallic is a consequence of the alignment of the bands of the Q and H structure (see Fig. 4.13 and Fig. 4.14(c)).

In the band structure shown in Figure 4.14, it is shown that the valence band wavefunctions correspond to the H layer while the conduction band wavefunctions belong to the Q layer, much in analogy with an artificial type-II semiconducting heterostructure [157].

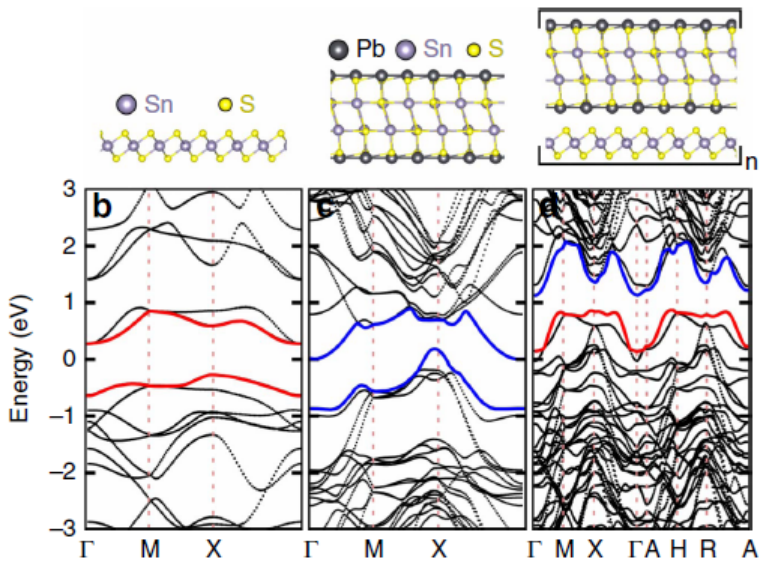

Figure 4.14: (a) Calculated band structure for the Q layer indicating the valence band maximum (VBM) and conduction band minimum (CBM) (red lines). (b) Calculated band structure for the H layer indicating the valence band maximum (VBM) and conduction band minimum (CBM) (blues lines). (c) Calculated band structure for the franckeite crystal that presents a bandgap of ~ 0.5 eV. The valence band is given by the H layer (red line), while the conduction band is given by the Q layer (blue line), suggesting that franckeite is a type-II heterostructure.

In Figure 4.15 it is shown a projection of the crystal structure (Figure 4.15(a)) with the corresponding Bloch states (Figure 4.15(b)), where the blue areas represent the Bloch states corresponding to the blue band in Figure 4.14(c) and the red areas represent the Bloch states in the in the red band in Figure 4.14(c).

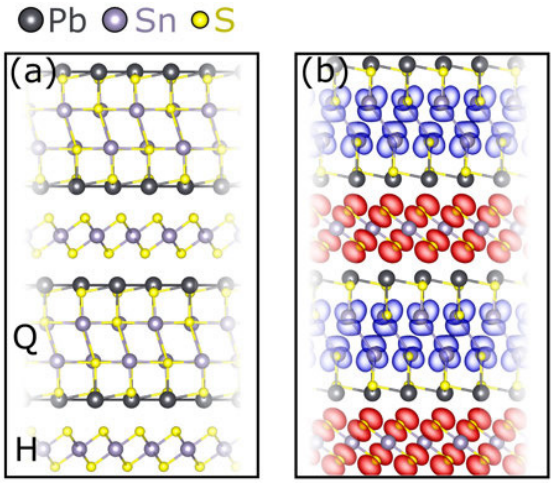

Figure 4.15: (a) Crystal structure of franckeite indicating the H and Q layers. (b) Bloch states in franckeite in which the valence (red) and conduction (blue) bands are represented.

4.3.3 Thickness dependent band structure

Figure 4.16 shows the evolution of the calculated band structure with the number of layers. It is found that the band structure topology and the bandgap, unlike most studied 2D semiconductors, where the reduction of the thickness is usually followed by a sizeable increase of the bandgap due to quantum confinement in the out-of-plane direction, was not significantly changed with a thickness from 1L to 3L, being essentially preserved up to the bulk calculation with an infinite number layers.

4.3.4 Sb-doped franckeite

In the previous section the density functional theory calculations of the band structure of franckeite considering that the crystal is composed of only PbSnS and SnS_2 layers are shown. Nevertheless, it is found that the composition of franckeite includes Sb substitutional atoms replacing Sn atoms which may donate one more electron to the system as a cation in the H layer. The calculations are now computed for a 50% and 100% substitution, i.e., 50% (or 100%) of the Sn atoms have been replaced by Sb atoms in the H layer. In Figure 4.17(a) it is shown the calculated band structure of franckeite composed only by PbSnS and SnS_2, where a bandgap of ~ 0.4 eV with the Fermi level lying below the valence band is found. When an Sb substitution of 50% is introduced (Figure 4.17(b)), one of the valence bands becomes almost fully occupied, while for a 100% substitution (Figure 4.17(c)) both bands are essentially full, leaving a small concentration of holes in the system. The gap has been closed at this stage, but this can be attributed to the known deficiencies of the standard approximation to the density functional that has been used and it is expected to remain open in reality. Substitutional Sb in the Q slab or substitutional Fe in

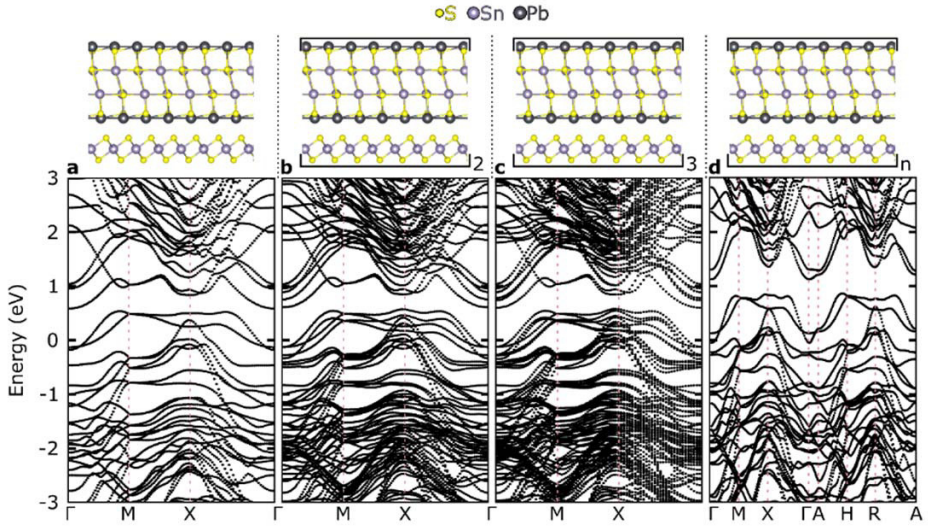

Figure 4.16: The evolution of the band structure of Franckeite with 4 increased thickness for (a) n = 1. (b), n = 2. (c), n = 3 and (d), bulk.

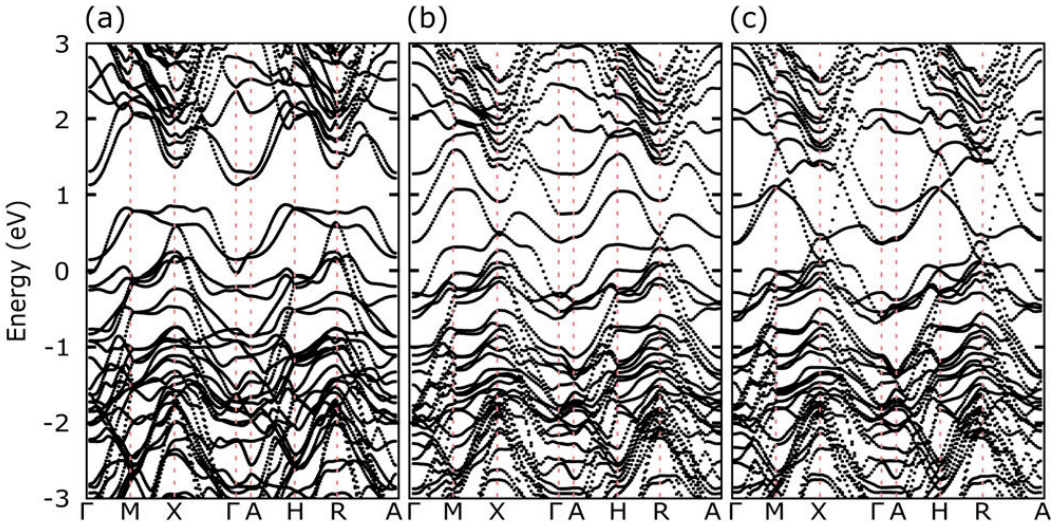

Figure 4.17: (a) Calculated band structure of franckeite without Sb. (b) Calculated band structure of franckeite when 50% of the Sn atoms have been replaced by Sb atoms in the H layer. (c) Calculated band structure of franckeite when 100% of the Sn atoms have been replaced by Sb atoms in the H layer.

the H layer, as well as an increase in the percentage of Pb in the Q slab, does not fundamentally change the spatial separation of electrons and holes in the heterostructure. The saturation with Sb in the H layer, maybe beyond nominal concentration values, seems to be determinant for the semiconducting behavior to emerge, but this coincides with the strong presence of Sb^{4+} observed in our samples by micro-XPS (section 4.2.3) and EDX (section 4.2.3).

Now we proceed to investigate the case in which the substitutional Sb atoms appear in both the Q and the H layer. We fix the amount of Sb in the Q layer at a substitution of 50% of the Sn atoms, while we change the amount of Sb from 0% (Figure 4.18(a)), 50% (Figure 4.18(b)) and 100% (Figure 4.18(c)) in the H layer. Here we observe that the amount of Sb doping is crucial to open a gap in the band structure and, in the situation of 50% Sb, 50% Sn in the Q layer and 100% Sb in the H layer, a minimum bandgap of ~ 0.2 eV appears.

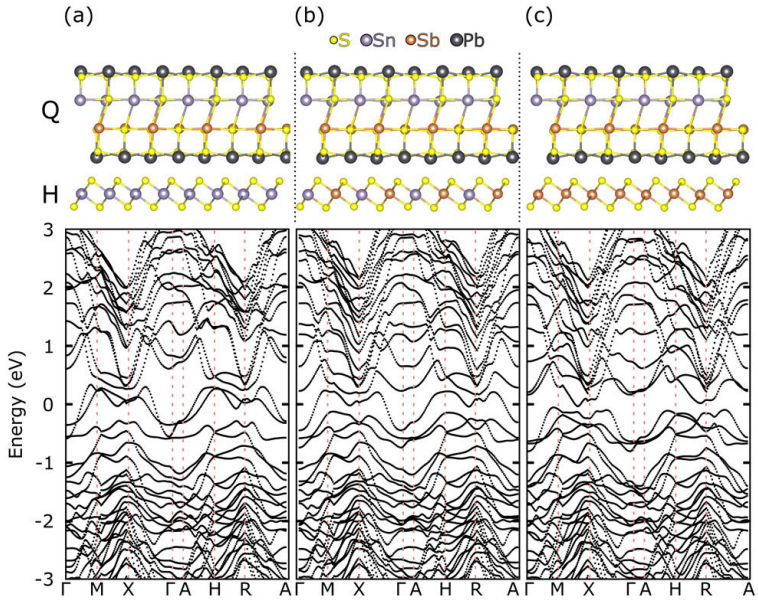

Figure 4.18: (a) Calculated band structure of franckeite with 50% Sn and 50% Sb in the Q layer and 0% Sb in the H layer. (b) Calculated band structure of franckeite with 50% Sn and 50% Sb in the Q layer and 50% Sn and 50% Sb in the H layer. (c) Calculated band structure of franckeite with 50% Sn and 50% Sb in the Q layer and 100% Sb in the H layer.

These results confirm that, although these calculations are simple approaches to the actual franckeite structure, the presence of Sb in the franckeite composition is changing the band structure in such a way that it opens a small bandgap and provides a p-doping.

4.3.5 Band structure with SOC

As a heavy element such as Pb is present in the Q layers, relativistic effects are expected to be large and have an appreciable effect on the electronics properties. To account for such relativistic

effects, spin-orbit coupling (SOC) is here included in the calculations with the GGA functional. For the H layers, as shown Figure 4.19(a), the inclusion of SOC did not change the band structure significantly, and, consequently, the band gap. On the other hand, in the case of Q layers and franckeite crystal Figure 4.19(b) and (c), the band gap has slightly decreased when SOC is taken into account.

Table 4.1: Fundamental band gaps (in eV) of H layer, Q layer, franckeite crystal and franckeite with 50% Sn and 50% Sb in the Q layer and 100% Sb in the H layer.

	GGA-PBE	GGA-PBE + SOC	HSE06
SnS_2	0.95	0.95	2.00
PbSnS	0.50	0.30	0.70
Franckeite	0.50	0.35	0.75
Franckeite (Q-Sb/Sn and H-100% Sb)	0.20	0.03	0.50

To be precise, as shown in Table 4.19, the direct gap at X has decreased by 0.20 eV in the PbSnS structure (Q layer) and the band gap at X has decreased by 0.15 eV in the franckeite structure, almost closing the gap.

As expected, the inclusion of SOC closes the band gap for the case of 50% Sb and 50% Sn in the Q layer and 100% Sb in the H layer, as shown in Figure 4.20. This gap closing should, however, be compensated with the use of HSE06 functional.

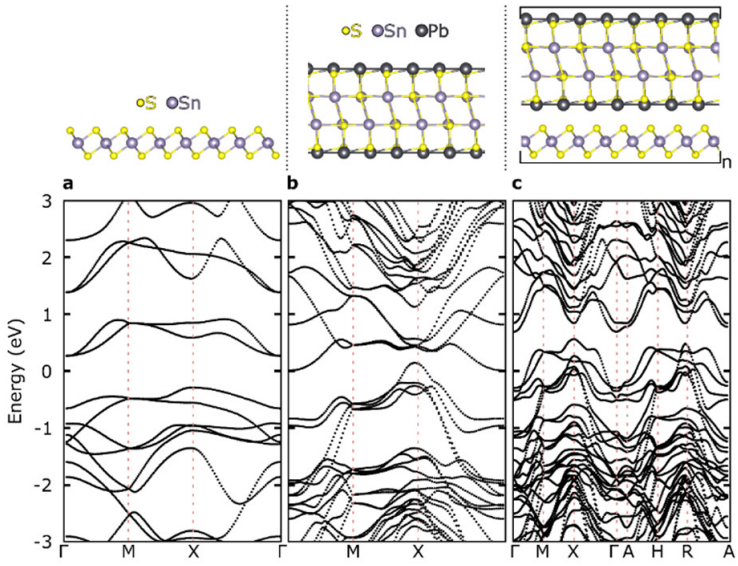

Figure 4.19: (a) SnS_2 (H layer). (b) PbSnS (Q layer) and (c) bulk franckeite from DFT/PBE with spin-orbit coupling.

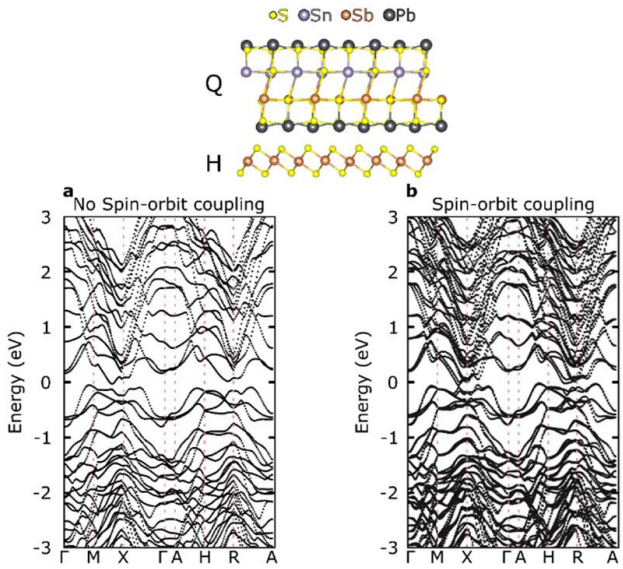

Figure 4.20: (a) Calculated band structure of franckeite with 50% Sn and 50% Sb in the Q layer and 100% Sb in the H layer without considering SOC. (b) The same but considering SOC.

4.4 Conclusion

In summary, in this chapter, it has been shown that bulk franckeite can be exfoliated both mechanically and in liquid phase to afford the first naturally occurring quasi 2D van der Waals heterostructure. The structure and properties of ultrathin flakes of franckeite have been studied extensively from both theory and experiment. Franckeite nanosheets show a very narrow bandgap < 0.7 eV, p-type conductivity, type-II heterostructure and are highly stable under ambient conditions, both as mechanically exfoliated flakes and as colloidal suspensions.

We study the influence of spin-orbit couppling, the evolution of the calculated band structure with the number of layers and the effect of Sb-doping on the electronic properties. We demonstrated that, as expected, the inclusion of SOC closes the band gap for the case of 50% Sb and 50% Sn in the Q layer and 100% Sb in the H layer. It is found that the band structure topology and the bandgap was not significantly changed with a thickness from 1L to 3L, being essentially preserved up to the bulk calculation with an infinite number layers. We also observe that the amount of Sb doping is crucial to open a gap in the band structure and, in the situation of 50% Sb, 50% Sn in the Q layer and 100% Sb in the H layer, a minimum bandgap of ~ 0.2 eV appears. These results confirm that, although these calculations are simple approaches to the actual franckeite structure, the presence of Sb in the franckeite composition is changing the band structure in such a way that it opens a small bandgap and provides a p-doping.

These features make it a unique addition to the still rather small library of experimentally investigated 2D materials. As validation for its potential technological application, have been

constructed prototype photodectectors based on mechanically exfoliated few-layers crystals, as well as a *p*-*n* junction made by stacking an MoS_2 flake and a franckeite flake.

CHAPTER 5

HIGH CURRENT DENSITY ELECTRICAL BREAKDOWN OF TiS_3 NANORIBBON-BASED FIELD-EFFECT TRANSISTORS

5.1 Introduction

Two-dimensional materials have been proposed as prospective candidates to replace conventional semiconductors in electronic devices owing to their attractive properties such as high on/off ratios when integrated in field-effect devices, high carrier mobilities, and minimal influence from short-channel effects [12, 158]. Nevertheless, one of the central considerations in the continued miniaturization of solid state devices is the increase in current density passing through the device that leads to electrical breakdown due to Joule heating or related phenomena [12, 41, 159]. Therefore, nanomaterials that can withstand high current densities are highly sought after for electronic applications and the study of their thermal stability is crucial to improved performance and general device stability.

Apart from transition metal dichalcogenides such as MoS_2, which have already proven to be efficient materials for electronic applications [2, 160, 161], other materials have arisen as promising candidates for replacing the common semiconductors in electronics and optoelectronics [4, 162, 163]. Titanium trisulfide (TiS_3) is a material from the transition metal trichalcogenides family that possess a relatively narrow bandgap of 1 eV [24, 26] and can be isolated as mono- or few-layer nanoribbons and nanoplates [25, 164]. TiS_3 nanoribbons have already shown remarkable field-effect characteristics [25, 164, 165], ultrahigh photoresponse to NIR light, predicted carrier mobilities up to 104 $cm^2\ V^{-1}\ s^{-1}$ and in-plane anisotropy [166, 167].

In this chapter, we present a study of the electrical breakdown and thermal stability of TiS_3. Through density functional theory (DFT) calculations we analyze the energies required for vacancy formation in TiS_3 crystals and find that an oxygen activated sulfur desorption is the

most plausible scenario. We will also study the thermal stability of the material for applications in field-effect devices by electrical breakdown characterization. A thermogravimetric analysis of bulk TiS_3 is performed and the results with density functional theory and kinetic Monte Carlo calculations are compared.

5.2 Crystal structure and synthesis

TiS_3 is a layered material belonging to the monoclinic $ZrSe_3$-type crystal structure shown in Figure 5.1 [168]. It possesses a chain structure of trigonal prisms stacked one of top of the other in which each Ti atom is coordinated to six S atoms at the corners and another two S atoms in the neighbor chains. The prisms are connected, forming a chain along the b axis, while they are bonded to neighboring chains, forming a sheet-like unit. The b axis chains make the material highly anisotropic [20]. The layers are stacked on top of each other along the c axis by van der Waals bonds, allowing to mechanically exfoliate the bulk material to a few-layer structure.

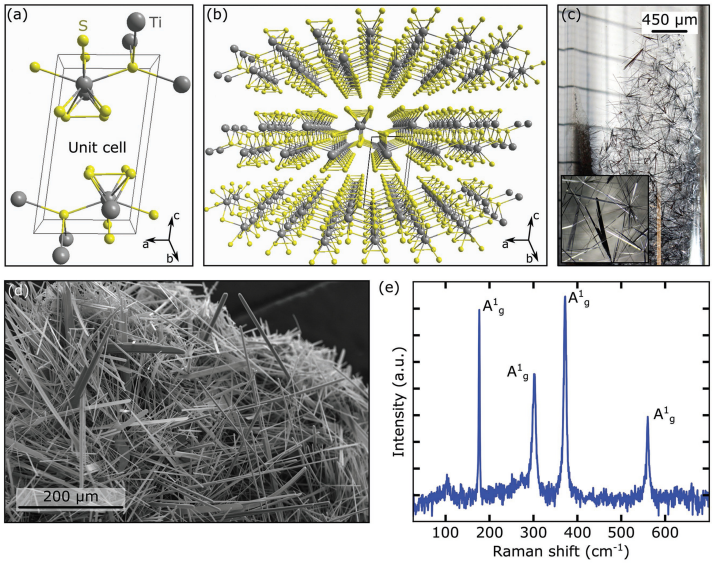

Figure 5.1: a) Artistic representation of the TiS_3 unit cell where the gray spheres represent the Ti atoms and the yellow spheres represent the S atoms. b) Artistic representation of the layered crystal structure of TiS_3. The unit cell is indicated by solid black lines. c) Photograph of TiS_3 inside the ampoule used to grow the material. Inset: magnified photograph of TiS_3 ribbons. d) SEM image of the TiS_3 powder showing the nanoribbon morphology of the material. e) Raman spectra acquired in the TiS_3 powder

The synthesis of bulk TiS_3 is accomplished by a solid-gas reaction between Ti powder ($\simeq$ 1 g, Goodfellow, 99.5% purity) and S gas produced by heating S powder ($\simeq$ 1.4 g, Merck, 99.99% purity) inside vacuum-sealed ampoules at 500 °C with an S/Ti molar ratio = 3 during 10 days. Figure 5.1(c) shows photographs of the resulting TiS_3 ribbons within the ampoule after growth.

In Figure 5.1(d), we show a scanning electron microscopy (SEM) image of the TiS_3 powder where ribbons with different thicknesses and lengths can be clearly identified. The quality and crystal structure of the synthetized material is confirmed by Raman spectroscopy (Figure 5.1(c)(e)), where vibrational modes ($A1_g$) corresponding to TiS_3 can be distinguished (175, 300, 370, and 557 cm^{-1}) [164, 169].

5.3 TiS_3-based field-effect transistors

Field-effect transistors are fabricated based on few-layer TiS_3 nanoribbons obtained by mechanical exfoliation of bulk material (the samples are fabricated by Prof. Herre van der Zant's group, Delft University of Technology, The Netherlands) obtaining few-layer nanoribbons with thicknesses ranging between 15 and 35 nm, $\simeq$ 17-40 layers). The exfoliated nanoribbons are then transferred to a SiO_2 substrate (285 nm thickness) thermally grown on a highly p-doped Si substrate by a deterministic transfer method [10]. Briefly, a polydimethylsiloxane (PDMS) stamp (Gelfilm from GelPak) is placed on bulk TiS_3 and peeled off fast, removing several nanoribbons with different thicknesses, which are cleaved again by peeling with another PDMS stamp. The stamp is then placed on the SiO_2/Si(p+) substrate and removed slowly, leaving the exfoliated material on the surface. We use standard e-beam lithography and lift-off procedures to define the metallic contacts (5 nm Ti/50 nm Au). A SEM image of representative devices is shown in Figure 5.2(a) and (b). The electrical characterization of the devices was carried out in a high vacuum (pressure lower than 10^{-5} mbar) probe station. The current-voltage characteristics (I_{ds}-V_{ds}) of one device is shown in Figure 5.2(c) and the transfer curve (current passing through the device while sweeping the back gate voltage for a fixed V_{ds}, I_{ds}-V_{ds}) shows n-type behavior with $\simeq$ 103 on/off ratio (Figure 5.2(d)) and off-state current of $\simeq$ 530 pA. The lower on/off ratio is most likely a result of midgap electronic states from sulfur vacancies [25].

From the transfer curve we extract the FET mobility using the following equation:

$$\mu = \frac{L}{WC_iV_{ds}}\frac{\partial I_{ds}}{\partial V_g} \tag{5.1}$$

where L and W are the channel length and width, respectively, and C_i is the capacitance per unit area to the gate electrode. Using Equation 5.3 and a parallel plate capacitor model (L = 500 nm, W = 100 nm, $C_i = \epsilon_{SiO_2}/d_{SiO_2}$ = 1.23 $\times$ 10^{-4} F m^{-2}, with d_{SiO_2} the thickness of the SiO_2 substrate), we estimate a two-terminal mobility of $\simeq$ 1 cm^2 V^{-1} s^{-1}, similar to the one reported for TiS_3 nanoribbons FETs [25]. Here we have to take into account that the measurement is done with two terminals, what is known to give an underestimated value for the mobility.

Figure 5.3 shows an AFM scan of the device used to estimate the contact resistance using the transfer length method (TLM). All possible combinations of two electrodes were used in order to extract 10 data points of resistance as a function of channel length. From a linear fit of the data in Figure 5.3(b), we estimate a contact resistance of 8.40 $\pm$ 4.60 M$\Omega/\mu m$. The measurements

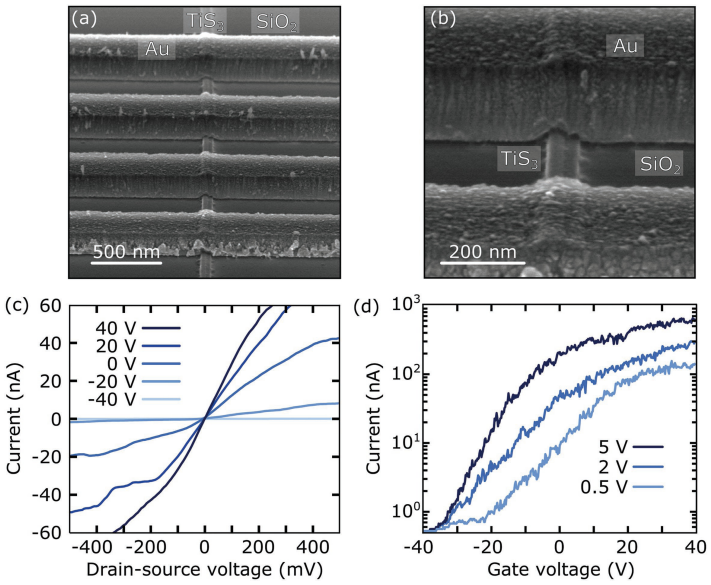

Figure 5.2: a) SEM image of TiS_3 FET fabricated from one TiS_3 nanoribbon. b) Higher resolution SEM image of one of the TiS_3 FETs shown in (a). c) Current-voltage characteristics of a TiS_3 nanoribbon device for different back-gate voltages. d) Transfer curves of a TiS_3 nanoribbon FET for different drain-source voltages.

were taken at V_g = 0 V and V_b = 500 mV. This value is comparable to MoS_2 transistors with gold contacts [170].

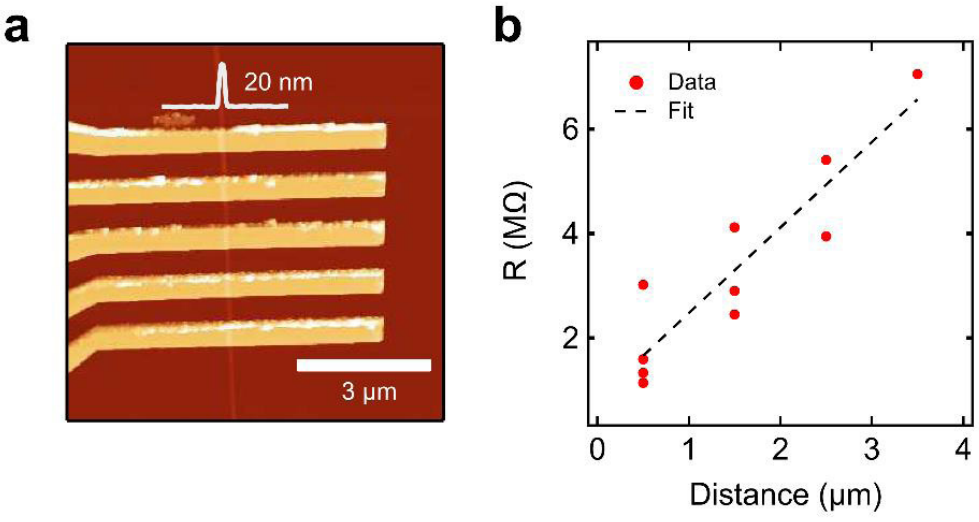

Figure 5.3: (a) AFM image of the TiS_3 nanoribbon device used to estimate the contact resistance. (b) Plot of the two terminal channel resistance (V_b = 500 mV, V_g = 0V) as a function of channel length.

5.3.1 Electrical breakdown of FETs

The electrical breakdown of TiS_3 nanoribbons was studied in air at room temperature in order to investigate the FETs in standard operating conditions for electronic devices; nevertheless, one device was also measured in vacuum, obtaining similar results. The procedure used for determining the electrical breakdown of the devices goes as follows: the back-gate voltage is set to +40 V to turn the device to the ON state, i.e., to reduce the channel resistance. A voltage is applied at one of the two electrodes (source), while the current is measured at the other electrode (drain), establishing a drain-source voltage which is slowly swept (208 mV s^{-1} in steps of 6 mV) from 0 V up to the breakdown voltage, usually between 14 and 20 V (Figure 5.4(a)). The breakdown current and voltage values can be easily identified from the sharp drop of the current to 0 A (green circles in Figure 5.4(a)). Atomic force microscopy (AFM) topographic images of one representative device before and after electrical breakdown are shown in Figure 5.4(b),(c), respectively, where the difference in thickness before (18 nm) and after (4 nm) breakdown is a sign of the degradation of the material. The highest current density at breakdown measured in our TiS_3 FETs is 1.7 × 106 A cm^{-2}, which is among the highest reported when directly compared with the breakdown current density measured for other nanomaterials (multilayer MoS_2 [171], multilayer graphene [172], monolayer graphene [173], Cu [174], TiO_2 [175], Si [176] and GaN [177]), shown in Figure 5.5. This makes TiS_3 a very interesting candidate for field-effect devices requiring high current densities or high power electronics.

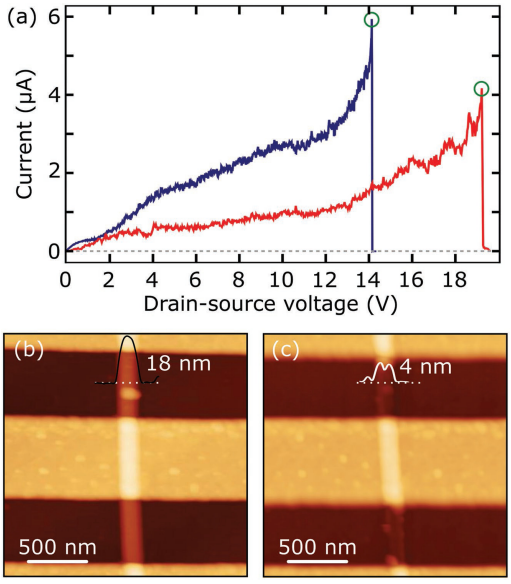

Figure 5.4: a) Current-voltage characteristics during the electrical breakdown process of two TiS_3 devices. The green circles highlight the current and voltage values just before breakdown. AFM topographic images of one device b) before and c) after electrical breakdown, including the AFM line profile that indicates the thickness.

In Figure 5.6 we show the current-voltage trace measured during the breakdown process for one TiS_3 device in vacuum (P < 10^5 mbar). As it can be depicted, the voltage needed to electrically break the nanodevice is in the same order of magnitude that those needed to break the nanodevices in air. The current density at breakdown measured for this device is 9.5·105 A/cm^2, in the same order of magnitude as the devices measured in air.

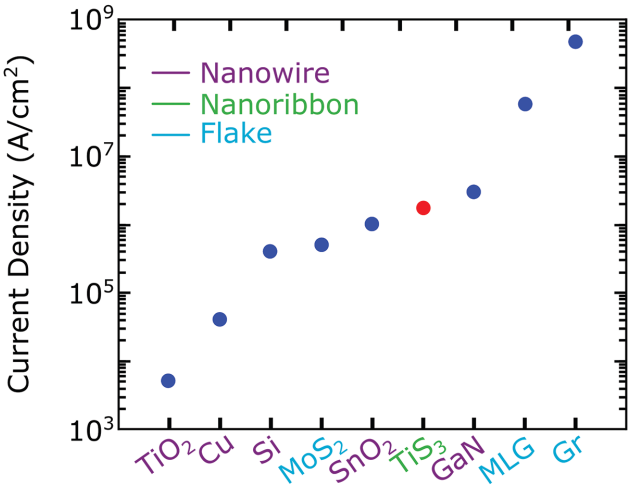

Figure 5.5: Maximum current density at breakdown for different nanomaterials: multilayer MoS_2 [171], multilayer graphene [172], monolayer graphene [173], Cu [174], TiO_2 [175], Si [176] and GaN [177] and TiS_3 (present work).

This result suggests either that the air is not important in the breakdown process or that even a small quantity of oxygen that might be adsorbed on the nanoribbon surface is enough to trigger the electrical breakdown. As it will be discussed later from the TGA measurements it is found that the oxygen adsorbed on the surface is playing an important role in the process.

The current density at breakdown measured for this device is 9.5·105 A/cm^2, in the same order of magnitude as the devices measured in air. This result suggests either that the air is not important in the breakdown process or that even a small quantity of oxygen that might be adsorbed on the nanoribbon surface is enough to trigger the electrical breakdown. As it will be discussed later from the TGA measurements it is found that the oxygen adsorbed on the surface is playing an important role in the process.

A deeper understanding of the breakdown process requires the analysis of the current density at breakdown (JBD). The current density at breakdown is calculated from the current value just before breakdown and the cross-sectional area of the device, which is determined by AFM topographic characterization before breakdown. The measured breakdown current density ranges from 5 × 104 to 1.7 × 106 A cm^{-2} among all devices, with an average value of 6.8 × 105 A cm^{-2}. Figure 5.7 shows the current density at breakdown for all nine devices as a function of the device resistivity ρ, calculated from the conductance just before breakdown. As reported in previous

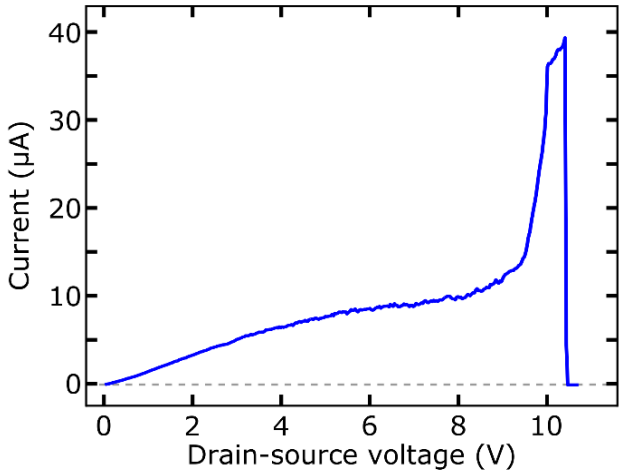

Figure 5.6: Current-voltage curve of a TiS_3 nanoribbon-based device measured in vacuum ($P < 10^{-5}$ mbar). The electrical breakdown occurs at a current density of 9.5·105 A/cm^2, in the same range as the devices measured in air.

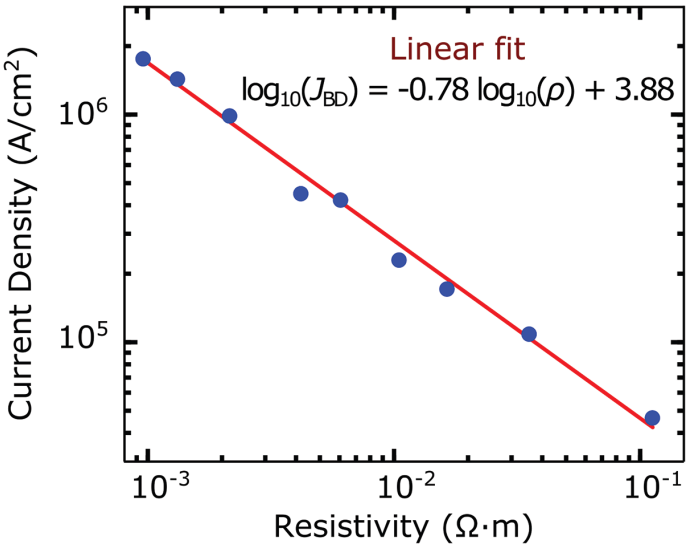

Figure 5.7: Current density at breakdown voltage versus resistivity in logarithmic scale for all the measured devices (blue dots). The red line represents a linear fit which yields a slope of -0.78.

works [178, 179], increasing the drain-source voltage translates into Joule heating that might be responsible for decreasing the contact resistance between the semiconducting material and the electrodes as well as annealing the material, i.e., removing adsorbates, increasing therefore the conductivity of the material, as can be depicted in the current-voltage curves shown in Figure 5.4(a). Taking this into account, the resistivity of the material in this analysis should be calculated prior to breakdown instead of at low-voltage [178, 179].

The expected behavior of the current density as a function of the resistivity for a purely Joule heating process, in which the breakdown occurs by thermal heating, is $J_{BD} \propto 1/\sqrt{\rho}$, which arises from solving the 1D heat equation [178]. A linear fit of the experimental data (J_{BD} as a function of ρ, red line in Figure 5.7) gives a slope of -0.78 with a R^2 value of 0.99, yielding a dependence of the current density with resistivity of the form: $J_{BD} \propto \rho^{-0.78}$. This deviation from $J_{BD} \propto 1/\sqrt{\rho}$ is related to the influence of different phenomena (defects, impurities, electron-hole pairs formation, etc.) in the breakdown process apart from a pure Joule heating process [178–180].

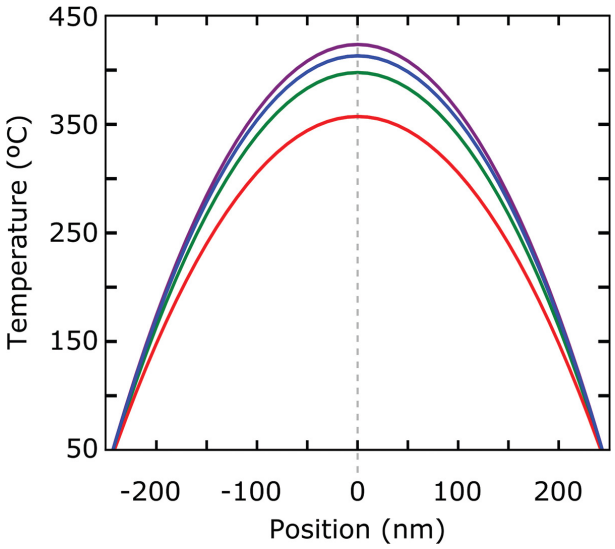

Figure 5.8: Calculated temperature distribution at breakdown along four TiS_3 nanoribbons-based devices using the 1D heat equation. The zero position (dashed gray line) corresponds to the center of the nanoribbon, while the -250 and 250 nm correspond to both source and drain electrodes edges. The highest temperature is reached in the center of the device and oscillates between 350 and 450 °C.

We investigate the nature of the breakdown process by estimating the temperature along the device using the analytical solution to the 1D heat equation [159, 181, 182]:

$$T(x) = T_0 + \frac{p'_x}{g}\left(1 - \frac{cosh(x/L_H)}{cosh(L/2L_H)}\right) \tag{5.2}$$

where T_0 = 300 K and L_H = $(kA/g)^{1/2}$ is the characteristic healing length along the material, p'$_x$ ≈ I^2R/L (with I the current passing through the device, R the corresponding resistance and L

the channel length) is the Joule heating rate in watts per unit length and g ≈ 1/[L(R_{ox} + R_{Si})] is the thermal conductance to the substrate per unit length, with the thermal resistance of SiO_2 and Si. R_{ox} = t_{ox}/(k_{ox}WL) and R_{Si} = 1/(k_{Si}(WL)$^{1/2}$), where t_{ox} is the SiO_2 thickness (285 nm), k_{ox} and k_{Si} are the thermal conductivities of SiO_2 and Si, respectively, and W and L are the channel width and length.

Using Equation 5.3.1 for the TiS_3 devices (with values kTiS_3 = 3.6 W·K^{-1} m^{-1} [183], k_{ox} = 1.4 W·K^{-1} m^{-1}, and k_{Si} = 50 W·K^{-1} m^{-1}), we find that the critical temperature at the center of the nanoribbons is ≈ 400 ± 50 °C (Figure 5.8).

5.4 Density functional theory calculations of activation energies

We study from the density functional theory (DFT) and kinetic Monte Carlo (KMC) simulations the thermal stability of the single layer TiS_3 on the atmosphere with low concentration of the atomic O. We have calculated the activation energies for the desorption of S atoms, SO pair and O atoms on the surface of a single layer of the TiS_3 and TiS_3O_x. We have calculated the total energies of a single layer TiS_3, TiS_3 with a vacancy and TiS_3O_x with SO pair vacancy using the Quantum Espresso package [115]. By starting from the initial lattice parameters extracted in this paper we have built a 3 × 3 supercell to reduce the interaction between vacancies on surface TiS_3. The layers were separated by a 15 Å(vacuum) to minimize interactions between the periodic images. We have therefore optimized the atomic positions with a residual force after relaxation of 0.001 atomic units, for the pristine system, TiS_3 with a vacancy, TiS_3O_x and $TiS_{3-x}O_x$. All the configurations are ionically relaxed using the Broyden-Fletcher-GoldfarbShann's (BFS) procedure. The generalized gradient approximation of Perdew-Burke-Ernzerhof (GGA-PBE) [116] was adopted for exchange-correlation functional, and the Trouiller-Martins norm-conserving pseudo-potential for Ti, S and O is used to model valence electron-nuclei interactions. The energy cut-off for the plane wave basis set is put at 60 Ry with a charge density cut-off of 240 Ry.

DFT calculations related to the loss of S and the influence of O in the transformation from TiS_3 into $TiS_{3-x}O_x$ have been performed trying to model the experimental results. On the basis of the DFT calculations, several active desorption processes that may take place at the experimental temperatures are identified (Figure 5.9): (a) desorption of S atoms, (b) desorption of S atoms due to the interaction with O atoms in the form of SO molecules that leads to the creation of a monovacancy, and (c) creating a divacancy.

We evaluate, in the first place, the viability of the oxidation of TiS_3 surface (before addressing the three processes mentioned above). To this aim we calculate the binding energy of an O atom adsorbed on an S atom from the equation

$$E_b = 1/N_O[E_{TiS_{3+O}} - (E_{TiS_3} + N_O E_{O_2}/2)], \tag{5.3}$$

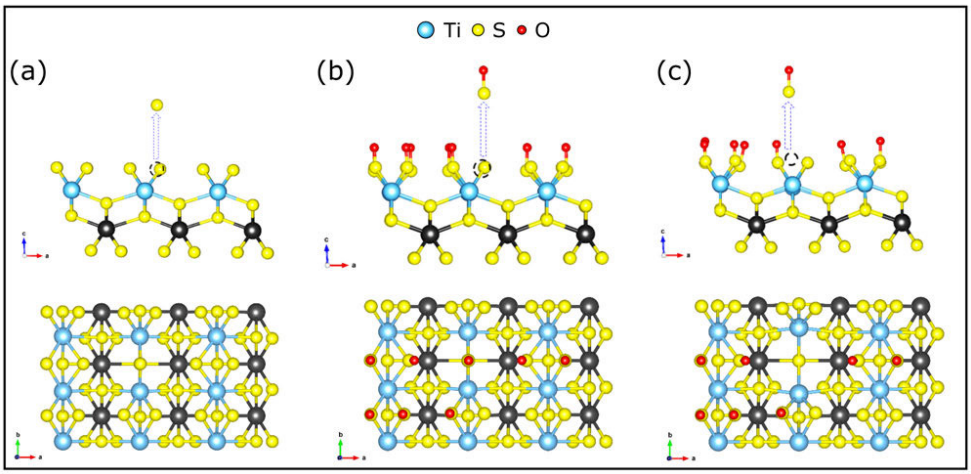

Figure 5.9: Artistic drawing of the different process considered in the DFT calculations. (a) S atoms desorption from the surface. (b) SO pairs desorption from the surface, creating a mono-vacancy. (c) SO pairs desorption from the surface, creating a di-vacancy.

where N_O is the number of O atoms in the supercell used in the calculation, $E_{TiS_{3+O}}$ is the total energy of O-doped TiS_3, E_{TiS_3} is the total energy of pristine TiS_3, and E_{O_2} is the total energy of the O_2 (triplet state) molecule. We obtain a binding energy of -3.74 eV, for our minimum concentration of one O atom per supercell, which is in good agreement with previous theoretical work [184]. The binding energy for other concentrations is shown in Table 5.1. According to the definition above, a negative E_b indicates that the chemisorption is exothermic (energetically favored) for all possible concentration values. Except for the minimal concentration, the binding energy E_b does not appreciably change with this or with the actual distribution of O (see Table 5.1). The actual dissociation of O_2 and accompanying adsorption is an activated process, but the activation energy is smaller than the experimental temperatures for all the paths that we have explored (not shown).

Table 5.1: Binding energy for the oxygen impurities for different concentrations

O surface concentration (per supercell) [%]	Binding energy [eV]
5.5	-3.74
22.5	-2.78
50	-2.58
100	-2.64

Since it appears that the oxidation of the surface is favorable, we now take into account the

possibility of desorption of SO pairs. The formation energies of the vacancies were obtained from

$$E_f = E_v - E_M + E_A, \tag{5.4}$$

where E_A is the energy of the removed isolated atom/pair (S/SO), and E_M and E_v are the total energies of the defect-free and the vacancy-containing layer. The different processes are represented in Figure 5.9, which also depicts the initial (side view) and final (top view) structures. The formation energy of an S-vacancy is 3.33 eV (Figure 5.9(a)) and the structure clearly shows locally reconstructed bonds with the nearest Ti atoms with a bond length of 2.31 Å. The formation energy is almost as high as the energy needed to desorb an O atom from S (3.67 eV), thus both processes will be excluded from our simulations since they are not active at the experimental temperatures. The energy needed to remove a SO pair from our (50% oxidized) surface is, however, much lower: 1.50 eV (Figure 5.9(b)). After the relaxation, the two nearest-neighbor SO pairs present a small distortion around the vacancy, which translates into a formation energy that increases to 1.63 eV when creating a second SO vacancy next to an existing one (not shown). The energy to remove the second SO pair from the same (bridge) site to create a divacancy (Figure 5.9(c)) is 2.72 eV. These results are in good agreement with the activation energies obtained from the nonisothermal Kissinger method [185] (Figure C.3(b)) using the TGA measurements shown in Figure C.2(a), where we find an activation energy of $E_{a,1}$ = 1.5 eV for the first event in the TGA, i.e., SO vacancy formation.

As far as the structural properties at higher temperature are concerned, and in order to obtain some qualitative insight into the formation of TiS_2, we have computed the surface formation energy in the absence and presence of vacancies. The energy required to create a new surface after the split-off of one TiS_3 layer (half of the fundamental Ti_2S_6 unit) is 2.2 eV per cell. The presence of vacancies on the topmost TiS_3 layer does not hinder this process and the energy cost for a detachment of this surface layer (now $TiS_{3,\grave{a}\acute{i}x}$) is similar in energy. Specifically, for full vacancy coverage (one S atom missing per bridge as discussed above) leading to a detached TiS_2 layer we obtain 2.35 eV. These results are in good agreement with the second activation energy, where we find an activation energy of $E_{a,2}$ = 2.05 eV for the second event that leads to TiS_2 formation.

5.5 Object kinetic Monte Carlo algorithm

The KMC calculations have been performed to understand the time evolution of the surface distribution of the vacancies for different temperatures and different vacancy-type defects on monolayer TiS_3. KMC algorithms are powerful techniques to study the dynamics of a system of particles when the different events that those particles can perform are known as well as their probabilities [186]. We use an object kinetic Monte Carlo (OKMC) algorithm, based on the residence time algorithm or Bortz-Kalos-Liebowitz (BKL) algorithm [186, 187]. Typically in

OKMC simulations, a list of possible events is defined with a given probability for each event, Γ_i. This probability usually follows an Arrhenius dependence with temperature

$$\Gamma_i = \Gamma_0 \exp\left(\frac{-\Delta_i}{K_B T}\right) \tag{5.5}$$

where K_B is the Boltzmann constant, Δ_i is the activation energy of the given event, and Γ_0 is the attempt frequency (we assume a reasonable attempt frequency $\Gamma_0 = 10^{13}$/s). Here, the activation energies are related to substitutional and desorption energies. The total rate for all events, R, is then calculated as

$$R = \sum_{i}^{n_e} \Gamma_i N_i \tag{5.6}$$

where ne is the total number of events and Ni is the number of particles that can perform event i. An event is then selected by picking a random number between [0, R]. In this way, one event is selected every Monte Carlo step from all possible with the appropriate weight. Once the event has been selected, a random particle is chosen from all those that can undergo that event. The particle is then moved and the total rate has to be computed again for the next simulation step. At every Monte Carlo step, the time increases by

$$t = -\ln \frac{\xi}{R} \tag{5.7}$$

where ξ is a random number between [0, 1] that is used to give a Poisson distribution of the time.

In this work, we considered a total of four events. However, the event that denotes the formation of the S-vacancy in the single layer of TiS_3 does not interfere in the desorption process due to its high activation energy (3.33 eV), yielding a higher probability for the desorption of the SO-pair, since it is more energetically favorable (1.50-1.63 eV). Thus, the events that actively participate in the desorption process are: SO monovacancy with energies 1.50 and 1.63 eV (these events occur almost simultaneously due to the low energy difference between them) and SO divacancy (2.72 eV).

As a result, we show the evolution of the relative desorption of SO (Δm) atoms on the surface of the TiS_3 first layer as a function of temperature (Figure 5.10) and for the respective time measurements at 1, 5, and 10 min. We observe that the population of SO atoms on the surface start to decrease after $\approx$ 200 °C and that this first process (creation of monovacancies) occurs until $\approx$ 300 °C. The formation of divacancies occurs in the temperature range of 500-650 °C. These results are in good agreement with the TGA measurements shown above (Figure C.2(a)), where the first event takes place in the temperature range between 300 and 400 °C, and are furthermore in agreement with the estimated temperature at breakdown for the FETs, which is $\approx 400 \pm 50$ °C. However, the second event in the TGA measurements (formation of TiS_2) could not be reproduced with the simplified scenario considered in the theoretical calculations. A more thorough study of the different possible reactions at high temperatures lies outside the scope of the current study.

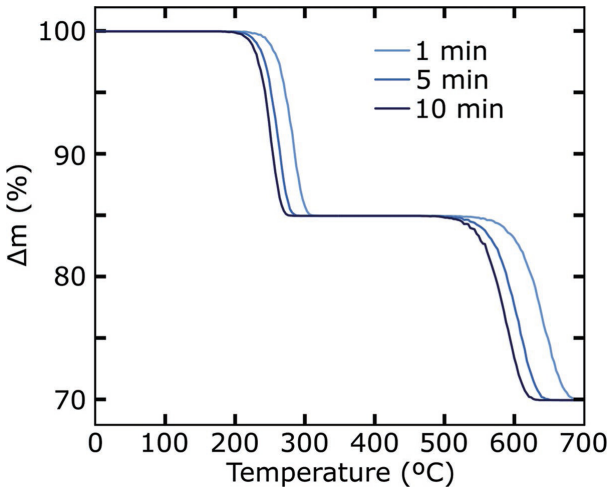

Figure 5.10: Calculated evolution of the relative desorption of SO (Δm) atoms on the surface layer of TiS_3 as a function of the temperature for different time rates: 1 min (light blue), 5 min (medium-dark blue), and 10 min (dark blue).

5.6 Conclusion

In summary, we have studied the thermal mechanisms that may be involved in the electrical breakdown by DFT calculations combined with kinetic Monte Carlo, as well as by TGA measurements in thin films (employed by our experimental collaborators), finding that the creation of vacancies due to the oxidation of the material and the subsequent desorption of sulfur atoms could trigger the degradation and therefore the breakdown of the material in FET's. It was evaluate the viability of the oxidation of TiS_3 surface and we found that that the chemisorption is exothermic (energetically favored) for all possible concentration values. The experimental results are compared with a series of DFT calculations related to the loss of S and the influence of O in the transformation from TiS_3 into $TiS_{3-x}O_x$. On the basis of our DFT calculations, we have identified several active desorption processes that may take place at the experimental temperatures. Futhermore, it was observed that the population of SO atoms on the surface starts to decrease after ≈ 200 °C and that this first process (creation of monovacancies) occurs until ≈ 300 °C. The formation of divacancies occurs in the temperature range of 500-650 °C.

The maximum current density in TiS_3 nanoribbons-based FETs was measured by inducing electrical breakdown in the devices, finding a maximum value of 1.7×106 A cm^{-2}, which is higher than the maximum current density in many other semiconducting low-dimensional materials. These results do not only make TiS_3 a prospective material for high-power nanoelectronics required to stand high current densities but also provide some insight into the thermal mechanisms occurring in nanostructured devices based on this material.

CHAPTER 6

ANTIMONENE: A NEW BIDIMENSIONAL MATERIAL

6.1 Introduction

Very recently antimony has been demonstrated to be amenable to standard exfoliation procedures opening the possibility of studying the electronic properties of isolated few-layers flakes of this material [16]. Antimony is a topological semimetal, meaning that its electronic structure presents spin-split helical states (or Dirac cones) on the surface, but it is still trivially metallic in bulk. Antimonene, on the other hand, may present a much reduced electronic bulk contribution for a small number of layers.

Theoretical calculations predict an electronic band structure suitable for optoelectronics and thermoelectric applications [66, 188, 189]. Single-layer antimonene phases form bilayer and trilayer structures with wide interlayer spacings. In multilayers, this spacing is reduced and eventually the structure changes to 3D pseudolayered bulk crystals.

The work presented in this section has not been published so far and has been performed in collaboration with Prof. Félix Zamora and Prof. Júlio Gómez Herrero groups.

6.2 Crystal structure

The crystal structure of Sb is rhombohedral with the space group D^5_{3d} ($R\bar{3}m$), with two antimony atoms in the trigonal unit cell. Experimental values of this 3D crystalline structure are the lattice constants a = b = 4.31 Å, c = 11.27 Å (at 298 K) [16] and Sb-Sb bond distance 2.91 Å. Our calculated values obtained from full structure optimization are a = b = 4.28 Å , and c = 11.18 Å . In Figure 6.1, the atomic configuration, together with the relevant structural parameters is illustrated. This 3D bulk phase can be viewed as consisting of an ABCABC... type of stacking of the single-layer structure. Each isolated single layer (Antimonene), exhibits a bipartite honeycomb lattice with A

and B sublattices. The two sublattices have different heights, forming a buckled configuration. At the equilibrium state, the Sb-Sb bond length is about 2.89 Å and the height of buckling (h) is 1.64 Å.

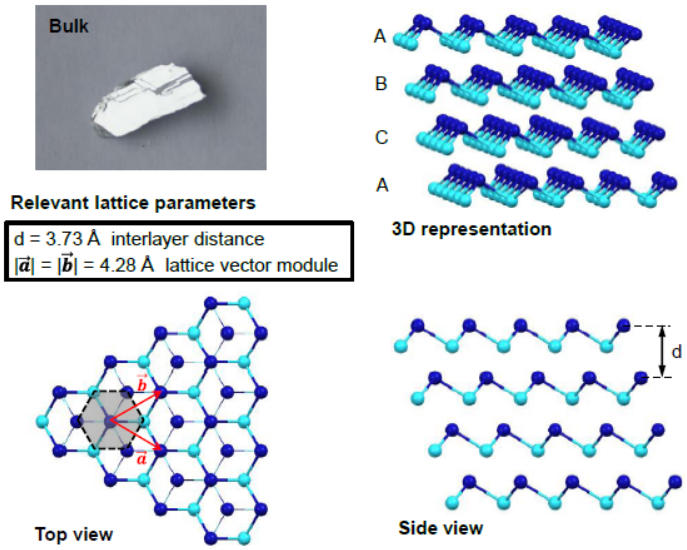

Figure 6.1: Relevant views and parameters of antimony atomic lattice (Extracted from [16]).

6.3 Allotropes and structural stability

The most commonly studied antimonene structure (β-antimonene) is not the only possible one. DFT calculations have been performed for other allotropic forms (see Figure 6.2), including the α, γ, and δ phases [190]. The results have shown that, other than the β structure, the only stable one is the α allotrope. The crystallographic structure of this phase corresponds to a rectangular Bravais lattice with four atoms in the unit cell. Similar in many respects to a black phosphorus monolayer or phosphorene [10], α-antimonene presents two atomic sublayers, where the two unit cell atoms that belong to the same sublayer are not exactly located in the same plane (see Figure 6.2). The relative stability of α- and β-antimonene has been studied by comparing the cohesive energy of the different allotropic forms. Several exchange and correlational functional forms of DFT have been used for this purpose. The α form presents, in general, a larger cohesive energy than the β form when using LDA ($\approx$ 60 meV) and van-der-Waals corrected DFT-D2 ($\approx$ 30 meV), although both phases become almost degenerate when the most standard GGA(PBE) is used instead [190]. Also the phonon free energy has been computed finding that the difference between both phases in the range of temperatures 0-600 K was less than 15 meV/atom. This suggests that both phases are comparable in their structural stability and, in principle, both could be found in experiments. In contrast to β-antimonene, the band gap of α-antimonene is

direct and, in addition, its value is much smaller (≈ 0.2 eV) than that of the β counterpart [191]. Otherwise stated, antimonene must be understood as β-antimonene throughout this work.

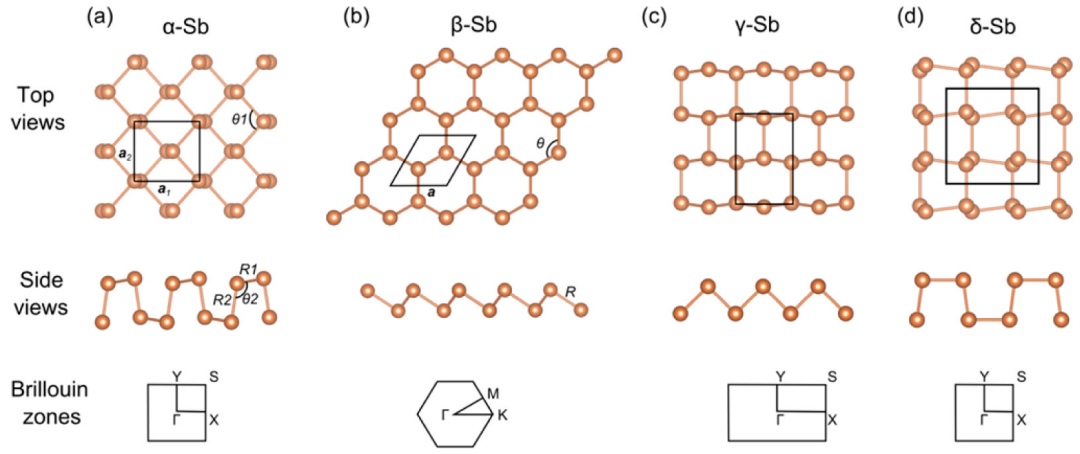

Figure 6.2: Structural configurations of antimonene allotropes: (a) α-Sb, (b) β-Sb, (c) γ-Sb and (d) δ-Sb.(Extracted from [190]).

6.4 Monolayer, bilayer and trilayer Antimonene

First, we gain insight into electronic properties of antimonene considering 1, 2 and 3 layers (BL). As shown in Figure 6.3(a), 1 BL antimonene is a nonmagnetic insulator, the Sb electronic states split into two parts forming a gap around the Fermi level. The indirect band gap is as large as about 0.90 eV calculated within PBE approximation and considering the spin-orbit coupling (SOC), which occurs between the minimum of the conduction band along the Γ-M direction and maximum of the valance band at the Γ point, implying the strong coupling between two surfaces. Calculations employed without SOC (not shown) indicated an indirect band gap 0.20 eV larger. Calculations carried out by HSE show that the DFT band gap is underestimated by 0.52 eV; hence this indirect band gap increases to 1.42 eV after HSE correction.

In the case of two and three BL (see Figure 6.3(a) and (b)), the splitting of $5p$ states decrease with the decline of the coupling, leading to a semimetallic electronic structure.

6.5 Few-layer Antimonene

Shortly before antimonene was the focus of attention by the research community, its bulk parent material had been the subject of an unexpected interest. An elemental bulk material such as antimony happens to be a topological semi-metal on account of an inverted bulk band order [69]. Despite the absence of a bulk gap, its non-zero topological invariant guarantees that antimony features protected topologically surface states (TSS), but coexisting with bulk bands at the Fermi

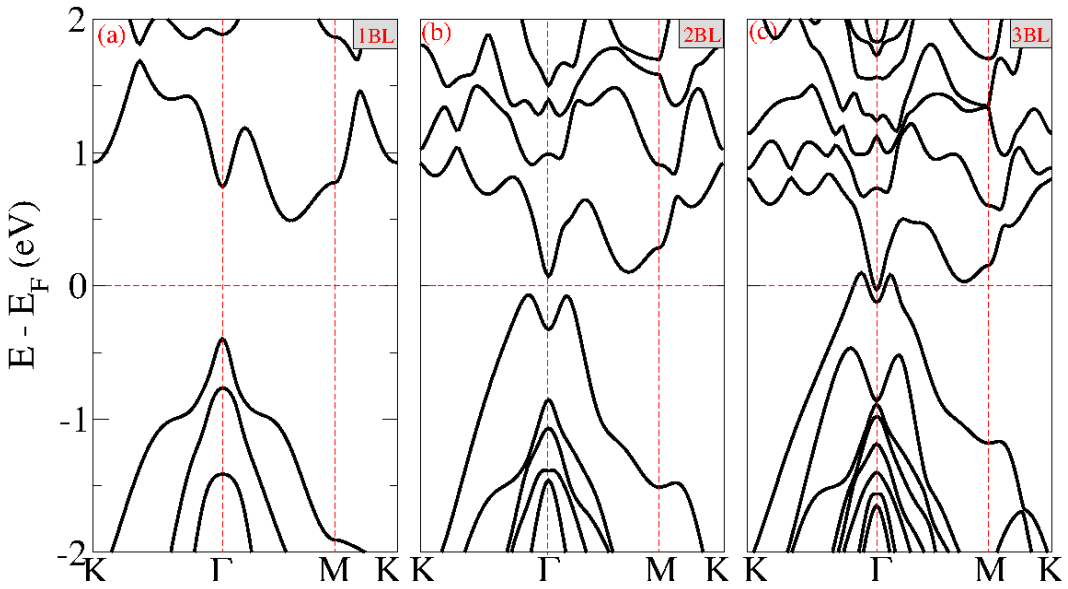

Figure 6.3: Band structure with one to three bilayer thickness. The Fermi level is set to zero.

energy [192, 193]. These metallic states, present a spin polarization locked with the momentum, which is protected by time reversal symmetry [192]. Such surface states are due to the bulk topological phase, which is characterized by a Z_2 invariant number [194, 195]. Sb(111) in thin film form could become, in principle, a 3D topological insulator if quantum confinement opened a gap in the bulk bands.

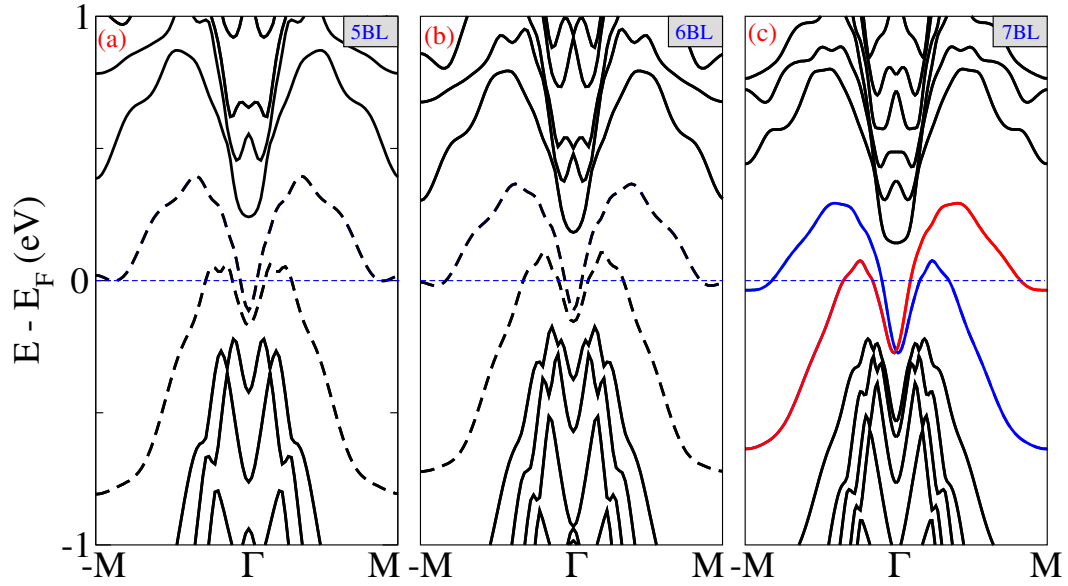

Figure 6.4: Band structure with five to seven bilayer thickness. The Fermi level is set to zero.

The topological features start to appear in the three BL case, where a non-trivial helical edge state below the Fermi level at Γ point can be identified (see Figure 6.3 (c)). This helical state consists of two surface states degenerated at Γ point but separated in energy elsewhere by SOC [193]. Nevertheless, it is noticeable that for the case of five BL and six BL films (see Figure 6.4(a) and (b)), the gaps are opened up again at Γ point. On the other hand, we have shown that the decoupling of the TSS requires a minimum of ~ 7 BL. The two surface bands in 7BL Sb are connected to the conduction band and the valence band separately. The resulting gapless configuration of the surface states (double degenerate) gives rise to a single Dirac cone, which is the signature of nontrivial topological order. The Dirac point is about 260 meV below the Fermi level, within the bulk band gap.

By the time that the TSS are decoupled and the gap at the Dirac point closes down, the Fermi energy crosses the Dirac cone above the Dirac point, but also crosses 6 surface state pockets and 6 bulk pockets. The presence of these bulk pockets could prevent the topological nature of the surface states from manifesting in conductivity measurements, although STM studies have shown that backscattering on the surface maintains traces of protection, even for semi-infinite crystals [196].

In next section, we examine the water effect on the electronic properties of 7BL Sb.

6.6 Effect of H_2O molecules on the 7BL Sb

How do H_2O molecules affect the electronic properties of antimonene? To address this issue, we investigated the behavior of three layers of H_2O on the surface of 7BL Sb. First, each molecule was placed in diverse configurations above various possible physisorption sites at a large distance from 7BL SB strucure (substrate). Then the atomic positions of the whole system were optimized to attain minimum total energy, as well as atomic forces. The optimized structures corresponding to minimum total energy are presented in Figure 6.5. Calculated values regarding the binding energy and molecule-substrate distances are E_b = 140 meV and d_{H_2O-Sb} = 2.77 Å. The optimized atomic configuration and calculated values related with energetics and physisorption configuration indicated that the molecule-substrate interaction is rather weak. The binding energy of H_2O (per unit cell) is 124 meV. As for the heights of molecules and the minimum distances between molecule and substrate Sb atom, they are rather large in compliance with low binding energies. Accordingly, the 7BL Sb is rather inert to the molecules H_2O, As reported in others theoretical [197] and experimental works [16]. In this respect, dissociation of these molecules cannot take place on 7BL Sb (as well as for others thickness [16, 197]) in normal conditions.

Now, we may turn our attention to the effect of H_2O on the topological properties of Sb on band structure, which will be illustrated in the following discussions based on the 7BL film. The surface bands in Figure 6.4(c) are doubly degenerate because of the two surfaces of the film, while

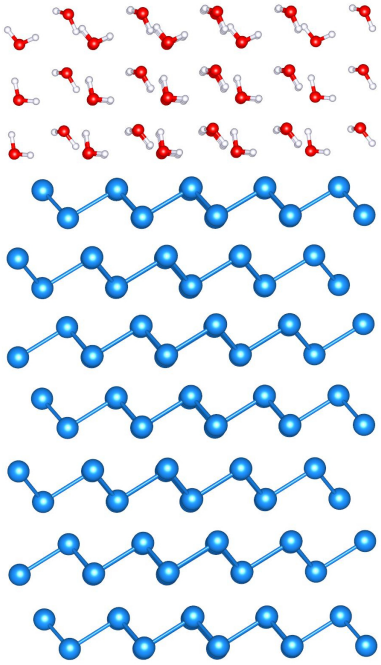

Figure 6.5: Relaxed structure of 7BL Sb with 3 layers of H_2O on the surface.

those in Figure 6.6 are nondegenerate.

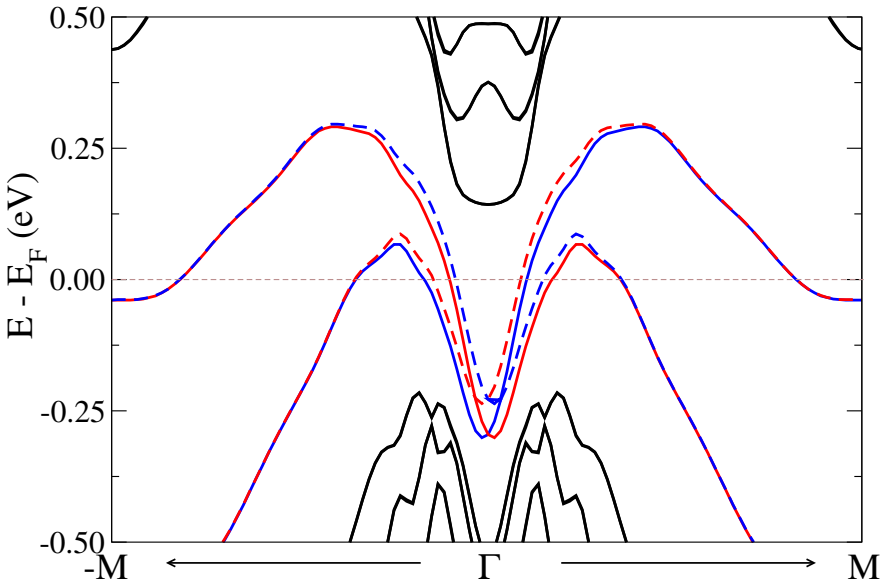

Figure 6.6: Band structure of 7BL antimonene. Solid (dashed) lines correspond to the layer in the top (bottom). Blue (red) correspond to spin down (up).

In Figure 6.6, the surface states on the upper surface of the film are shifted slightly upward

(dashed lines) in energy (~ 30 meV) by the perturbation caused by the presence of water molecules, resulting in two separate Dirac cones at the zone center. The Dirac cone of down surface (solid lines) are shifted slightly downward in energy (~ 30 meV). These shifts in energy are according to the position of the Dirac cone for the 7BL without H_2O.

6.7 Electrical characterization of few-layer antimonene

The results presented bellow are being currently carried out by the groups of Dr. Júlio Gómez Herrero and Dr. Félix Zamora. Preliminary results on the electrical characterization of few-layer antimonene are presented in this section. Since the size of the antimonene flakes were very small, Probe-Assisted Nanowire (PAN) lithography had been developed to create electrical contacts on different FL-Sb flakes. C-AFM was used to probe their electrical properties at room temperature. Figure 6.7 shows AFM topographic images of the studied flakes, whose thicknesses varied from ~ 3.5 to 21 nm.

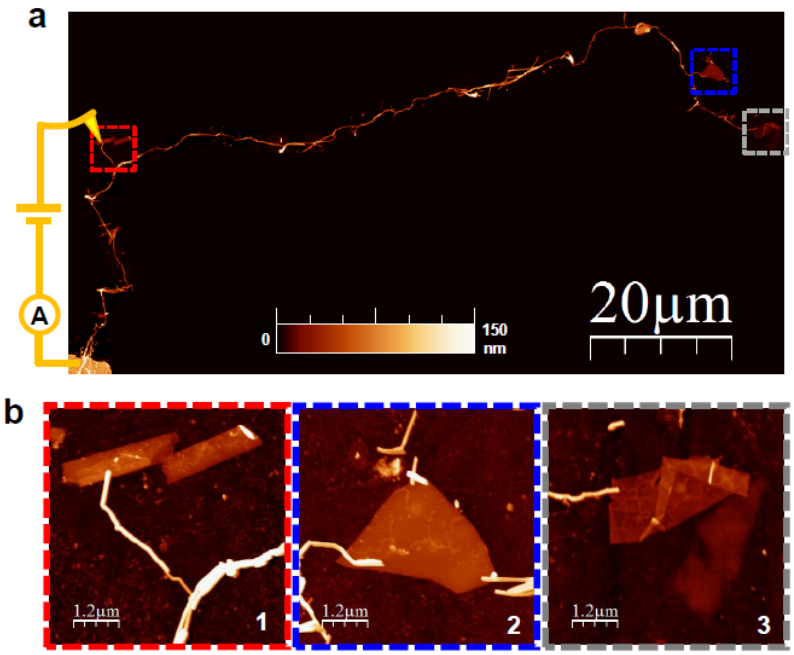

Figure 6.7: Setup for the electrical characterization of FL-Sb flakes. a) AFM topographic image of the whole area under study. This image is a collage of AFM images of smaller areas following the Au path, hence the absence of any feature far from it. A diagram of the electrical circuit for one of the flakes has been included for the sake of clarity. On the bottom left corner a micrometer size gold electrode created by thermal evaporation assisted by stencil mask can be seen. b) Details of the studied FL-Sb flakes. Flakes are designated with the numbers shown in the bottom right corners: 1, 2 and 3 from left to right.

C-AFM measurements were performed by using a metallized AFM tip as a second mobile

electrode to measure the current in the flakes as a function of their distance to the Au nanowire electrode. Images were acquired in AM-AFM mode and at selected locations the tip was brought into contact to perform IV characteristics. Figure 6.8 presents electrical characterization of the FL-Sb flakes in Figure 6.7.

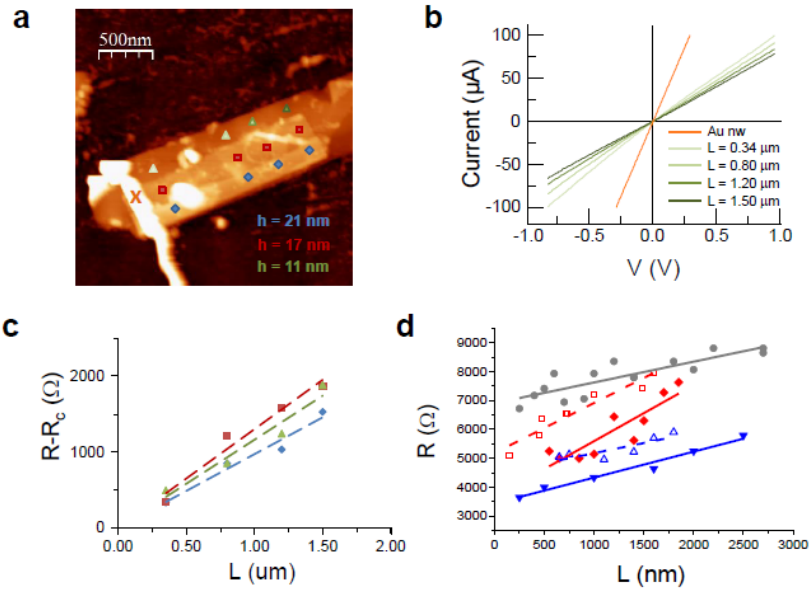

Figure 6.8: Electrical characterization of FL-Sb flakes. a) AFM topographic image of flake 1. Spots where IV curves at different tip-electrode distances are marked with different symbols. b) Representative IV curves at different tip-electrode distances for the lowest terrace in flake 1. c) Resistance vs. Length plots obtained from IV curves in the different terraces in flake 1 as pointed by the symbols in a). Dashed lines are linear fits for data from each terrace. No significant differences in the slopes are found within error (contact resistance was subtracted in this plot for clarity). d) Resistance vs. Length plots from similar IV curves as in b) obtained in the different flakes using different AFM tips. Red: flake 1, blue: flake 2, gray: flake 3. Symbols are experimental values and lines are linear fits to these experimental data. Solid symbols with solid fit lines correspond to data acquired with one tip whereas empty symbols with dashed fit lines correspond to data acquired with another tip.

Figure 6.8(a) shows an AFM topographic image of flake 1. The locations where IV curves were acquired are marked with different symbols. Figure 6.8(b) shows representative IV curves acquired in flake 1 at different tip-Au electrode distances. The linear dependence of the IV curves is in good agreement with our theoretical calculations for thicknesses above 3 layers, where no band gap is expected, and is another proof of the high stability of antimonene to ambient conditions. The linear shape of the curves is also indicative of good electrical contacts between both tip-sample and sample-Au electrode. Figure 6.8(c) presents the dependence of the resistance with the distance between electrodes for the spots marked with symbols in figure 6.7(a). Neither

significant differences among terraces nor correlation with the terrace height can be found. Figure 6.8(d) presents Resistance vs. Length curves for the three studied flakes using two different AFM tips. Linear fits allow extracting the 1D resistivity, $\rho_{1D} = dR/dL$, from the slopes and contact resistances, R_c, from the intersections for L = 0. As expected, it can be observed that, disregarding the contact resistance, the slope for each flake is independent of the tip.

On the other hand, the sheet resistivity can be defined as:

$$\rho_{2D} = \frac{\Delta R}{\Delta L} W \tag{6.1}$$

where ΔR is the contribution to the resistance of a portion of the flake in a length ΔL with a width W. Consequently, $\rho_{2D} = \rho_{1D} W$. Please notice that the unit of ρ_{2D} is Ω. It is usually employed Ω/□ to express the ρ_{2D} 2-dimensional character.

Since the dimensions of the flakes are very well characterized from the AFM images, the sheet resistivity, ρ_{2D} can be calculated from the ρ_{1D}, using equation 6.1. For conventional 2D materials, the sheet resistance depends on thickness. Interestingly, this tendency is not observed for the measured few-layer antimonene flakes. In this case, ρ_{2D} yields an average value of 1300 ± 400 Ω/□.

Our theoretical calculations, show that few-layer antimonene band structure presents topologically protected surface states that originate a bidimensional conductance character of the flakes, independent of their thicknesses. Figure 6.9 show the partial density of states (PDOS) of

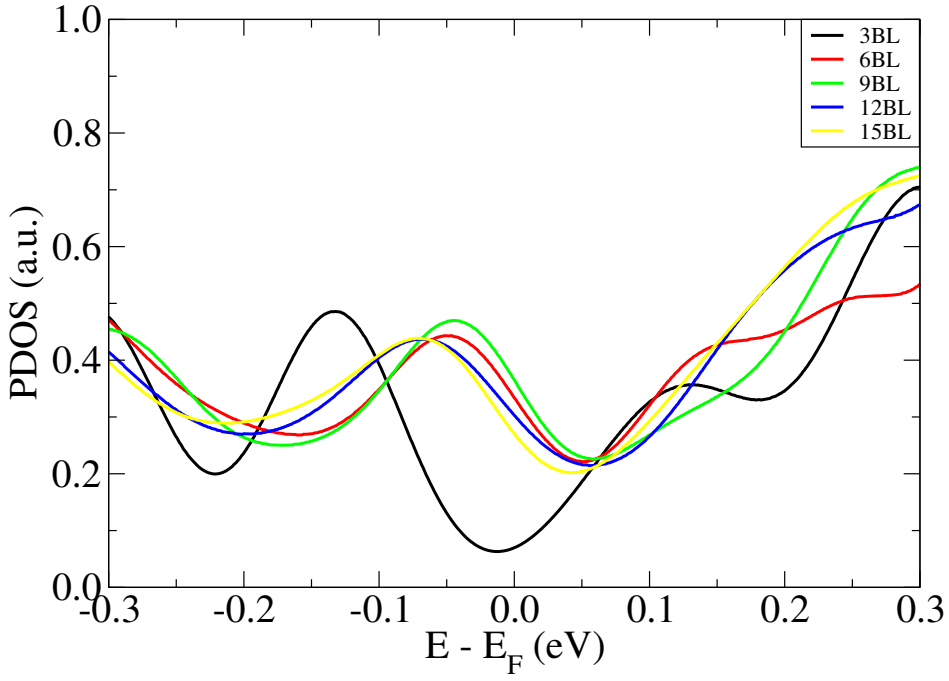

Figure 6.9: Partial density of states (PDOS) of 3 to 15BL Sb thickness.

the surface states considering the thickness of 3 to 15 BL. It can be observed that the density

of surface states remain constant with the increment of thickness (> 5BL), indicating that the conductivity due to topologically protected states does not change with the thickness, as the experiment suggest.

A direct comparison of the ρ_{2D} values obtained in similar conditions for graphene, ρ_{2D-G} = 670 Ω/□, and for FL-Sb now, $\rho_{2D-FLSb}$ = 1300 Ω/□, suggests a bidimensional electrical transport. From the band structures in figure 6.4(c), it can be seen that, since the two Dirac cones in FL-Sb are almost superimposed, backscattering between them is likely to occur, and then, assuming similar carrier concentrations in both graphene and FL-Sb, the resistivity in this latter case is expected to be comparable but larger than in graphene, as observed experimentally.

From the obtained ρ_{2D} value for FL-Sb, the mobility can be roughly estimated using the expression:

$$\mu = \frac{\sigma_{2D}}{e n_{2D}} \tag{6.2}$$

where μ is the mobility in $cm^2\ V^{-1}\ s^{-1}$, σ_{2D} the bidimensional conductivity in S, e the electron charge in C =V·S·s and n_{2D} the bidimensional carrier concentration in cm^{-2}. σ_{2D} can be obtained from ρ_{2D}, $\sigma_{2D} = 1/\rho_{2D}$ and n_{2D} can be calculated from the band structure, counting the number of carriers per unit area in the surface states, resulting in $n_{2D} \sim 6\ 10^{12}\ cm^{-2}$. This figure is in good agreement with a back-of-the-envelope calculation comparing this band structure to that of graphene. In the first Brillouin zone graphene presents 4 Dirac cones, whereas few-layer antimonene presents a central Dirac cone and 6 pockets. Therefore, assuming a similar Fermi level, in this case n_{2D} could be roughly estimated as 7/4 of the graphene carrier density, which coincides fairly well with the value from more sophisticated calculations. A high mobility $\mu \sim 800\ cm^2\ V^{-1}\ s^{-1}$ is obtained in good agreement with theoretical predictions [66, 67, 198]. This figure can be put in perspective by comparing it with the reported mobility of black phosphorus, $\mu_{BP} \sim 50$ - 1000 $cm^2\ V^{-1}\ s^{-1}$ (depending on the thickness) [139]. The high mobility obtained for antimonene turns it as a promising candidate for nanoelectronics and optoelectronics.

6.8 Conclusion

As mentioned at the beginning of this section, these are preliminary results and are still being carried out, but initial comparison between experimental results and theory seems to agree fairly well, pointing to a conduction governed by topologically protected surface states in few-layer antimonene. According to the calculated band structures for FL-Sb in vacuum and including water to somehow mimic ambient conditions, these surface states, which are given by the Dirac cones in the Γ point and the hole pockets nearby, are very robust and do not vanish in ambient conditions, pointing to topologically protected surface states. Thus, an essential role of these surface states is expected in the electrical conduction of few-layer antimonene flakes. In particular, was observed that these surface states originate the absence of thickness dependence on the electrical properties of FL-Sb flakes, as the experiment suggest.

CHAPTER 7

GENERAL CONCLUSIONS

In the present manuscript, I have been dedicated to theretical study the properties of promising novel semiconducting 2D materials which could be used as an alternative to the common bulk semiconductors in electronic and optoelectronic applications. Four different nanomaterials have been studied during this thesis: Molybdenum disulfide (MoS_2), Franckeite, Titanium trisulfide (TiS_3) and Few-layer Antimonene.

Heterostructures have been the essential elements in modern semiconductor industry and play a crucial role in high-speed electronics and optoelectronic devices. The quality of the electrical contacts - quantified through the contact resistance - is as important to the proper functioning of the entire device as the semiconductor (SC) itself.

Semiconductors of atomically thick monolayers, which can be combined to create van der Waals heterostructures where monolayers of multiple 2D materials are stacked vertically layer-by-layer, can also be stitched together seamlessly in-plane to form lateral heterojunctions. Lateral interfacing of atomic monolayers has opened up unprecedented opportunities to engineer two-dimensional heteromaterials. Yet, little is known about the nature of these newly created interfaces.

A theoretical study of the electrical contact between the two most common crystallographic phases of MoS_2 monolayer crystals: 2H (semiconductor) and 1T (metallic) was performed. In our work we exploit a combined strategy to study the behavior of these lateral heterostructures through DFT calculations, tight binding methodology, and quantum transport. Our tight-binding quantum transport calculations aided by the DFT results generically confirm a low contact resistance in the range of 200 - 400 $\Omega\mu m$, as experimentally reported. We show that, locally, the interface dipole potential changes the contact resistance that is predicted to be smaller at the armchair interface for electron injection and, on the contrary, smaller for hole injection at the

zigzag interface.

The assembly of the van der Waals heterostructures is typically done manually by artificial staking of individual layers thus presenting challenges and issues such as the control of the relative orientation between the stacked layers and avoiding interlayer contaminants. Moreover, large scale isolation methods as liquid phase exfoliations have problems to provide suspensions whith platelets consisting of van der Waals heterostructures with high quality.

Here we present an extensive theoretical and experimental characterizations of franckeite which is a naturally occurring and air stable van der Waals heterostructure. Thin layers of heterostructures based on alternating layers of SnS_2-based and PbS-based 2D layers (with remarkably high crystalline and stacking order) by mechanical and liquid phase exfoliation were isolated. As the bulk material is already composed of these alternating SnS_2 and PbS layers, the exfoliation process minimizes stacking missorientation and avoids interlayer adsorbates in the isolated nanosheets of franckeite.

These ultrathin van der Waals heterostructures have been thoroughly characterized by microscopy (SEM, TEM, AFM, STM), spectroscopy (Raman, UV-VIS-IR, syncrotron micro-XPS, STS) and electrical (we fabricated proof-of-concept devices: a photodetector and a PN junction) measurements. We also performed density functional calculations to study the band structure. We found that franckeite layers are highly stable in air and they show a p-type semiconducting behnaviour with a narrow hap of 0.5-0.7 eV. Thus, this material can be an interesting replacement for black phosphorus (the most studied narrow gap p-type 2D semiconductor so far) which tends to degradate rapidly in air.

TiS_3 is narrow-bandgap material which has been recently isolated as few-layer nanoribbons with high performance in electronic and optoelectronic devices, showing remarkable field-effect characteristics, high mobility and ultrahigh photoresponse to NIR light. It is a rather new quasi-1D material that has gained attention very fast within the scientific community due to its interesting physical properties and its promising applications. Nevertheless, little is known about the thermal mechanisms taking place in nanostructured field-effect devices based on TiS_3.

We investigate the electrical breakdown of TiS_3 nanoribbon-based field-effect transistors (FETs) and the thermal mechanisms that lead to the devices breakdown. For that purpose, we measure the maximum current density that TiS_3 nanoribbons are able to stand in FETs and obtain that it is amongst the highest current densities reported for nanostructured materials. We estimate the temperature reached in these devices using the 1D heat equation and find that the presence of defects or vacancies in the material might be responsible for their electrical breakdown. Furthermore, these results are compared with thermogravimetric analysis of bulk TiS_3 degradation, as well as with density functional theory and Kinetic Monte Carlo simulations of surface oxidation and the subsequent desorption of sulphur atoms that lead to the creation of defects and could explain the FETs malfunction.

Finally, preliminary results on the electronic and electrical properties of few-layer antimonene

have been presented. Few-layer (> 2 BL) antimonene shows metallic characteristic. In particular, few-layer (> 6 BL) presented the gapless configuration of the surface bands give rise to a single Dirac cone (double degenerate), which is the signature of nontrivial topological order. H_2O molecules on the surface broke the degeneracy of the Dirac cone giving rise to two Dirac cones at the Γ point separated by 60 meV. The experimental electrical properties reported herein are in good agreement with theoretical calculations still ongoing, pointing to a conduction governed by topologically protected surface states in few-layer antimonene.

CHAPTER 8

CONCLUSIONES GENERALES

En el presente manuscrito, se ha dedicado a estudiar las propiedades de los nuevos prometedores materiales semiconductores 2D que podrían ser utilizado como una alternativa a los semiconductores masivos comunes en aplicaciones electrónicas y optoelectrónicas. Durante esta tesis se han estudiado cuatro nanomateriales diferentes: Disulfuro de Molibdeno (MoS_2), Franckeíta, Trisulfuro de Titanio (TiS_3) y Antimoneno de pocas capas.

Las heteroestructuras han sido los elementos esenciales en la industria moderna de semiconductores y desempeñan un papel crucial en la electrónica de alta velocidad y los dispositivos optoelectrónicos. La calidad de los contactos eléctricos - cuantificados a través de la resistencia de contacto - es tan importante para el correcto funcionamiento de todo el dispositivo como el propio semiconductor (SC).

Los semiconductores de monocapas atómicamente gruesas, que se pueden combinar para crear heterostructuras de van der Waals donde las monocapas de múltiples materiales 2D se apilan verticalmente capa por capa, también pueden ser cosidas juntas de forma transparente en el plano para formar heterojunciones laterales. Interfaz lateral de Monocapas atómicas ha abierto oportunidades sin precedentes para diseñar heteromateriales bidimensionales. Sin embargo, poco se sabe sobre la naturaleza de estas interfaces recién creadas.

Se realizó un estudio teórico del contacto eléctrico entre las dos fases cristalográficas más comunes de los cristales monocapa de MoS_2: 2H (semiconductor) y 1T (metálico). En nuestro trabajo se explota una estrategia combinada para estudiar el comportamiento de estas heterostructuras laterales a través de cálculos DFT, del método tight binding y el transporte cuántico. Nuestros cálculos de transporte cuántico de unión apretada ayudados por los resultados de DFT confirman genéricamente una resistencia de contacto baja en el rango de 200 - 400 $\Omega\mu m$, en acuerdo con los resultados experimentales. Mostramos que, localmente, el potencial del dipolo interfacial

cambia la resistencia de contacto que se prevé que sea menor en la interfaz del armchair para la inyección de electrones y, por el contrario, menor para la inyección de agujeros en la interfaz zigzag.

El montaje de las heterostructuras de van der Waals se realiza típicamente manualmente mediante apilamiento artificial de capas individuales, presentando así desafíos y cuestiones tales como el control de la orientación relativa entre las capas apiladas y evitar contaminantes entre capas. Además, los métodos de aislamiento a gran escala, las exfoliaciones químicas o en fase líquida, tienen problemas para proporcionar suspensiones con plaquetas consistentes en heterostructuras de van der Waals de alta calidad.

Aquí fue presentado un enfoque radicalmente diferente para fabricar heterostructuras ultrafinas basadas en capas 2D: fueron aisladas capas finas de heteroestructuras basadas en capas alternas de capas 2D de SnS_2 y PbS (con un orden cristalino y estacionario notablemente alto) por exfoliación mecánica y líquida de la Franckeíta, un mineral natural. Como el material a granel ya está compuesto por estas capas alternas de SnS_2 y PbS, el proceso de exfoliación minimiza la desorientación de apilamiento y evita adsorbatos de intercapa en las nanocintas aisladas de la Franckeíta.

Estas heterostructuras de van der Waals ultradelgadas han sido caracterizadas por microscopía (SEM, TEM, AFM, STM), espectroscopía (Raman, UV-VIS-IR, sincrotrón micro-XPS, STS) y eléctrica (fueron fabricados dispositivos de prueba de concepto: Un fotodetector y una unión PN). También se realizaron cálculos de DFT para estudiar la estructura de la bandas. Encontramos que capas de Franckeíta son muy estables en el aire y que muestran un semiconductor tipo-p con un gap estrecho de (0,5-0,7 eV). Así, este material puede ser un sustituto interesante para el fósforo negro (el semiconductor 2D tipo-p de gap estrecho más estudiado hasta el momento) que tiende a degradarse rápidamente en el aire.

El Trisulfuro de Titanio (TiS_3) es un material de banda estrecha que ha sido aislado recientemente como nanocintas de escasa capa con alto rendimiento en dispositivos electrónicos y optoelectrónicos, mostrando notables características de efecto de campo, alta movilidad y alta respuesta fotovoltaica a la luz NIR. Es un material cuasi-1D bastante nuevo que ha ganado mucha atención en la comunidad científica debido a sus interesantes propiedades físicas y sus prometedoras aplicaciones. Sin embargo, poco se sabe sobre los mecanismos térmicos que tienen lugar en las nanoestructuras de dispositivos de efecto de campo basados en TiS_3.

Se investigó la descomposición eléctrica de los transistores de efecto de campo basados en nanocintas y los mecanismos térmicos que conducen a ruptura de los dispositivos. Para ello, medimos la densidad de corriente máxima que los FETs basados en nanocintas de TiS_3 son capaces de soportar y obtenemos que está entre las densidades de corriente más altas reportadas para materiales nanoestructurados. Estimamos la temperatura alcanzada en estos dispositivos usando la ecuación de calor 1D y encontramos que la presencia de defectos o vacantes en el material podría ser responsable de su avería eléctrica. Además, estos resultados se comparan

con el análisis termogravimétrico de la degradación de la masa, así como con las simulaciones de DFT y Monte Carlo cinético de la oxidación superficial y la posterior desorción de los átomos de azufre que conducen a la creación de defectos y podría explicar el funcionamiento defectuoso de los FETs.

Por último, se han presentado resultados preliminares sobre las propiedades electrónicas y eléctricas del antimoneno de pocas capas. Antimoneno de pocas capas (> 2 BL) tiene una característica metálica. En particular, el caso (> 6 BL) presentó la configuración sin ranuras de las bandas de superficie dando lugar a un solo cono de Dirac (Doble degenerado), que es la firma del orden topológico no trivial. La presencia de moléculas de H_2O en la superficie rompió la degeneración en el cono de Dirac dando lugar a dos conos Dirac en el punto Γ separados por 60 meV. Las propiedades eléctricas experimentales presentadas hasta ahora están en buen acuerdo con los cálculos teóricos aún en curso, apuntando a una conducción regida por estados de superficie topológicamente protegidos en el antimonio de pocas capas.

APPENDIX A

APPENDIX A

A.1 Density Functional Theory (DFT)

The full Hamiltonian for a set of electrons and atoms in a solid is

$$\hat{H} = -\sum_{I=1}^{P}\frac{\hbar^2}{2M_I}\nabla_I^2 - \sum_{i}^{N}\frac{\hbar^2}{2m}\nabla_i^2 + \frac{e^2}{2}\sum_{I=1}^{P}\sum_{J\neq I}^{P}\frac{Z_I Z_J}{|\,\mathbf{R}_I-\mathbf{R}_J\,|} + \frac{e^2}{2}\sum_{i=1}^{N}\sum_{i\neq j}^{N}\frac{1}{|\,\mathbf{r}_i-\mathbf{r}_j\,|} - e^2\sum_{i=1}^{N}\sum_{I=1}^{P}\frac{Z_I}{|\,\mathbf{R}_I-\mathbf{r}_i\,|} \tag{A.1}$$

where the atomic nuclei is represented by capital letters indexes and the electrons by lowercase letters. The first two terms are the operators kinetic energy for the nuclei and electrons, $\hat{T}_N$ and $\hat{T}_e$. The third and fourth terms are the Coulomb interaction between the same type of charge. Finally, the last term is the Coulomb interaction among the electrons and the nuclei. Thus the many-body Schrödinger equation reads

$$\hat{H}\Psi_n(\mathbf{R}_I,\mathbf{r}_i) = E_n\Psi_n(\mathbf{R}_I,\mathbf{r}_i) \tag{A.2}$$

where $\Psi_n(\mathbf{R}_I,\mathbf{r}_i)$ is the many-body wave function and E_n the corresponding eigenvalue. As the inverse masses of nuclei are very small it is common to first assume the kinetic energy of atoms to be zero while solving the equation for electronic degrees of freedom. Then later the nuclei degrees of freedom are treated classically. This separation of electronic and nuclear motion is known as the Born-Oppenheimer approximation[199]. Thus, in this approximation it is possible to separate the variables

$$\hat{H}\Psi_n(\mathbf{R}_I,\mathbf{r}_i) = \sum_n \chi_n(\mathbf{R}_I,t)\psi(\mathbf{R}_I;\mathbf{r}_i) \tag{A.3}$$

where $\chi_n(\mathbf{R}_I,t)$ are the wave functions describing the nuclei, and $\psi(\mathbf{r}_i;\{\mathbf{R}_I\})$ are the eigenstates of the time independet Schrödinger equation for the electron

$$\hat{H}_e\psi(\mathbf{r}_i;\{\mathbf{R}_I\}) = \epsilon_n\psi(\mathbf{r}_i;\{\mathbf{R}_I\}) \tag{A.4}$$

In this equation, the position of the nuclei are considered as parameters that can change with the time. Then, the electronic Hamiltonian is

$$\hat{H}_e = -\sum_i^N \frac{\hbar^2}{2m}\nabla_i^2 + \frac{e^2}{2}\sum_{i=1}^N\sum_{i\neq j}^N \frac{1}{|\,\mathbf{r}_i - \mathbf{r}_j\,|} - e^2\sum_{i=1}^N\sum_{I=1}^P \frac{Z_I}{|\,\mathbf{R}_I - \mathbf{r}_i\,|} \tag{A.5}$$

Therefore, with this approximation we can find the electronic contribuition, ϵ_n, to the total energy of system. This electronic energy is orders of magnitude bigger than any other energy contribuition given by the nuclei. Eq. (A.1) contains thus the particles' motions which are correlated through the potential energy.

A.1.1 The Hohenberg-Kohn theorems

Density functional theory (DFT) is based on the two theorems by Hohenberg and Kohn (H-K) [70]. Basicaly, the first theorem shows that there is a one-to-one correspondence between the electron density and the external potential. The energy functional $E[\rho(r)]$ is defined as

$$E[\rho(\mathbf{r})] \equiv E_{ext}[\rho(\mathbf{r})] + E_{Hartree}[\rho(\mathbf{r})] + G[\rho(\mathbf{r})], \tag{A.6}$$

where,

- the first term is the energy $E_{ext}\rho(\mathbf{r})$ due to external potential $v_{ext}(\mathbf{r})$, given by $E_{ext}[\rho] \equiv \int v(\mathbf{r})\rho(\mathbf{r})\mathrm{d}\mathbf{r}$;
- the second term is the Coulomb energy (Hartree term) $E_{Hartree}[\rho] = \frac{1}{2}\iint \frac{\rho(\mathbf{r})\rho(\mathbf{r}')}{|\mathbf{r}-\mathbf{r}'|}\mathrm{d}\mathbf{r}\mathrm{d}\mathbf{r}'$
- the last term $G[\rho(\mathbf{r})]$ is a functional of $\rho(\mathbf{r})$ including the kinetic energy term of the non-interacting system $T[\rho(\mathbf{r})]$ and $E_{xc}[\rho(\mathbf{r})]$ is exchange-correlation energy functional.

The second theorem states that, from variational principle, the energy of the ground state is the global minimum of the functional energy $E[\rho(r)]$ and density that minimizes this functional is the exact density of state fundamental $\rho_0(r)$. That is, assuming $\rho(\mathbf{r}) \geq 0$ we can write

$$\int \rho(\mathbf{r})\mathrm{d}\mathbf{r} = N \tag{A.7}$$

and

$$E[\rho(\mathbf{r})] \geq E[\rho_0(\mathbf{r})] = E_0. \tag{A.8}$$

The second theorem shows that for any attempt density $\rho(\mathbf{r}) \neq \rho_0(\mathbf{r})$, the total energy obtained is always greater than the total energy corresponding to the exact density of the ground state.

The H-K theorems lays the groundwork for reducing the many-body problem of N electrons with 3N spatial coordinates to 3 spatial coordinates, through the use of functionals of the electron density. Although the H-K theorems ensure that the knowledge of $\rho_0(r)$ is enough to determine all the properties of the ground state of the system, they do not provide a practical procedure to obtain it. This was only resolved from the Kohn-Sham equations.

A.1.2 The Kohn-Sham density-functional

In the Kohn-Sham formulation of DFT (KS-DFT) [200], the many-electron problem is mapped into an auxiliary single-particle problem

$$\left[-\frac{1}{2}\nabla^2 + v_{ext}(\mathbf{r}) + \int \frac{\rho(\mathbf{r})}{|\mathbf{r}-\mathbf{r}'|}\mathrm{d}\mathbf{r}' + v_{xc}^{\sigma}(\mathbf{r})\right]\phi_i^{\sigma} = \epsilon_i \phi_i^{\sigma} \qquad \text{and} \qquad i = 1,2,3,\cdots,N. \tag{A.9}$$

where $v_{ext}(\mathbf{r})$ is the external potential and

$$v_{xc}^{\sigma} = \frac{\delta E_{xc}[\rho_\alpha, \rho_\beta]}{\delta \rho_\sigma(\mathbf{r})} \tag{A.10}$$

is the exchange-correlation (XC) potential related to the exchange-correlation energy $E_{xc}[\alpha,\beta]$, where $[\sigma \equiv (\alpha,\beta)]$ represents the *spin* component. The total density is expressed using the KS orbitals as

$$\rho_\sigma(\mathbf{r}) = \sum_{i=1}^{N} f_i^{\sigma} \mid \phi_i^{\sigma}(\mathbf{r}) \mid^2, \tag{A.11}$$

where f_i^{σ} are the occupations, such that $f_i^{\sigma} = 0,1$ or $f_i^{\sigma} \in [0,1]$ if broadening is allowed. The auxiliary problem, Eq. A.9 and A.11, is solved self-consistently, since the potentials depend on the previous solution. The total energy can be written as a functional of the density

$$E[\rho_\alpha,\rho_\beta] = \sum_{\sigma}\sum_{i}^{N} f_i^{\sigma}\epsilon_i^{\sigma} - \frac{1}{2}\iint \frac{\rho(\mathbf{r})\rho(\mathbf{r}')}{|\mathbf{r}-\mathbf{r}'|}\mathrm{d}\mathbf{r}\mathrm{d}\mathbf{r}' + E_{xc}[\rho_\alpha,\rho_\beta] - \sum_{\sigma}\int v_{xc}^{\sigma}\rho_\sigma(\mathbf{r})\mathrm{d}\mathbf{r}, \tag{A.12}$$

where the single particle exchange-correlation potential energy $v_{xc}^{\sigma}(\mathbf{r})$ is subtracted and replaced with the exchange-correlation energy functional $E_{xc}[\rho_\alpha,\rho_\beta]$. Moreover, half of the Hartree potential is subtracted to omit double counting. Since kinetic energy functionals of density are typically not accurate enough, the Kohn-Sham formalism is used to work around this problem.

A.1.3 Exchange-correlation functionals

The exchange-correlation potential is crucial in the accuracy of DFT calculations and has been employed numerous computational studies in finding accurate forms of v_{xc}^{σ}. The simplest approximation is to assume that the density can be treated locally as an uniform electron gas; the exchange correlation energy at each point in the system is the same as that of an uniform electron gas of the same density (see Fig. **??**). This approximation was originally introduced by Kohn and Sham [70] and holds for a slowly varying density. Using this approximation the exchange-correlation energy for a density $\rho(\mathbf{r}) = \rho_\alpha(\mathbf{r}) + \rho_\beta(\mathbf{r})$ is given by

$$E_{xc}^{LDA}[\rho(\mathbf{r})] = \int \rho(\mathbf{r})\epsilon_{xc}^{LDA}[\rho(\mathbf{r})]\mathrm{d}\mathbf{r}, \tag{A.13}$$

where $\epsilon_{xc}(\rho)$ is the exchange-correlation energy per particle of an uniform electron gas of density ρ. The exchange-correlation potential is then given by

$$v_{xc}^{LDA}[\rho(\mathbf{r})] = \frac{\delta E_{xc}^{LDA}}{\delta\rho(\mathbf{r})} = \epsilon_{xc}(\rho) + \rho(\mathbf{r})\frac{\partial\epsilon_{xc}(\rho)}{\partial\rho}. \tag{A.14}$$

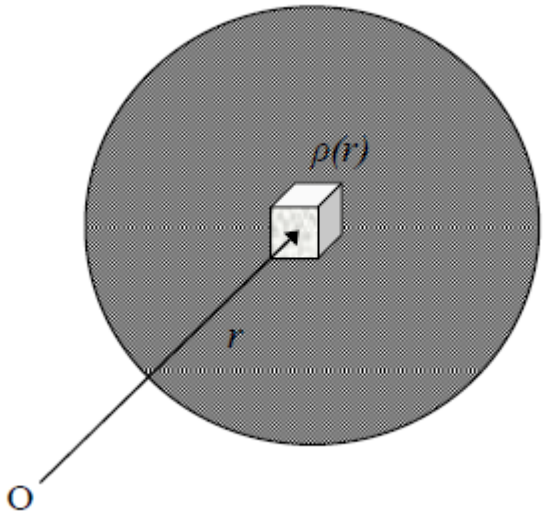

Figure A.1: The values ρ is calculated at each point of $\mathbf{r}$ [201].

For practical use of the LDA in calculations it is necessary to determine the exchange-correlation energy for an uniform electron gas of a given density. It is common to split $\epsilon_{xc}(\rho)$ into exchange and correlation potentials

$$E_{xc}^{LDA}[\rho(\mathbf{r})] = E_{x}^{LDA}[\rho(\mathbf{r})] + E_{c}^{LDA}[\rho(\mathbf{r})] \tag{A.15}$$

where $E_{x}^{LDA}[\rho(\mathbf{r})]$ is exchange potential and $E_{c}^{LDA}[\rho(\mathbf{r})]$ is the correlation potential. The exchange potential is given by the Dirac functional [202]

$$\epsilon_{x}[\rho(\mathbf{r})] = -\frac{3}{4}\left(\frac{3}{\pi}\right)^{\frac{1}{3}}\rho(\mathbf{r}). \tag{A.16}$$

Accurate values for $\epsilon_{c}(\rho)$ have been determined from Quantum Monte Carlo (QMC) calculations [203].

As the LDA approximates the energy of the true density by the energy of a local constant density, it fails in situations where the density undergoes rapid changes such as in molecules. An improvement to this can be made by considering the gradient of the electron density $\nabla\rho$, the so-called Generalized Gradient Approximation (GGA) [204]. The functional can be written as

$$E_{xc}[\rho] = E_{xc}^{GGA}[\rho(\mathbf{r})] = \int \rho(\mathbf{r})\epsilon_{x}\rho(\mathbf{r})F_{xc}(\rho(\mathbf{r}),\nabla\rho(\mathbf{r}))\mathrm{d}\mathbf{r}, \tag{A.17}$$

where: $F_{xc}(\rho(\mathbf{r}),\nabla\rho(\mathbf{r}))$ is the correction factor of local *exchange*.

Total energy and charge density of a system can in principle be evaluated accurately using DFT given an accurate exchange-correlation functional. However, even if the KS eigenenergies are commonly used to estimate the band structure, there is only little theoretical foundation

relating the two. Similarly, band gaps are estimated within the KS formalism by evaluating the difference between the highest occupied and lowest unoccupied KS eigenvalues (HOMO-LUMO energy gap). It is well-known that KS-DFT with PBE or local-density approximation (LDA) functionals typically underestimates the true band gaps [205].

A.1.4 HSE Hybrid functional

Despite the great success of relatively simple XC functionals such as LDA and GGA functionals, numerous computational studies suggest that KS-DFT calculations with hybrid functionals [150, 151, 206, 207] can provide systematically improved description of important physical quantities such as band gaps. In general, calculations using hybrid functional are computationally more expensive since it contains a part of the Fock exchange term, which is defined using the entire density matrix rather than the electron density.

The Heyd-Scuseria-Ernzerhof (HSE) hybrid functional [150, 151] originated as an alternative approach that can be efficiently applied in a vast range of systems. HSE employs screened short-range Hartree-Fock exchange instead of the full exact exchange, drastically reducing the computational requirements and, at the same time, overcoming the known problems of Hartree-Fock exchange where HF calculations in metals suffer from a divergence in the derivative of the orbital energies with respect to k [208]. This singularity is caused by the divergence of the Fourier transform $4\pi/k^2$ of the $\frac{1}{r}$ Coulomb potential which diverges for $k = 0$. The expression for the HSE exchange-correlation energy is

$$E_{xc}^{HSE} = aE_x^{HF,SR} + (1-a)E_x^{PBE,SR} + E_x^{PBE,LR} + E_c^{PBE}, \tag{A.18}$$

where $E_x^{HF,SR}$ is the Hartree-Fock exchange, $E_x^{PBE,SR}$ and $E_x^{PBE,LR}$ are the short-range and long-range components of the Perdew-Burke-Ernzerhof [116] (PBE) exchange functional, respectively, and $a = 1/4$ is the Hartree-Fock exchange mixing parameter [150, 151]. In HSE, the short-range and long-range partition in Eq. (A.18) is carried out splitting the Coulomb operator as

$$\frac{1}{r} = \frac{erfc(\omega r)}{r^{SR}} + \frac{erf(\omega r)}{r^{LR}}, \tag{A.19}$$

where erf and $erfc$ are the error and complementary error functions, respectively, and ω is the screening parameter. The functional form of HSE is based on the PBE0 [209, 210]. The HSE form can be viewed as an adiabatic connection functional only for the short-range portion of exchange, whereas long-range exchange and correlation are treated at the PBE GGA level.

In contrast to the LDA/GGA methods, the Hartree-Fock (HF) method correctly produces a charge transfer semiconductor by correctly identifying the top of the valence band. The HF method, however, significantly over-predicts the magnitude of the band gap. Hybrid functionals, which contain a fractional amount of exact HF exchange, are capable of arriving close to the experimental band gap.

APPENDIX B

APPENDIX B

B.1 Thermopower

We have also studied the thermopower of bulk franckeite by using a modified scanning tunneling microscope (STM) which allows to locally measure the therm-power of a surface. The gold STM tip, which is mechanically cut, is moved towards the sample for 70-90 nm to form a large contact.

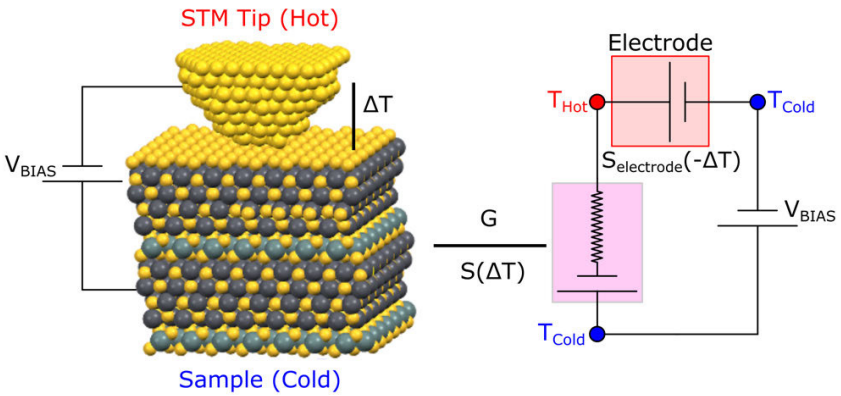

Figure B.1: Equivalent thermal circuit of the setup for measuring the thermopower. The sample is kept at ambient temperature T_{Cold} while the tip is heated to a temperature of $T_{Hot} = T_{Cold} + \Delta \cdot S$ is the thermopower of franckeite and Slead is the thermopower of the tip connecting lead. V_{BIAS} is the bias voltage applied at the sample.

The sample is kept at room tem-perature while the tip is resistively heated up to a temperature gradient of ~ 35 K. In addition to the applied bias voltage, the temperature gradient gives rise to a voltage offset $-S \cdot \Delta T$, where S is the thermopower of the franckeite (Figure B.1). This offset

can be measured from a current-voltage curve by finding the voltage that makes the current zero. The slope of the current-voltage curve gives the conductance (Figure B.2(a)) [211, 212].

By heating the tip we not only establish a temperature difference between the tip and the substrate but also a temperature gradient across the tip-connecting electrode, which gives rise to an additional thermoelectric voltage. The equivalent circuit for measuring the thermopower is shown in Figure B.1. Considering the equivalent circuit, we can write $I = G(V_{bias} + S_{electrode}\Delta T - S\Delta T)$, where S and $S_{electrode}$ are the thermopower of franckeite and the tip-connecting electrode, respectively, and $\Delta T = T_{Hot} - T_{Cold}$ is the temperature gradient, with T_{Hot} and T_{Cold} being the temperatures of the tip and the franckeite, respectively. It has been shown previously that $S_{electrode} = 0.05\mu V \cdot K^{-1}$, which is negligible in comparison with the thermopower of franckeite.

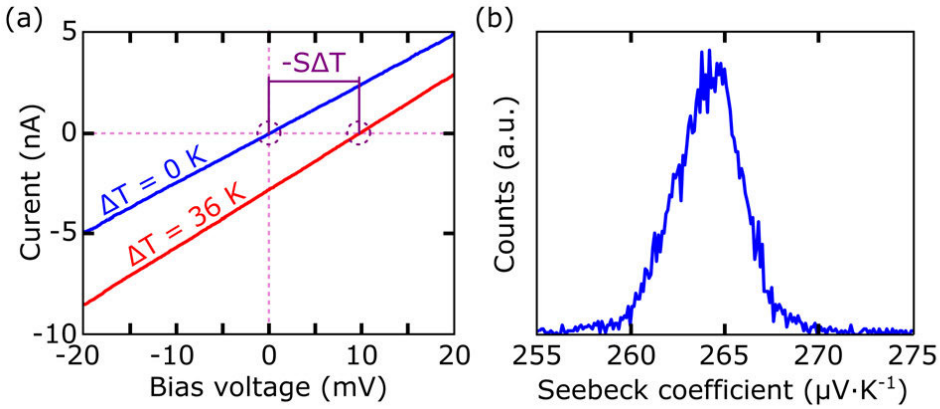

Figure B.2: Equivalent thermal circuit of the setup for measuring the thermopower. The sample is kept at ambient temperature T_{Cold} while the tip is heated to a temperature of $T_{Hot} = T_{Cold} + \Delta \cdot S$ is the thermopower of franckeite and Slead is the thermopower of the tip connecting lead. V_{BIAS} is the bias voltage applied at the sample.

In addition, the resulting value of the measured thermopower is the difference between the thermopower of gold and franckeite, but since the thermopower of gold is much smaller than the franckeite, its contribution is negligible. To obtain the average thermopower of franckeite we collected data of 85 traces in a histogram (Figure B.2(b)) and we found a positive value of $S = 264\mu V \cdot K^{-1}$, allowing to state that the material is p-doped, since the sign of the thermoelectric current is dictated by the sign of the Seebeck coefficient (positive for p-doping, negative for n-doping) and the thermal gradient [213]. In addition, the mean conductance was found to be $G = 0.0032G_0(R = 4M\Omega)$, where G_0 is the quantum of conductance. The thermal conductivity of gold is expected to be much larger than that of franckeite when making a large contact, thus most of the temperature drops in the franckeite itself and consequently the thermopower measured is the bulk thermopower of the franckeite [211].

B.2 Raman spectroscopy

The Raman characterization was performed on bulk franckeite powder and on the most concentrated colloidal suspension (from the 100 mg·mL^{-1} NMP powder dispersion). Both samples present similar spectra, with five main bands centered at 66, 145, 194, 253, 318 cm^{-1}, and a shoulder from ~ 400 to 650 cm^{-1} (Figure B.3), confirming the nature of the colloid obtained. As in a first approximation, franckeite alternates SnS_2 and PbS layers having a crystal structure similar to that of SnS_2 and PbS, most of its Raman bands can be associated to those of the parent structures. However, the band at 253 cm^{-1} would result from the combination of phonon modes of both the Q and H layers [214]. We also find differences in the relative intensities between the Raman spectra of bulk and exfoliated material, probably originating from their respective thickness.

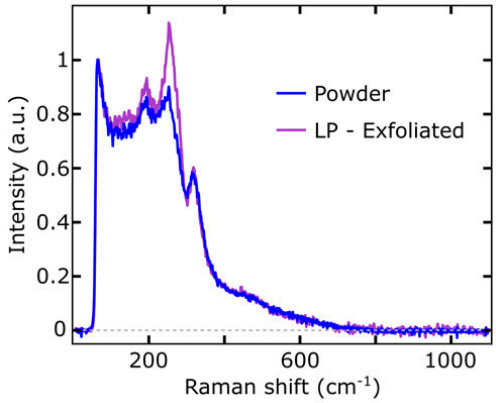

Figure B.3: Raman spectra of franckeite raw powder (blue line) and liquid-phase (LP)-exfoliated franckeite obtained from the sonication of a 100 mg·mL^{-1} powder dispersion in NMP (pink line).

The band at 66 cm^{-1} corresponds to an acoustic phonon mode in PbS [214–216], whereas the band at 318 cm^{-1} is a clear signa-ture of the A1g mode in SnS_2 [217–220]. Other bands at 145, 194 cm^{-1}, and the 400-650 cm^{-1} shoulder are most likely due to a superposition of respective phonon modes of both PbS (combinations and overtones of acoustic and optical modes) [214–216, 221] and SnS_2 (including the Eg mode and second-order effects) [217–220]. As proposed in other works on misfit compounds [214], the last band at 253 cm^{-1} could result from the combination of phonon modes of both layer types. Slight shifts are to be noted regarding the parent structures; they can be attributed to deviations in terms of structure [141, 145, 148] and composition (e.g. Sb and Fe identified by TEM/EDX) [222] between the idealized model and natural franckeite. In spite of its weakness, the interlayer van der Waals interaction can also cause some noticeable changes in the respective vibration properties of each lattice [214].

B.3 Liquid phase exfoliation

Liquid-phase exfoliation (LPE) of layered materials allows scale-up, improves processibility, and opens the way to chemically functionalize the nanosheets in suspension [65]. We demonstrate LPE isolation of franckeite by bath ultrasonication for 1 h at 20 °C, using franckeite powder obtained from careful grinding of mineral pieces (Fig. B.4). The LPE of franckeite were done by our collaborators Dr. Emilio M. Pérez's group (IMDEA Nanociencia, Madrid, Spain).

Figure B.4: Franckeite samples. Left: bulk mineral; middle: powder material obtained after grinding of raw chips; right: suspension of exfoliated material prepared by sonication of a 100 mg·mL^{-1} powder dispersion in NMP.

First, LPE was carried out in N-methyl-2-pyrrolidone (NMP), already used to exfoliate graphite and transition metal dichalcogenides [223, 224] due to its surface tension and coordination properties, which favour layer separation and subsequent nanosheet stabilization. LPE was also investigated in various isopropanol/water (IPA/water) mixtures, as well as in two other polar solvents, methanol and N,N-dimethylformamide (DMF). In the following, we will focus on NMP and IPA/water 1/4 (v/v), the latter matching surface tension with SnS_2 (ref. [225]).

Remarkably, all the suspensions prepared in NMP were indefinitely stable in time (46 months). Analysis of the most concentrated colloids using atomic force microscopy (AFM, Fig. B.5(a) and (b)) and TEM (Fig. B.5(c) and (d)) reveals large flakes (> 100nm in lateral size) of height < 25 nm, together with copious amounts of very small fragments (> 10 nm-20nm in lateral size), less present when exfoliating a less concentrated dispersion.

The LPE exfoliation in IPA/water leads to much more uniform nanosheets. Figure B.6(a) shows a large area AFM topographic image obtained after drop-cast-ing and drying of a franckeite dispersion prepared in IPA/water on a mica sub-strate. Statistical analysis of the height data (Figure B.6(b)) attests to the formation of very thin flakes, with a narrow thickness distribution

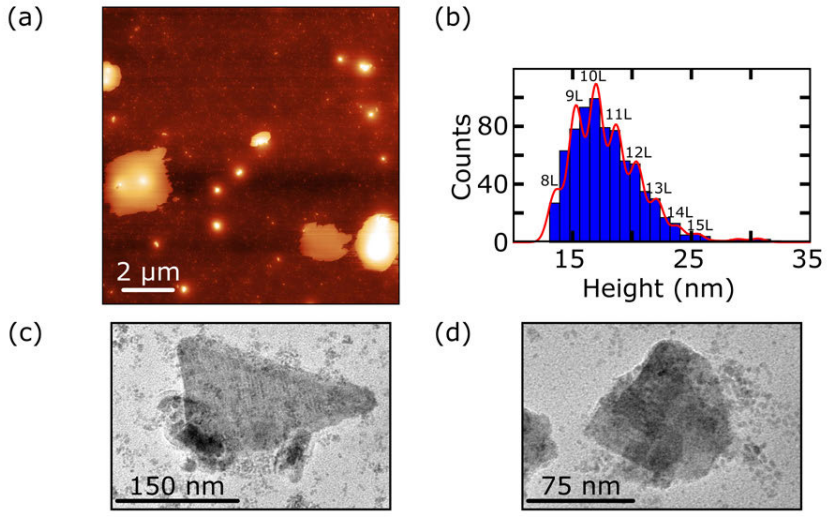

Figure B.5: (a) AFM micrograph of the sample drop-casted and dried over a freshly exfoliated mica substrate. (b) Statistical analysis of the raw height data. (c) and (d) TEM images of representative franckeite nanosheets prepared by exfoliation of a 100 mg·mL^{-1} powder dispersion in NMP

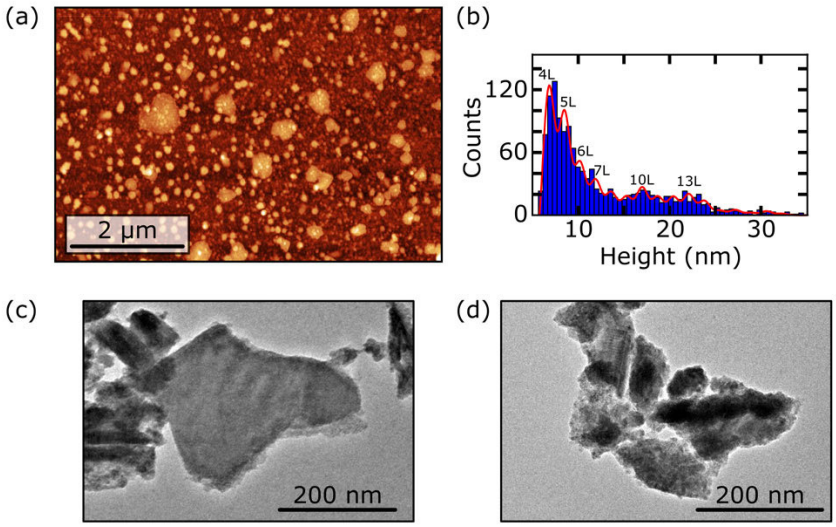

Figure B.6: (a) AFM topographic characterization of franckeite nanosheets obtained from the exfoliation of a 1 mg·mL^{-1} powder dispersion in isopropanol/water 1/4 (v/v). (b) Statistical analysis of the AFM raw height data. The inserted numbers indicate the corresponding number of layers (unit cell, H + Q layer, 1.7 nm in thickness) from 4 layers (4L) up to ~ 13 layers (13L). (c) and (d) TEM images of of franckeite nanosheets obtained from the exfoliation of a 1 mg·mL^{-1} powder dispersion in isopropanol/water 1/4 (v/v).

between 6 and 12 nm. This range corresponds to a maximum number of ~ 4 to 7 franckeite layers (being one layer an H and Q pair), without taking into account adsorbed solvent molecules remaining onto the nanosheet surface, which might increase the measured thick-ness by up to 1.2-1.3 nm [226]. The lateral size distribution (Figure B.6(c) and (d)), is also more homogeneous and displaced towards larger sheets (c.a. 200 nm).

B.4 Franckeite-based nanodevices

To further explore the electronic properties of franckeite, we have employed mechanically exfoliated flakes in the fabrication of electronic devices by transferring the flakes onto Ti/Au electrodes pre-patterned on a SiO_2/Si substrate. The flakes are placed bridging the electrodes using the deterministic transfer technique. Figure B.7 shows both optical microscopy and AFM topographic images of one of these devices (with a thickness ranging from ~ 7 nm to ~ 13 nm). In Appendix C we show the characterization of another franckeite photodetector.

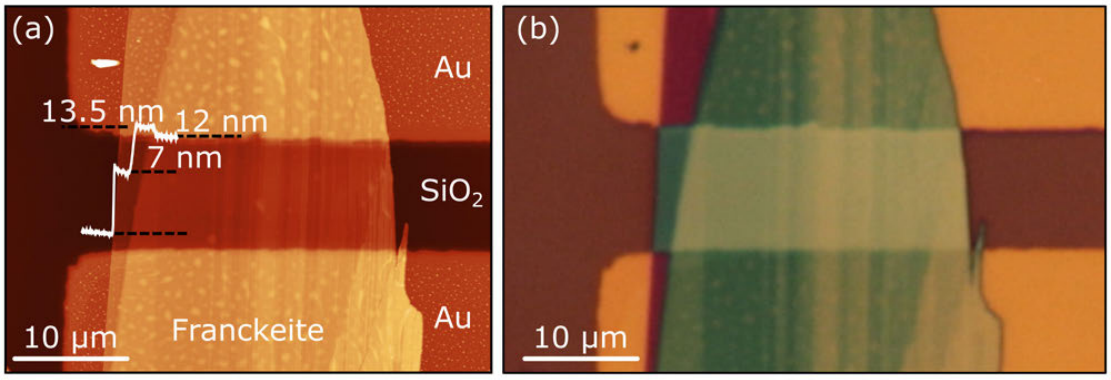

Figure B.7: (a) AFM topographic image of a franckeite-based device. The scan profile yields a thickness ranging from 7 nm to 13.5 nm. (b) Optical microscopy image of the device shown in (a).

B.4.1 Electronic characterization

The devices are characterized by measuring current-voltage characteristics (the current passing through the material (Ids) while sweeping the drain-source voltage (V_{ds}) with a fixed back-gate voltage (V_g)) and by measuring the current dependence on the back-gate voltage with a fixed drain-source voltage (transfer curve). Figure B.8 shows the $I_{ds} - V_g$ curve for the device shown in Figure B.7 measured in dark conditions, high vacuum (P < 10^{-5} mbar) and with an applied V_{ds} = 150 mV. The dependence of the current on the back-gate voltage serves as a test for determining the doping of the material: the decrease in the current with increasing back-gate voltage indicates that the material is p-doped, in agreement with the STS and thermopower measurements for bulk. The gate traces also show that the franckeite flake is strongly doped and it cannot be

switched off within the experimental gate voltage window. Thus, franckeite does not seem an appropriate material to fabricate FETs and requires doping engineering to reduce the intrinsic doping. This measurement was repeated after 41 days, finding a small drop of 5% in the current intensity, which indicates that the device remains stable over time. This is very relevant when comparing with black phosphorus, the other intrinsically doped p-type 2D semiconductor, which degrades on a time scale of a few hours **??**. From the $I_{ds} - V_{ds}$ curve (shown in the inset of Figure B.8) we estimate a resistivity of $\sim 50 m\Omega \cdot m$.

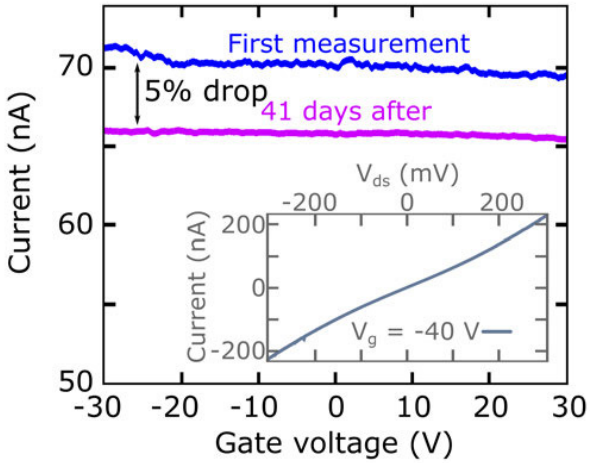

Figure B.8: Current as a function of the applied back-gate voltage in dark conditions for the device shown in Figure B.7 (V_{ds} = 150 mV). The gate-dependence shows a p-type doping, hole conduction. The first measurement (blue line) was repeated after 41 days (pink line), showing a drop of 5%, yielding a good stability of the device. Inset: current-voltage curve with an applied back-gate voltage of -40 V.

B.4.2 Optoelectronic characterization

The absorption spectroscopy of the liquid phase exfoliated material and the STS measurements on bulk franckeite, suggest that franckeite presents a narrow bandgap and, therefore, motivates the application of franckeite as a photodetector working in the NIR (they should be able to generate photocurrent upon illumination with light wavelength as long as $\sim$ 2000 nm). To test the optoelectronic characteristics of our franckeite-based photodetectors, we first study the dependence of the $I_{ds} - V_{ds}$ curves on the illumination with a laser source. The measurements, plotted in Figure B.9, are carried out using a laser of 640 nm wavelength and show that the drain-source current of the photodetector increases with increasing light power over the full range of the gate voltage.

In order to further characterize the photodetector we calculate the responsivity, a typical figure-of-merit for photodetectors that represents the input-output gain of the device as a function

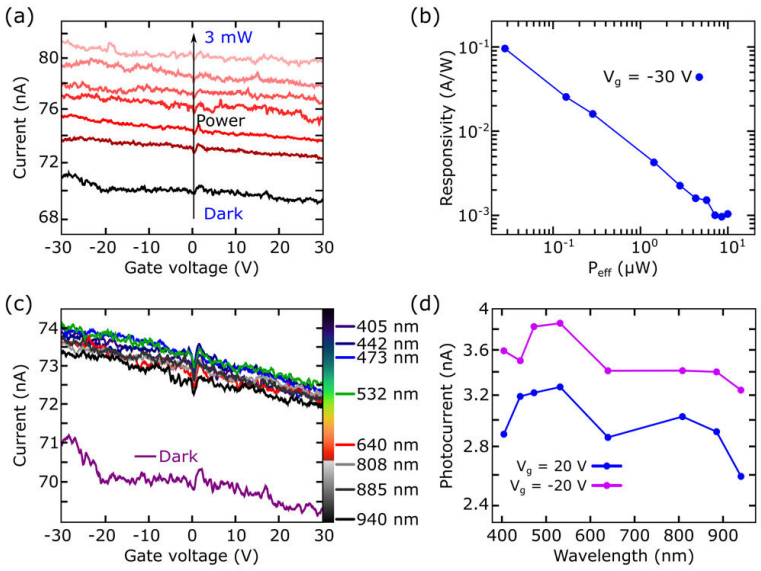

Figure B.9: (a) Current as a function of the applied back-gate voltage (V_{ds} = 150mV) for the device shown in Figure B.7 in dark conditions and upon illumination with a 640 nm wavelength laser with different powers. (b) Responsivity of the device shown in (a) upon illumination with a 640 nm wavelength laser as a function of the laser effective power with an applied back-gate voltage of V_g = -30 V and V_{ds} = 150 mV. (c) Current as a function of the applied back-gate voltage (V_{ds} = 150 mV) for the same device upon ilumination with lasers of different wavelengths at the same intensity (P_d = 6.3 $mW \cdot cm^{-2}$). There is photocurrent generation even at wavelengths as large as 940 nm. (d) Photocurrent as a function of the laser wavelengths with the same light intensity for back gate voltages of -20 V and +20V and V_{ds} = 150 mV.

of the laser effective power reaching the device (Figure B.9(b)). The responsivity (R) is calculated as $R = I_{ph}/P_{eff}$, where I_{ph} (photocurrent) is the difference between the current measured upon illumination and in dark conditions, and Peff is the effective power of the laser that reaches the device ($P_{eff} = P_{laser} \cdot A_{device}/A_{spot}$). For the device shown in Figure B.7, upon illumination at 640 nm, we obtain a maximum responsivity of ~ 100 mA·W^{-1} for a laser intensity of ~ 30 mW·cm^{-2}. Even if this value is not as high as for other two-dimensional photodetectors, such as monolayer MoS_2 (R > 106 mA·W^{-1}) or In_2Se_3 (R > 107 mA·W^{-1}) [103, 162, 227], it is larger than most of the responsivities measured in few-layer black-phosphorus, the two-dimensional phototedector with the narrowest bandgap reported to date [228, 229] ranging from 0.5 mA·W^{-1} to 135 mA·W^{-1} [4, 230, 231].

We have also studied the photocurrent generation in franckeite photodetectors upon illumination in a wide range of light wavelengths (from 405 nm (UV) to 940 nm (NIR)). The $I_{ds} - V_g$ curves, measured in dark conditions and upon illumination with lasers of different wavelengths (Figure B.9(c)), reveal that the device is able to generate photocurrent at wavelengths as large as 940 nm, in good agreement with the results obtained from the UV-Vis-NIR spectroscopy of the

liquid-phase-exfoliated material. The photocurrents calculated from these measurements for two fixed back-gate voltages are plotted in Figure B.9(d).

B.5 MoS_2-franckeite $p-n$ junction

Taking advantage of the simplicity of the deterministic transfer method to build van der Waals heterostructures [230], and the p-doping of franckeite (uncommon in 2D-materials), we fabricated a $p-n$ junction (building blocks of modern electronics) based on the stacking of mechanically-exfoliated franckeite and MoS_2 flakes. Figure B.10(a) and (b) show both optical microscopy and AFM topographic images of the device, which is represented in an artistic drawing in Figure B.10(c): the MoS_2 flake is first deposited by deterministic transfer onto a SiO_2 substrate in contact with one pre-patterned Ti/Au electrode, then a franckeite flake is deposited in contact with the other pre-patterned electrode, resulting in a van der Waals heterostructure made of a p-doped material (franckeite) and an n-doped material (MoS_2) in the overlapping region.

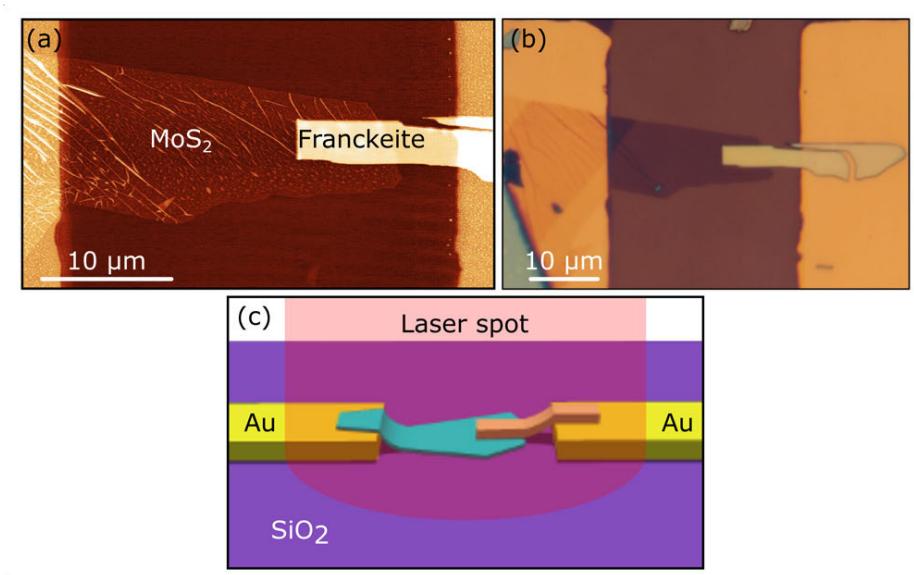

Figure B.10: (a) AFM topographic image of a franckeite-based device. The scan profile yields a thickness ranging from 7 nm to 13.5 nm. (b) Optical microscopy image of the device shown in (a). (c) Artistic representation of the p-n junction shown in (a).

The electronic characterization of the device, carried out in vacuum (P < 10^{-5} mbar), at room temperature and in dark conditions, shows diode-like $I_{ds}-V_g$ characteristics for different back-gate voltages (Figure B.11(a)). The $I_{ds}-V_g$ curve shown in the inset of Figure B.11(a) yields a current rectification ratio of 400 and a gate threshold voltage of V_{th} ~ -10 V. To test the optoelectronic properties, the device is illuminated with laser spots of 940 nm and 885 nm wavelength, indicating that there is photocurrent generation even for zero applied voltage

(short circuit current, I_{sc}) and that the current is zero for a finite positive applied voltage (open circuit voltage, V_{oc}). This phenomena is due to the photovoltaic effect: upon illumination at zero applied voltage, the photogenerated electron-hole pairs are separated by an internal electric field, generating a photocurrent (I_{sc}) with the same sign as the reverse voltage; on the other hand, charge carriers are accumulated at different parts of the device, creating a voltage when the circuit is open (Voc) in the forward voltage direction.

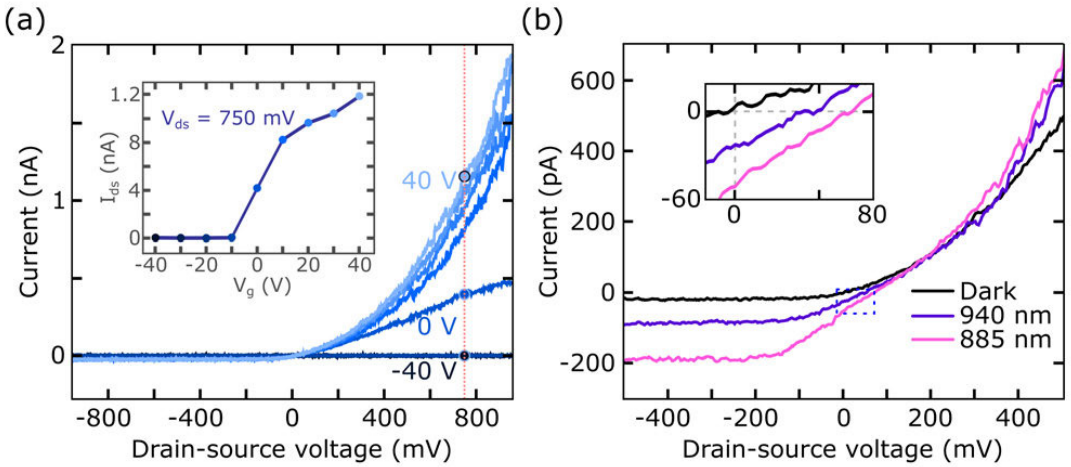

Figure B.11: (a) Diode-like current-voltage ($I_{ds} - V_g$) curve of the $p-n$ junction in dark conditions for different applied back-gate voltages. Inset: gate trace extracted from the $I_{ds} - V_g$ at V_{ds} = 750 mV. The $p-n$ junction switches on at an applied back-gate voltage of 0 V. (b) Diode-like current-voltage ($I_{ds} - V_g$) curve of the $p-n$ junction at an applied back-gate voltage of V_g = 40 V in dark conditions and upon illumination with laser of 940 nm and 885 nm wavelength, both with a power of 140 μW. The inset highlights the region around V_{ds} = 0 V and I_{ds} = 0 V to show the short-circuit current (I_{sc}) and open circuit voltage (V_{oc}) values, obtaining I_{sc} = -27 pA and V_{oc} = 55 mV at 940 nm, and I_{sc} = -51 pA and V_{oc} = 77 mV at 885 nm.

The photocurrent measured upon illumination with laser spots of 940 nm and 885 nm wavelength (Figure B.11(b)) presents I_{sc} = -27 pA and V_{oc} = 55 mV at 940 nm, and I_{sc} = -51 pA and V_{oc} = 77 mV at 885 nm. The current voltage characteristics for different applied back-gate voltages upon illumination are shown in Figure B.12.

We also calculate the electrical power harvested by the $p-n$ junction (Figure B.13), which reaches the maximum values of $P_{el,max} \sim$ 0.5 pW upon illumination with 940 nm and $P_{el,max} \sim$ 1.2 pW upon illumination at 885 nm. We should stress here that optimizing the performance of franckeite-based $p-n$ junction devices is beyond the scope of this work. Nevertheless, these results demonstrate that one can exploit the p-type character of franckeite in electronic devices where a narrow gap, air-stable, p-type semiconductor is needed.

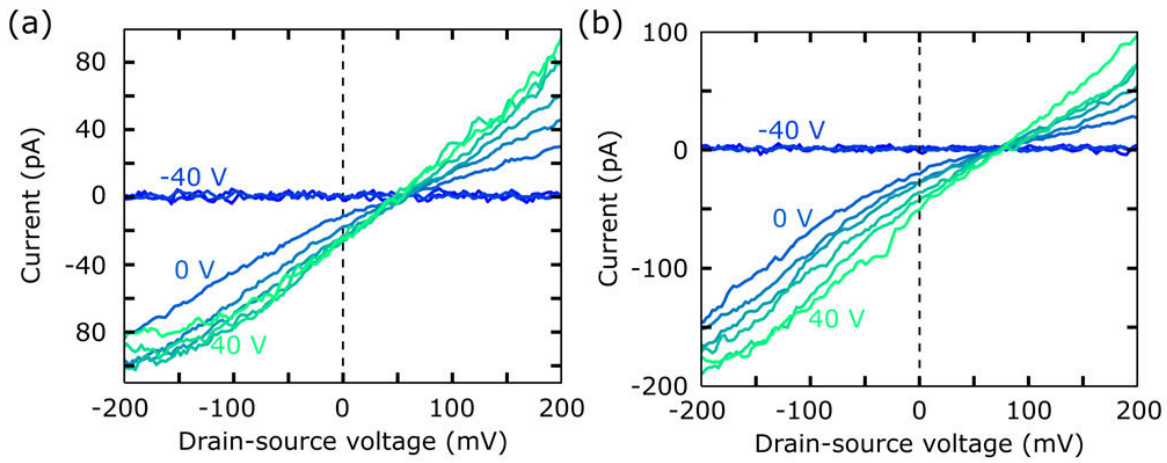

Figure B.12: $P-n$ junction current-voltage characteristics for different back-voltages ranging from -40 V to 40 V upon illumination with (a) 940 nm wavelength and (b) 885 nm wavelength.

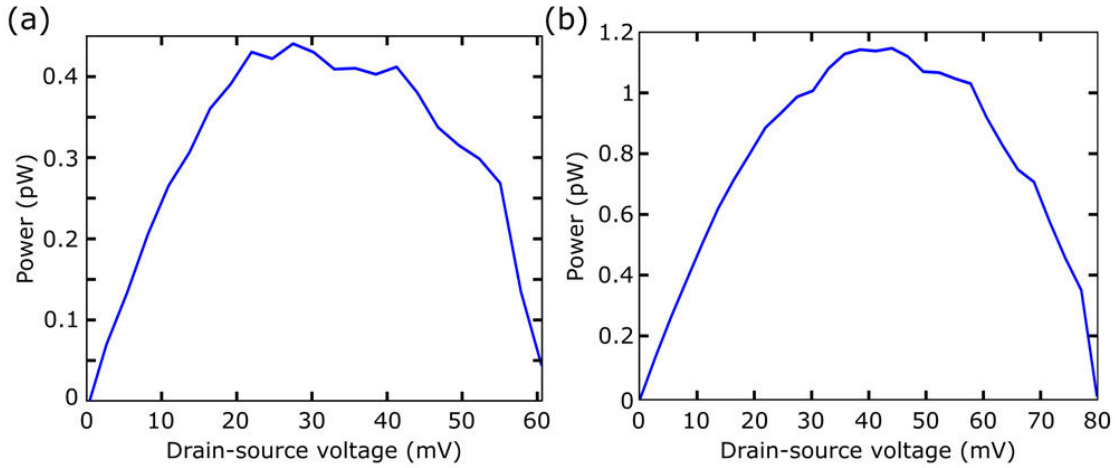

Figure B.13: $P-n$ junction electrical power harvested in the device, calculated as $P_{el} = | I_{ds} | \cdot V_{ds}$ upon illumination with a laser spot of (a) 940 nm wavelength with a $P_{el,max} \sim 0.5$ pW and (b) 885 nm wavelength with a $P_{el,max} \sim 1.2$ pW.

APPENDIX C

APPENDIX C

C.1 Thermogavimetric analysis and mass spectroscopy

We study the stability and plausible generation of defects in TiS_3 at the temperatures reached right before breakdown by performing a thermogravimetric coupled to mass spectrometry analysis of bulk TiS3 both under Ar- or O_2-rich atmosphere. The thermogravimetric analysis (TGA) of TiS_3 in an O2-rich atmosphere shows a total mass release of 36% from room temperature up to 650 °C (Figure C.2). We distinguish two events in the TGA analysis related to the mass release: one event occurs in a temperature range between 300 and 450 °C, exhibiting an important mass release of ≈ 18% related to the presence of O_2, and the second event occurs in a temperature range between 450 and 550 °C, with a mass release of ≈ 18%. The total amount of mass released, as well as the stoichiometry ratio of the decomposed sample (S/Ti = 1.9 ± 0.1 and O/Ti = 2.0 ± 0.2) obtained by energy-dispersive X-ray spectroscopy measurements, indicate that TiS_3 is decomposed into TiS_2 and TiO_2, in agreement with previously reported studies [232].

In fact, mass spectrometry (Figure C.1) confirms that O_2 is starting to be consumed during this event, supporting a reaction between TiS_3 and molecular O that forms an oxysulfide (TiS_{3-xOx}) as an intermediate step on TiO_2 formation [233]. The mass-spectrometry analysis of TiS_3 during the thermal treatment at m/q = 32, attributed to O_2 consumption, is shown in Figure C.1. It is observed that the signal (current) decreases at a small rate while increasing the temperature from room temperature to 300 °C, but it decreases with a higher rate between 300 °C and 550 °C, indicating a higher oxygen consumption in this temperature range, related to a reaction between O_2 and TiS_3. Higher temperatures lead to the decomposition of the remaining TiS_3 into TiS_2, as confirmed by X-ray diffraction analysis (XRD).

The XRD pattern shows the decomposition of the initial monoclinic TiS_3 (Figure C.2(b), blue line) into three crystalline phases (Figure C.2(b), red line): hexagonal titanium disulfide (TiS_2)

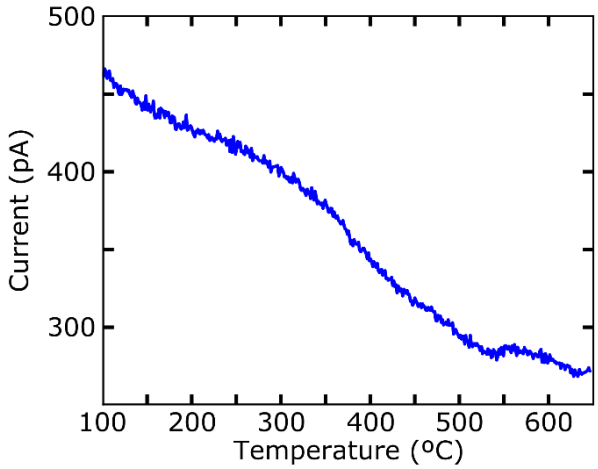

Figure C.1: Ion current signal related to molecular oxygen (m/q = 32) during thermal decomposition of TiS_3. An increase of oxygen consumption from T = 350 °C up to 550 °C is observed (O_2-ion current signal decreases) which is related to the reaction between oxygen and TiS_3.

and titanium dioxide (TiO_2, anatase and rutile), supporting the reaction of O with TiS_3.

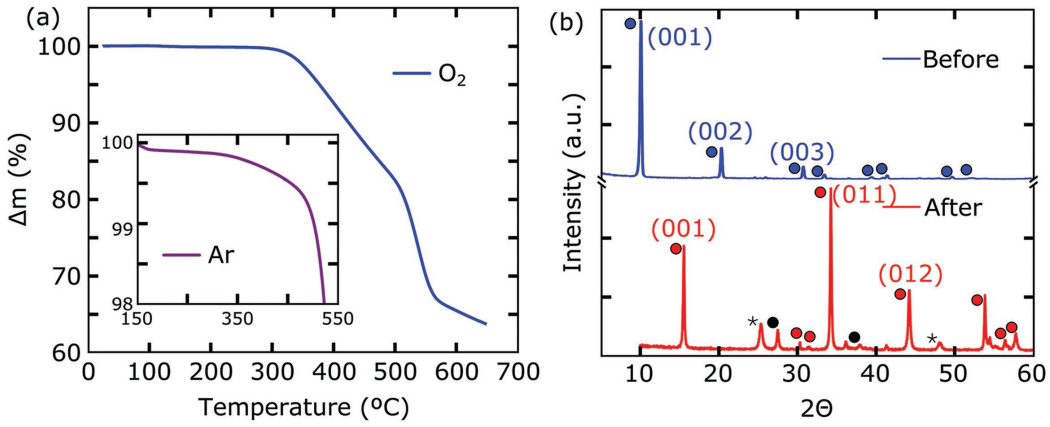

Figure C.2: a) Thermogravimetric analysis of bulk TiS_3 in oxygen atmosphere. Inset: Thermogravimetric analysis of bulk TiS_3 in argon around the first event. b) XRD pattern of TiS_3 as-synthetized (blue line) and after thermal treatment (red line). The blue circles correspond to TiS_3 phase, the red circles correspond to TiS_2 phase, * corresponds to TiO_2 anatase, and the black circles correspond to TiO_2 rutile.

Note that similar thermal events are observed even when the TGA is performed in argon atmosphere (inset of Figure C.2(a)) with a small amount of residual O_2.

Thermogravimetric curves obtained at different heating rates of TiS_3 under argon atmosphere is shown in Figure C.3(a). The activation energies obtained from the non-isothermal Kissinger

method [185] (Figure C.3(b)) using the TGA measurements shown in Figure C.2 are $E_{a,1}$ = 1.5 eV for the first event in the TGA and $E_{a,2}$ = 2.05 eV for the second event in the TGA.

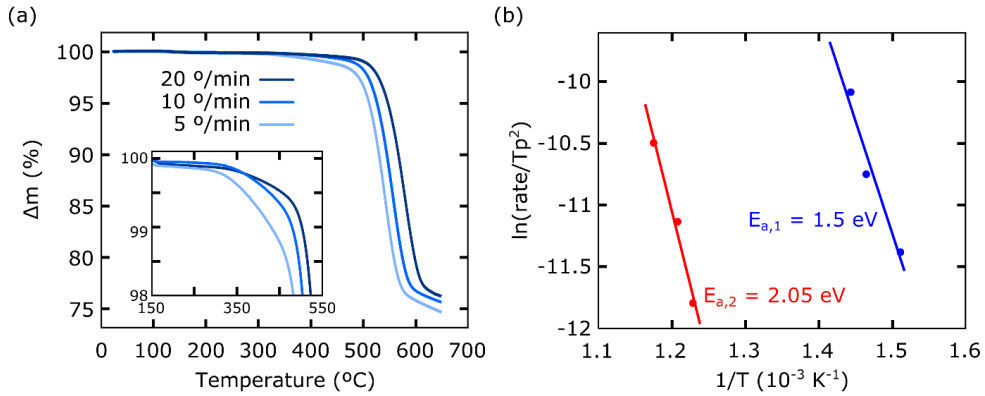

Figure C.3: (a) Thermogravimetric curves obtained at different heating rates of TiS_3 under argon atmosphere. (b) Kissinger plots and calculated activation energies of the two events.

References

[1] Novoselov, K. S., Geim, A. K., Morozov, S. V., Jiang, D., Zhang, Y., Dubonos, S. V., Grigorieva, I. V., and Firsov, A. A. Electric Field Effect in Atomically Thin Carbon Films. *Science*, **306**:666–669 (2004).

[2] Radisavljevic, B., Radenovic, A., Brivio, J., Giacometti, V., and Kis, A. Single-layer Mos_2 transistors. *Nat. Nanotechnol.*, **6**:147–150 (2011).

[3] Das, S., Chen, H.-Y., Penumatcha, A. V., and Appenzeller, J. High Performance Multilayer Mos_2 Transistors with Scandium Contacts. *Nano Lett.*, **13**:100–105 (2013).

[4] Buscema, M., Groenendijk, D. J., Blanter, S. I., Steele, G. A., van der Zant, H. S. J., and Castellanos-Gomez, A. Fast and Broadband Photoresponse of Few-Layer Black Phosphorus Field-Effect Transistors. *Nano Lett.*, **14**:3347–3352 (2014).

[5] Mayorov, A. S., Gorbachev, R. V., Morozov, S. V., Britnell, L., Jalil, R., Ponomarenko, L. A., Blake, P., Novoselov, K. S., Watanabe, K., Taniguchi, T., and Geim, A. K. Micrometer-Scale Ballistic Transport in Encapsulated Graphene at Room Temperature. *Nano Lett.*, **102**:2396–2399 (2011).

[6] Kappera, R., Voiry, D., Yalcin, S. E., Branch, B., Gupta, G., Mohite, A. D., and Chhowalla, M. Phase-engineered low-resistance contacts for ultrathin mos_2 transistors. *Nat Mater*, **13**:1128–1134 (2014).

[7] Ferrari, A. C., Bonaccorso, F., Fal'ko, V., Novoselov, K. S., Roche, S., and Boggild, P. *et.al.*. Science and technology roadmap for graphene, related two-dimensional crystals, and hybrid systems. *Nanoscale*, **7**(11):4598–4810 (2015).

[8] Novoselov, K. S., Jiang, D., Schedin, F., Booth, T. J., Khotkevich, V. V., Morozov, S. V., and Geim, A. K. Two-dimensional atomic crystals. *PNAS*, **102**:10451–10453 (2005).

[9] Mak, K. F., Lee, C., Hone, J., Shan, J., and Heinz, T. F. Atomically Thin MoS_2: A New Direct-Gap Semiconductor. *Phys. Rev. Lett.*, **105**(13):136805 (2010).

[10] Castellanos-Gomez, A., Vicarelli, L., Prada, E., Island, J. O., Narasimha-Acharya, K. L., Blanter, S. I., Groenendijk, D. J., Buscema, M., Steele, G. A., Alvarez, J. V., Zandbergen,

H. W., Palacios, J. J., and Zant, H. S. J. v. d. Isolation and characterization of few-layer black phosphorus. *2D Mater.*, **1**:025001 (2014).

[11] Butler, S. Z., Hollen, S. M., Cao, L., Cui, Y., Gupta, J. A., Gutierrez, H. R., Heinz, T. F., Hong, S. S., Huang, J., and Ismach, A. F. Progress, challenges, and opportunities in two-dimensional materials beyond graphene. *ACS Nano*, **7**(4):2898–2926 (2013).

[12] Wang, Q. H., Kalantar-Zadeh, K., Kis, A., Coleman, J. N., and Strano, M. S. Electronics and optoelectronics of two-dimensional transition metal dichalcogenides. *Nat. Nanotechnol.*, **7**(11):699–712 (2012).

[13] Lin, Z., McCreary, A., Briggs, N., Subramanian, S., Zhang, K., Sun, Y., Li, X., Borys, N. J., Yuan, H., Fullerton-Shirey, S. K., Chernikov, A., Zhao, H., McDonnell, S., Lindenberg, A. M., Xiao, K., LeRoy, B. J., Drndić, M., Hwang, J. C. M., Park, J., Manish Chhowalla, Schaak, R. E., Javey, A., Hersam, M. C., Robinson, J., and Terrones, M. 2D materials advances: from large scale synthesis and controlled heterostructures to improved characterization techniques, defects and applications. *2D Mater.*, **3**(4):042001 (2016).

[14] Zhao, J., Liu, H., Yu, Z., Quhe, R., Zhou, S., Wang, Y., Liu, C. C., Zhong, H., Han, N., Lu, J., Yao, Y., and Wu, K. Rise of silicene: A competitive 2D material. *Prog. in Mater. Sci.*, **83**:24–151 (2016).

[15] Dávila, M. E., Xian, L., Cahangirov, S., Rubio, A., and Lay, G. L. Germanene: a novel two-dimensional germanium allotrope akin to graphene and silicene. *New J. Phys.*, **16**(9):095002 (2014).

[16] Ares, P., Aguilar-Galindo, F., Rodríguez-San-Miguel, D., Aldave, D. A., Díaz-Tendero, S., Alcamí, M., Martín, F., Gómez-Herrero, J., and Zamora, F. Mechanical Isolation of Highly Stable Antimonene under Ambient Conditions. *Adv. Mater.*, **28**(30):6332–6336 (2016).

[17] Cahangirov, S., Topsakal, M., Akturk, E., sahin, H., and Ciraci, S. Two- and One-Dimensional Honeycomb Structures of Silicon and Germanium. *Phys. Rev. Lett.*, **102**(23):236804 (2009).

[18] Lebegue, S., Bjorkman, T., Klintenberg, M., Nieminen, R. M., and Eriksson, O. Two-Dimensional Materials from Data Filtering and Ab Initio Calculations. *Phys. Rev. X*, **3**(3):031002 (2013).

[19] Dai, J. and Zeng, X. C. Titanium Trisulfide Monolayer: Theoretical Prediction of a New Direct-Gap Semiconductor with High and Anisotropic Carrier Mobility. *Angew. Chem. Int. Ed.*, **54**(26):7572–7576 (2015).

[20] Island, J. O., Biele, R., Barawi, M., Clamagirand, J. M., Ares, J. R., Sánchez, C., Zant, H. S. J. v. d., Ferrer, I. J., D'Agosta, R., and Castellanos-Gomez, A. Titanium trisulfide (TiS_3): a 2D semiconductor with quasi-1D optical and electronic properties. *Sci. Rep.*, **6**:22214 (2016).

[21] Island, J. O., Molina-Mendoza, A. J., Barawi, M., Biele, R., Flores, E., Clamagirand, J. M., Ares, J. R., Sánchez, C., Zant, H. S. J. v. d., D'Agosta, R., Ferrer, I. J., and Castellanos-Gomez, A. Electronics and optoelectronics of quasi-1D layered transition metal trichalcogenides. *2D Mater.*, **4**(2):022003 (2017).

[22] Bufler, F. M. and Fichtner, W. Scaling of strained-Si n-MOSFETs into the ballistic regime and associated anisotropic effects. *IEEE Transactions on Electron Devices*, **50**(2):278–284 (2003).

[23] Liu, E., Fu, Y., Wang, Y., Feng, Y., Liu, H., Wan, X., Zhou, W., Wang, B., Shao, L., Ho, C.-H., Huang, Y.-S., Cao, Z., Wang, L., Li, A., Zeng, J., Song, F., Wang, X., Shi, Y., Yuan, H., Hwang, H. Y., Cui, Y., Miao, F., and Xing, D. Integrated digital inverters based on two-dimensional anisotropic ReS_2 field-effect transistors. *Nat. Commun.*, **6**:6991 (2015).

[24] Ferrer, I. J., Ares, J. R., Clamagirand, J. M., Barawi, M., and Sánchez, C. Optical properties of titanium trisulphide (TiS_3) thin films. *Thin Solid Films*, **535**:398–401 (2013).

[25] Island, J. O., Barawi, M., Biele, R., Almazán, A., Clamagirand, J. M., Ares, J. R., Sánchez, C., van der Zant, H. S. J., Álvarez, J. V., D'Agosta, R., Ferrer, I. J., and Castellanos-Gomez, A. TiS_3 Transistors with Tailored Morphology and Electrical Properties. *Adv. Mater.*, **27**(16):2595–2601 (2015).

[26] Molina-Mendoza, A. J., Barawi, M., Biele, R., Flores, E., Ares, J. R., Sánchez, C., Rubio-Bollinger, G., Agrait, N., D'Agosta, R., Ferrer, I. J., and Castellanos-Gomez, A. Electronic Bandgap and Exciton Binding Energy of Layered Semiconductor TiS_3. *Adv. Electron. Mater.*, **1**(11) (2015).

[27] Du, X., Skachko, I., Barker, A., and Andrei, E. Y. Approaching ballistic transport in suspended graphene. *Nat Nano*, **3**(8):491–495 (2008).

[28] Ellis, J. K., Lucero, M. J., and Scuseria, G. E. The indirect to direct band gap transition in multilayered MoS_2 as predicted by screened hybrid density functional theory. *Appl. Phys. Lett.*, **99**(26):261908 (2011).

[29] Jin, Z., Li, X., Mullen, J. T., and Kim, K. W. Intrinsic transport properties of electrons and holes in monolayer transition-metal dichalcogenides. *Phys. Rev. B*, **90**(4):045422 (2014).

[30] Carvalho, A., Wang, M., Zhu, X., Rodin, A. S., Su, H., and Neto, A. H. C. Phosphorene: from theory to applications. *Nat. Rev. Mater.*, **1**:16061 (2016).

[31] Watanabe, K., Taniguchi, T., and Kanda, H. Direct-bandgap properties and evidence for ultraviolet lasing of hexagonal boron nitride single crystal. *Nat. Mater.*, **3**(6):404–409 (2004).

[32] Matthes, L., Pulci, O., and Bechstedt, F. Massive Dirac quasiparticles in the optical absorbance of graphene, silicene, germanene, and tinene. *J. Phys.: Condens. Matter*, **25**(39):395305 (2013).

[33] Houssa, M., Dimoulas, A., and Molle, A. Silicene: a review of recent experimental and theoretical investigations. *J. Phys.: Condens. Matter*, **27**(25):253002 (2015).

[34] Yoon, Y., Ganapathi, K., and Salahuddin, S. How Good Can Monolayer MoS_2 Transistors Be? *Nano Lett.*, **11**(9):3768–3773 (2011).

[35] Cao, W., Kang, J., Sarkar, D., Liu, W., and Banerjee, K. 2D Semiconductor FETs Projections and Design for Sub-10 nm VLSI. *IEEE Transactions on Electron Devices*, **62**(11):3459–3469 (2015).

[36] Sarkar, D., Liu, W., Xie, X., Anselmo, A. C., Mitragotri, S., and Banerjee, K. MoS_2 Field-Effect Transistor for Next-Generation Label-Free Biosensors. *ACS Nano*, **8**(4):3992–4003 (2014).

[37] Lembke, D. and Kis, A. Breakdown of High-Performance Monolayer MoS_2 Transistors. *ACS Nano*, **6**(11):10070–10075 (2012).

[38] Castellanos-Gomez, A., Roldán, R., Cappelluti, E., Buscema, M., Guinea, F., van der Zant, H. S. J., and Steele, G. A. Local Strain Engineering in Atomically Thin MoS_2. *Nano Lett.*, **13**(11):5361–5366 (2013).

[39] Bertolazzi, S., Brivio, J., and Kis, A. Stretching and breaking of ultrathin MoS_2. *ACS Nano*, **5**(12):9703–9709 (2011).

[40] Geim, A. K. and Grigorieva, I. V. Van der Waals heterostructures. *Nature*, **499**(7459):419–425 (2013).

[41] Fiori, G., Bonaccorso, F., Iannaccone, G., Palacios, T., Neumaier, D., Seabaugh, A., Banerjee, S. K., and Colombo, L. Electronics based on two-dimensional materials. *Nat. Nanotechnol.*, **9**(10):768–779 (2014).

[42] Chhowalla, M., Jena, D., and Zhang, H. Two-dimensional semiconductors for transistors. *Nat. Rev. Mater.*, **1**:16052 (2016).

[43] Liu, B., Abbas, A., and Zhou, C. Two-Dimensional Semiconductors: From Materials Preparation to Electronic Applications. *Adv. Elec. Mater.*, page 1700045.

[44] Morkoc, H. and Mohammad, S. N. High-Luminosity Blue and Blue-Green Gallium Nitride Light-Emitting Diodes. *Science*, **267**(5194):51–55 (1995).

[45] Zory, P. S. Quantum Well Lasers ((Academic, 1993)).

[46] Mimura, T., Hiyamizu, S., Fujii, T., and Nanbu, K. A New Field-Effect Transistor with Selectively Doped GaAs/n-$Al_xGa_{1-x}As$ Heterojunctions. *Jpn. J. Appl. Phys.*, **19**(5):L225 (1980).

[47] Levendorf, M. P., Kim, C.-J., Brown, L., Huang, P. Y., Havener, R. W., Muller, D. A., and Park, J. Graphene and boron nitride lateral heterostructures for atomically thin circuitry. *Nature*, **488**(7413):627–632 (2012).

[48] Liu, L., Park, J., Siegel, D. A., McCarty, K. F., Clark, K. W., Deng, W., Basile, L., Idrobo, J. C., Li, A.-P., and Gu, G. Heteroepitaxial Growth of Two-Dimensional Hexagonal Boron Nitride Templated by Graphene Edges. *Science*, **343**(6167):163–167 (2014).

[49] Liu, Z., Ma, L., Shi, G., Zhou, W., Gong, Y., Lei, S., Yang, X., Zhang, J., Yu, J., Hackenberg, K. P., Babakhani, A., Idrobo, J.-C., Vajtai, R., Lou, J., and Ajayan, P. M. In-plane heterostructures of graphene and hexagonal boron nitride with controlled domain sizes. *Nat. Nanotechnol.*, **8**(2):119–124 (2013).

[50] Huang, C., Wu, S., Sanchez, A. M., Peters, J. J., Beanland, R., Ross, J. S., Rivera, P., Yao, W., Cobden, D. H., and Xu, X. Lateral heterojunctions within monolayer $mose_2$–wse_2 semiconductors. *Nat. Mater.*, **13**:1096–1101 (2014).

[51] Cho, S., Kim, S., Kim, J. H., Zhao, J., Seok, J., Keum, D. H., Baik, J., Choe, D.-H., Chang, K. J., Suenaga, K., Kim, S. W., Lee, Y. H., and Yang, H. Phase patterning for ohmic homojunction contact in $MoTe_2$. *Science*, **349**(6248):625–628 (2015).

[52] Novoselov, K. S., Mishchenko, A., Carvalho, A., and Neto, A. H. C. 2D materials and van der Waals heterostructures. *Science*, **353**(6298):aac9439 (2016).

[53] Molina-Mendoza, A. J., Giovanelli, E., Paz, W. S., Niño, M. A., Island, J. O., Evangeli, C., Aballe, L., Foerster, M., Zant, H. S. J. v. d., Rubio-Bollinger, G., Agrait, N., Palacios, J. J., Pérez, E. M., and Castellanos-Gomez, A. Franckeite as a naturally occurring van der Waals heterostructure. *Nat. Commun.*, **8**:14409 (2017).

[54] Feng, B., Ding, Z., Meng, S., Yao, Y., He, X., Cheng, P., Chen, L., and Wu, K. Evidence of Silicene in Honeycomb Structures of Silicon on Ag(111). *Nano Lett.*, **12**(7):3507–3511 (2012).

[55] Ni, Z., Liu, Q., Tang, K., Zheng, J., Zhou, J., Qin, R., Gao, Z., Yu, D., and Lu, J. Tunable Bandgap in Silicene and Germanene. *Nano Lett.*, **12**(1):113–118 (2012).

[56] Lay, G. L., Salomon, E., De Padova, P., Layet, J.-M., and Angot, T. The Rise of Elemental Two-Dimensional Materials Beyond Graphene. *Aust. J. Chem.*, **67**(10):1370–1372 (2014).

[57] Bundy, F. P. Phase Diagrams of Silicon and Germanium to 200 kbar, 1000 C. *The J. of Chem. Phys.*, **41**(12):3809–3814 (1964).

[58] Aufray, B., Kara, A., Vizzini, S., Oughaddou, H., Léandri, C., Ealet, B., and Le Lay, G. Graphene-like silicon nanoribbons on Ag(110): A possible formation of silicene. *Appl. Phys. Lett.*, **96**(18):183102 (2010).

[59] De Padova, P., Quaresima, C., Ottaviani, C., Sheverdyaeva, P. M., Moras, P., Carbone, C., Topwal, D., Olivieri, B., Kara, A., Oughaddou, H., Aufray, B., and Le Lay, G. Evidence of graphene-like electronic signature in silicene nanoribbons. *Appl. Phys. Lett.*, **96**(26):261905 (2010).

[60] Ye, X.-S., Shao, Z.-G., Zhao, H., Yang, L., and Wang, C.-L. Intrinsic carrier mobility of germanene is larger than graphene's: first-principle calculations. *RSC Adv.*, **4**(41):21216–21220 (2014).

[61] Liu, C.-C., Jiang, H., and Yao, Y. Low-energy effective Hamiltonian involving spin-orbit coupling in silicene and two-dimensional germanium and tin. *Phys. Rev. B*, **84**(19):195430 (2011).

[62] Ling, X., Wang, H., Huang, S., Xia, F., and Dresselhaus, M. S. The renaissance of black phosphorus. *PNAS*, 112(15):4523–4530 (2015).

[63] Island, J. O., Steele, G. A., Zant, H. S. J. v. d., and Castellanos-Gomez, A. Environmental instability of few-layer black phosphorus. *2D Mater.*, **2**(1):011002 (2015).

[64] Gibaja, C., Rodriguez-San-Miguel, D., Ares, P., Gómez-Herrero, J., Varela, M., Gillen, R., Maultzsch, J., Hauke, F., Hirsch, A., Abellán, G., and Zamora, F. Few-Layer Antimonene by Liquid-Phase Exfoliation. *Angew. Chem. Int. Ed.*, **55**(46):14345–14349 (2016).

[65] Nicolosi, V., Chhowalla, M., Kanatzidis, M. G., Strano, M. S., and Coleman, J. N. Liquid Exfoliation of Layered Materials. *Science*, **340**(6139):1226419 (2013).

[66] Zhang, S., Xie, M., Li, F., Yan, Z., Li, Y., Kan, E., Liu, W., Chen, Z., and Zeng, H. Semiconducting Group‚ÄÖ15 Monolayers: A Broad Range of Band Gaps and High Carrier Mobilities. *Angew. Chem. Int. Ed.*, **55**(5):1666–1669 (2016).

[67] Wang, Y. and Ding, Y. Electronic Structure and Carrier Mobilities of Arsenene and Antimonene Nanoribbons: A First-Principle Study. *Nanoscale Res. Lett.*, **10**(1):254 (2015).

[68] Zhao, M., Zhang, X., and Li, L. Strain-driven band inversion and topological aspects in Antimonene. *Sci. Rep.*, **5**:16108 (2015).

[69] Fu, L., Kane, C. L., and Mele, E. J. Topological Insulators in Three Dimensions. *Phys. Rev. Lett.*, **98**(10):106803 (2007).

[70] Hohenberg, P. and Kohn, W. Inhomogeneous electron gas. *Phys. Rev.*, **136**:B864 (1964).

[71] Grosso, G. and Pastori Parravicini, G. *Solid States Physics*, volume 2. Elsevier (2014).

[72] Neto, A. C., Guinea, F., Peres, N. M., Novoselov, K. S., and Geim, A. K. The electronic properties of graphene. *Rev. Mod. Phys.*, **81**(1):109 (2009).

[73] Reich, S., Maultzsch, J., Thomsen, C., and Ordejon, P. Tight-binding description of graphene. *Phys. Rev. B*, **66**:035412 (2002).

[74] Wallace, P. R. The band theory of graphite. *Phys. Rev.*, **71**:622 (1947).

[75] Odom, T. W., Huang, J.-L., Kim, P., and Lieber, C. M. Structure and electronic properties of carbon nanotubes. *J. Phys. Chem. B*, **104**:2794–2809 (2000).

[76] Son, Y.-W., Cohen, M. L., and Louie, S. G. Energy gaps in graphene nanoribbons. *Phys. Rev. Lett.*, **97**:216803 (2006).

[77] Liu, G.-B., Shan, W.-Y., Yao, Y., Yao, W., and Xiao, D. Three-band tight-binding model for monolayers of group-vib transition metal dichalcogenides. *Phys. Rev. B*, **88**:085433 (2013).

[78] Roldán, R., López-Sancho, M. P., Guinea, F., Cappelluti, E., Silva-Guillén, J., and Ordejón, P. Momentum dependence of spin–orbit interaction effects in single-layer and multi-layer transition metal dichalcogenides. *2D Mater.*, **1**:034003 (2014).

[79] Cappelluti, E., Roldán, R., Silva-Guillén, J. A., Ordejón, P., and Guinea, F. Tight-binding model and direct-gap/indirect-gap transition in single-layer and multilayer mos_2. *Phys. Rev. B*, **88**:075409 (2013).

[80] Jacob, D. and Palacios, J. J. Critical comparison of electrode models in density functional theory based quantum transport calculations. *J. Chem Phys.*, **134**(4):044118 (2011).

[81] Kalos, M. A. and Whitlock, P. A. *Monte Carlo Methods, Vol 1.: Basics, Courant Institute of Mathematical Sciences, New York University*. John Wiley & Sons (1986).

[82] Slater, J. C. and Koster, G. F. Simplified lcao method for the periodic potential problem. *Phys. Rev.*, **94**:1498 (1954).

[83] Harrison, W. A. Elementary electronic structure (revised edition). *(World Scientific Publishing Co., Singapore, 2004)*.

[84] Agrait, N., Yeyati, A. L., and van Ruitenbeek, J. M. Quantum properties of atomic-sized conductors. *Phys. Rep.*, **377**(2-3):81–279 (2003).

[85] Datta, S. Electronic transport in mesoscopic systems. *Cambridge University Press, Cambridge, 1997*, (44-46).

[86] Landauer, R. Spatial variation of currents and fields due to localized scatterers in metallic conduction. *IBM Journal of Research and Development*, **1**(3):223–231 (1957).

[87] Economou, E. N. Green's functions in quantum mechanics. *Springer, Berlin, 2006*.

[88] Jacob, D. Spin transport in nanocontacts and nanowires. *Ph.D. thesis, Universidad de Alicante (2007)*.

[89] Caroli, C., Combescot, R., Lederer, D., Nozieres, P., and Saint-James, D. A direct calculation of the tunnelling current. II. Free electron description. *J. Phys. C: Solid State Phys.*, **4**(16):2598 (1971).

[90] Radisavljevic, B. and Kis, A. Mobility engineering and a metal–insulator transition in monolayer mos2. *Nat. Mater.*, **12**(9):815–820 (2013).

[91] Wang, L., Meric, I., Huang, P., Gao, Q., Gao, Y., Tran, H., Taniguchi, T., Watanabe, K., Campos, L., Muller, D., et al. One-dimensional electrical contact to a two-dimensional material. *Science*, **342**(6158):614–617 (2013).

[92] Castellanos-Gomez, A., Barkelid, M., Goossens, A. M., Calado, V. E., van der Zant, H. S., and Steele, G. A. Laser-thinning of mos_2: on demand generation of a single-layer semiconductor. *Nano Lett.*, **12**(6):3187–3192 (2012).

[93] Radisavljevic, B., Radenovic, A., Brivio, J., Giacometti, V., and Kis, A. Single-layer mos_2 transistors. *Nat. Nanotechnol.*, **6**(3):147–150 (2011).

[94] Yoon, Y., Ganapathi, K., and Salahuddin, S. How good can monolayer mos2 transistors be? *Nano Lett*, **11**(9):3768–3773 (2011).

[95] Fuhrer, M. S. and Hone, J. Measurement of mobility in dual-gated mos2 transistors. *Nat. Nanotechnol.*, **8**(3):146–147 (2013).

[96] Jariwala, D., Sangwan, V. K., Lauhon, L. J., Marks, T. J., and Hersam, M. C. Emerging device applications for semiconducting two-dimensional transition metal dichalcogenides. *ACS Nano*, **8**(2):1102–1120 (2014).

[97] Xia, F., Wang, H., and Jia, Y. Rediscovering black phosphorus as an anisotropic layered material for optoelectronics and electronics. *Nat. Commun.*, **5**(3087) (2014).

[98] Das, S. and Appenzeller, J. Where does the current flow in two-dimensional layered systems? *Nano Lett.*, **13**(7):3396–3402 (2013).

[99] Chang, H.-Y., Zhu, W., and Akinwande, D. On the mobility and contact resistance evaluation for transistors based on mos2 or two-dimensional semiconducting atomic crystals. *Appl. Phys. Lett.*, **104**(11):113504 (2014).

[100] Liu, H., Neal, A. T., and Ye, P. D. Channel length scaling of mos2 mosfets. *ACS Nano*, **6**(10):8563–8569 (2012).

[101] Liu, H., Si, M., Deng, Y., Neal, A. T., Du, Y., Najmaei, S., Ajayan, P. M., Lou, J., and Ye, P. D. Switching mechanism in single-layer molybdenum disulfide transistors: an insight into current flow across schottky barriers. *ACS Nano*, **8**(1):1031–1038 (2013).

[102] McDonnell, S., Addou, R., Buie, C., Wallace, R. M., and Hinkle, C. L. Defect-dominated doping and contact resistance in mos_2. *ACS Nano*, **8**(3):2880–2888 (2014).

[103] Lopez-Sanchez, O., Lembke, D., Kayci, M., Radenovic, A., and Kis, A. Ultrasensitive photodetectors based on monolayer mos2. *Nat. Nanotechnol.*, **8**(7):497–501 (2013).

[104] Krasnozhon, D., Lembke, D., Nyffeler, C., Leblebici, Y., and Kis, A. Mos2 transistors operating at gigahertz frequencies. *Nano Lett.*, **14**(10):5905–5911 (2014).

[105] Liu, H., Si, M., Najmaei, S., Neal, A. T., Du, Y., Ajayan, P. M., Lou, J., and Ye, P. D. Statistical study of deep submicron dual-gated field-effect transistors on monolayer chemical vapor deposition molybdenum disulfide films. *Nano Lett.*, **13**(6):2640–2646 (2013).

[106] Allain, A., Kang, J., Banerjee, K., and Kis, A. Electrical contacts to two-dimensional semiconductors. *Nat. Mater.*, **14**(12):1195–1205 (2015).

[107] Giovannetti, G., Khomyakov, P., Brocks, G., Karpan, V. v., Van den Brink, J., and Kelly, P. Doping graphene with metal contacts. *Phys. Rev. Lett.*, 101(2):026803 (2008).

[108] Gong, K., Zhang, L., Ji, W., and Guo, H. Electrical contacts to monolayer black phosphorus: A first-principles investigation. *Phys. Rev. B*, **90**(12):125441 (2014).

[109] Wang, L., Meric, I., Huang, P. Y., Gao, Q., Gao, Y., Tran, H., Taniguchi, T., Watanabe, K., Campos, L. M., Muller, D. A., Guo, J., Kim, P., Hone, J., Shepard, K. L., and Dean, C. R. One-dimensional electrical contact to a two-dimensional material. *Science*, **342**(6158):614–617 (2013).

[110] Kappera, R., Voiry, D., Yalcin, S. E., Branch, B., Gupta, G., Mohite, A. D., and Chhowalla, M. Phase-engineered low-resistance contacts for ultrathin mos_2 transistors. *Nat Mater*, **13**(12):1128–1134 (2014).

[111] Eda, G., Fujita, T., Yamaguchi, H., Voiry, D., Chen, M., and Chhowalla, M. Coherent atomic and electronic heterostructures of single-layer MoS_2. *ACS Nano*, **6**(8):7311–7317 (2012).

[112] Eda, G., Yamaguchi, H., Voiry, D., Fujita, T., Chen, M., and Chhowalla, M. Photoluminescence from chemically exfoliated MoS_2. *Nano Lett.*, **11**(12):5111–5116 (2011).

[113] Chhowalla, M., Shin, H. S., Eda, G., Li, L.-J., Loh, K. P., and Zhang, H. The chemistry of two-dimensional layered transition metal dichalcogenide nanosheets. *Nat. Chem.*, **5**(4):263–275 (2013).

[114] Léonard, F. and Tersoff, J. Role of fermi-level pinning in nanotube schottky diodes. *Phys. Rev. Lett.*, **84**(20):4693 (2000).

[115] Giannozzi, P., Baroni, S., Bonini, N., Calandra, M., Car, R., Cavazzoni, C., Ceresoli, D., Chiarotti, G. L., Cococcioni, M., Dabo, I., et al. Quantum espresso: a modular and open-source software project for quantum simulations of materials. *J Phys: Condens. Matter*, **21**:395502 (2009).

[116] Perdew, J. P., Burke, K., and Ernzerhof, M. Generalized gradient approximation made simple. *Phys. Rev. Lett.*, 77(18):3865 (1996).

[117] Monkhorst, H. J. and Pack, J. D. Special points for brillouin-zone integrations. *Phys. Rev. B*, **13**(12):5188 (1976).

[118] Slater, J. C. and Koster, G. F. Simplified lcao method for the periodic potential problem. *Phys. Rev.*, **94**(6):1498 (1954).

[119] Shi, H., Pan, H., Zhang, Y.-W., and Yakobson, B. I. Quasiparticle band structures and optical properties of strained monolayer MoS_2 and WS_2. *Phys. Rev. B*, **87**(15):155304 (2013).

[120] Wilson, J. A. and Yoffe, A. D. The transition metal dichalcogenides discussion and interpretation of the observed optical, electrical and structural properties. *Adv. Phys.*, **18**(73):193–335 (1969).

[121] Fives, K., McGovern, I. T., McGrath, R., Cimino, R., Hughes, G., McKinley, A., and Thornton, G. The photoelectron bandstructure of molybdenum disulphide. *J Phys: Condens. Matter*, **4**(25):5639 (1992).

[122] Qian, X., Liu, J., Fu, L., and Li, J. Quantum spin hall effect in two-dimensional transition metal dichalcogenides. *Science*, **346**(6215):1344–1347 (2014).

[123] Li, Y., Zhou, Z., Zhang, S., and Chen, Z. Mos2 nanoribbons: high stability and unusual electronic and magnetic properties. *J Am. Chem. Soc.*, **130**(49):16739–16744 (2008).

[124] Botello-Méndez, A. R., Lopez-Urias, F., Terrones, M., and Terrones, H. Metallic and ferromagnetic edges in molybdenum disulfide nanoribbons. *Nanotechnology*, **20**(32):325703 (2009).

[125] Landauer, R. Electrical resistance of disordered one-dimensional lattices. *Philos. Mag.*, **21**(172):863–867 (1970).

[126] Dean, C. R., Young, A. F., Meric, I., Lee, C., Wang, L., Sorgenfrei, S., Watanabe, K., Taniguchi, T., Kim, P., Shepard, K. L., and Hone, J. Boron nitride substrates for high-quality graphene electronics. *Nat. Nanotechnol.*, **5**(10):722–726 (2010).

[127] Bae, S., Kim, H., Lee, Y., Xu, X., Park, J.-S., Zheng, Y., Balakrishnan, J., Lei, T., Ri Kim, H., Song, Y. I., Kim, Y.-J., Kim, K. S., Ozyilmaz, B., Ahn, J.-H., Hong, B. H., and Iijima, S. Roll−to−roll production of 30−inch graphene films for transparent electrodes. *Nat. Nanotechnol.*, **5**(8):574–578 (2010).

[128] Yang, W., Chen, G., Shi, Z., Liu, C.-C., Zhang, L., Xie, G., Cheng, M., Wang, D., Yang, R., Shi, D., Watanabe, K., Taniguchi, T., Yao, Y., Zhang, Y., and Zhang, G. Epitaxial growth of single-domain graphene on hexagonal boron nitride. *Nat. Mater.*, **12**(9):792–797 (2013).

[129] Gong, Y., Lin, J., Wang, X., Shi, G., Lei, S., Lin, Z., Zou, X., Ye, G., Vajtai, R., Yakobson, B. I., et al. Vertical and in-plane heterostructures from WS_2/MoS_2 monolayers. *Nat. Mater.*, **13**:1135–1142 (2014).

[130] Zhang, X., Meng, F., Christianson, J. R., Arroyo-Torres, C., Lukowski, M. A., Liang, D., Schmidt, J. R., and Jin, S. Vertical Heterostructures of Layered Metal Chalcogenides by van der Waals Epitaxy. *Nano Lett.*, **14**(6):3047–3054 (2014).

[131] Ponomarenko, L. A., Geim, A. K., Zhukov, A. A., Jalil, R., Morozov, S. V., Novoselov, K. S., Grigorieva, I. V., Hill, E. H., Cheianov, V. V., Fal'ko, V. I., Watanabe, K., Taniguchi, T., and Gorbachev, R. V. Tunable metal-insulator transition in double-layer graphene heterostructures. *Nat. Phys.*, **7**(12):958–961 (2011).

[132] Georgiou, T., Jalil, R., Belle, B. D., Britnell, L., Gorbachev, R. V., Morozov, S. V., Kim, Y.-J., Gholinia, A., Haigh, S. J., Makarovsky, O., Eaves, L., Ponomarenko, L. A., Geim, A. K., Novoselov, K. S., and Mishchenko, A. Vertical field-effect transistor based on graphene-WS_2 heterostructures for flexible and transparent electronics. *Nat. Nanotechnol.*, **8**(2):100–103 (2013).

[133] Bertolazzi, S., Krasnozhon, D., and Kis, A. Nonvolatile Memory Cells Based on MoS_2/Graphene Heterostructures. *ACS Nano*, **7**(4):3246–3252 (2013).

[134] Hunt, B., Sanchez-Yamagishi, J. D., Young, A. F., Yankowitz, M., LeRoy, B. J., Watanabe, K., Taniguchi, T., Moon, P., Koshino, M., Jarillo-Herrero, P., and Ashoori, R. C. Massive Dirac Fermions and Hofstadter Butterfly in a van der Waals Heterostructure. *Science*, **340**(6139):1427–1430 (2013).

[135] Withers, F., Del Pozo-Zamudio, O., Mishchenko, A., Rooney, A. P., Gholinia, A., Watanabe, K., Taniguchi, T., Haigh, S. J., Geim, A. K., Tartakovskii, A. I., and Novoselov, K. S. Light-emitting diodes by band-structure engineering in van der Waals heterostructures. *Nat. Mater.*, **14**(3):301–306 (2015).

[136] Pizzocchero, F., Gammelgaard, L., Jessen, B. S., Caridad, J. M., Wang, L., Hone, J., Boggild, P., and Booth, T. J. The hot pick-up technique for batch assembly of van der Waals heterostructures. *Nat. Commun.*, **7**:11894 (2016).

[137] Ross, J. S., Klement, P., Jones, A. M., Ghimire, N. J., Yan, J., Mandrus, D. G., Taniguchi, T., Watanabe, K., Kitamura, K., Yao, W., Cobden, D. H., and Xu, X. Electrically tunable excitonic light-emitting diodes based on monolayer WSe_2 p-n junctions. *Nat. Nanotechnol.*, **9**(4):268–272 (2014).

[138] Baugher, B. W. H., Churchill, H. O. H., Yang, Y., and Jarillo-Herrero, P. Optoelectronic devices based on electrically tunable p-n diodes in a monolayer dichalcogenide. *Nat. Nanotechnol.*, **9**(4):262–267 (2014).

[139] Li, L., Yu, Y., Ye, G. J., Ge, Q., Ou, X., Wu, H., Feng, D., Chen, X. H., and Zhang, Y. Black phosphorus field-effect transistors. *Nat. Nanotechnol.*, **9**(5):372–377 (2014).

[140] Liu, H., Neal, A. T., Zhu, Z., Luo, Z., Xu, X., Tománek, D., and Ye, P. D. Phosphorene: An Unexplored 2D Semiconductor with a High Hole Mobility. *ACS Nano*, **8**(4):4033–4041 (2014).

[141] Makovicky, E., Petricek, V., Dusek, M., and Topa, D. The crystal structure of franckeite: $Pb_{21.7}Sn_{9.3}Fe_{4.0}Sb_{8.1}s_{56.9}$. *American Mineralogist*, **96**:1686–1702 (2011).

[142] Henriksen, R. B., Makovicky, E., Stipp, S., Nissen, C., and Eggleston, C. M. Atomic-scale observations of franckeite surface morphology. *American Mineralogist*, **87**:1273–1278 (2002).

[143] Prior, G. On teallite, a new sulphostannite of lead from bolivia and its relation to franckeite and cylindrite. *Mineralogical Magazine*, **14**:21–27 (1904).

[144] Mottana A, P. G., Fiori S. Improved x-ray powder diffraction data for franckeite. *Powder Diffraction*, **7**(2):112–114 (2013).

[145] Williams, T. B. and Hyde, B. G. Electron microscopy of cylindrite and franckeite. *Phys. Chem. Min.*, **15**(6):521–544 (1988).

[146] Aballe, L., Foerster, M., Pellegrin, E., Nicolas, J., and Ferrer, S. The ALBA spectroscopic LEEM-PEEM experimental station: layout and performance. *J. Synchrotron. Rad., J. Synchrotron. Radiat.*, **22**(3):745–752 (2015).

[147] Maccariello, D., Garnica, M., Niño, M. A., Navío, C., Perna, P., Barja, S., Vázquez de Parga, A. L., and Miranda, R. Spatially Resolved, Site-Dependent Charge Transfer and Induced Magnetic Moment in TCNQ Adsorbed on Graphene. *Chem. Mater.*, **26**(9) (2014).

[148] Wang, S. and Kuo, K. H. Crystal lattices and crystal chemistry of cylindrite and franckeite. *Acta Cryst A, Acta Cryst Sect A, Acta Crystallogr A, Acta Crystallogr Sect A, Acta Crystallogr A Found Crystallogr, Acta Crystallogr Sect A Found Crystallogr*, **47**(4):381–392 (1991).

[149] Crampin, S., Jensen, H., Kroger, J., Limot, L., and Berndt, R. Resonator design for use in scanning tunneling spectroscopy studies of surface electron lifetimes. *Phys. Rev. B*, **72**(3):035443 (2005).

[150] Heyd, J., Scuseria, G. E., and Ernzerhof, M. Hybrid functionals based on a screened coulomb potential. *The Journal of Chemical Physics*, **118**(18):8207–8215 (2003).

[151] Heyd, J., Scuseria, G. E., and Ernzerhof, M. Erratum:„Äúhybrid functionals based on a screened coulomb potential„Äù[j. chem. phys. 118, 8207 (2003)]. *The Journal of Chemical Physics*, **124**(21):219906 (2006).

[152] Heyd, J., Peralta, J. E., Scuseria, G. E., and Martin, R. L. Energy band gaps and lattice parameters evaluated with the Heyd-Scuseria-Ernzerhof screened hybrid functional. *The J. of Chem. Phys.*, **123**(17):174101 (2005).

[153] Troullier, N. and Martins, J. L. Efficient pseudopotentials for plane-wave calculations. *Phys. Rev. B*, **43**(3):1993 (1991).

[154] Bader, R. F. W. Atoms in molecules. *Acc. Chem. Res.*, **18**(1):9–15 (1985).

[155] Henkelman, G., Arnaldsson, A., and Jónsson, H. A fast and robust algorithm for Bader decomposition of charge density. *Computational Materials Science*, 36(3):354–360 (2006).

[156] Baldereschi, A., Baroni, S., and Resta, R. Band Offsets in Lattice-Matched Heterojunctions: A Model and First-Principles Calculations for GaAs/AlAs. *Phys. Rev. Lett.*, **61**(6):734–737 (1988).

[157] Terrones, H., López-Urías, F., and Terrones, M. Novel hetero-layered materials with tunable direct band gaps by sandwiching different metal disulfides and diselenides. *Sci. Rep.*, **3**:1549 (2013).

[158] Pop, E., Sinha, S., and Goodson, K. E. Heat Generation and Transport in Nanometer-Scale Transistors. *Proceedings of the IEEE*, **94**(8):1587–1601 (2006).

[159] Pop, E. Energy dissipation and transport in nanoscale devices. *Nano Res.*, **3**(3):147–169 (2010).

[160] Fang, H., Chuang, S., Chang, T. C., Takei, K., Takahashi, T., and Javey, A. High-Performance Single Layered WSe_2 p-FETs with Chemically Doped Contacts. *Nano Lett.*, **12**(7):3788–3792 (2012).

[161] Li, H., Wu, J., Yin, Z., and Zhang, H. Preparation and Applications of Mechanically Exfoliated Single-Layer and Multilayer MoS_2 and WSe_2 Nanosheets. *Acc. Chem. Res.*, **47**(4):1067–1075 (2014).

[162] Island, J. O., Blanter, S. I., Buscema, M., van der Zant, H. S. J., and Castellanos-Gomez, A. Gate Controlled Photocurrent Generation Mechanisms in High-Gain In_2se_3 Phototransistors. *Nano Lett.*, **15**(12):7853–7858 (2015).

[163] Buscema, M., Island, J. O., Groenendijk, D. J., Blanter, S. I., Steele, G. A., Zant, H. S. J. v. d., and Castellanos-Gomez, A. Photocurrent generation with two-dimensional van der Waals semiconductors. *Chem. Soc. Rev.*, **44**(11):3691–3718 (2015).

[164] Pawbake, A. S., Island, J. O., Flores, E., Ares, J. R., Sanchez, C., Ferrer, I. J., Jadkar, S. R., van der Zant, H. S. J., Castellanos-Gomez, A., and Late, D. J. Temperature-Dependent Raman Spectroscopy of Titanium Trisulfide (TiS_3) Nanoribbons and Nanosheets. *ACS Appl. Mater. Interfaces*, **7**(43):24185–24190 (2015).

[165] Lipatov, A., Wilson, P. M., Shekhirev, M., Teeter, J. D., Netusil, R., and Sinitskii, A. Few-layered titanium trisulfide (TiS_3) field-effect transistors. *Nanoscale*, **7**(29):12291–12296 (2015).

[166] Island, J. O., Buscema, M., Barawi, M., Clamagirand, J. M., Ares, J. R., Sánchez, C., Ferrer, I. J., Steele, G. A., van der Zant, H. S. J., and Castellanos-Gomez, A. Ultrahigh Photoresponse of Few-Layer TiS_3 Nanoribbon Transistors. *Adv. Opt. Mater.*, **2**(7):641–645 (2014).

[167] Dai, J. and Zeng, X. C. Titanium Trisulfide Monolayer: Theoretical Prediction of a New Direct-Gap Semiconductor with High and Anisotropic Carrier Mobility. *Angew. Chem. Int. Ed.*, **54**(26):7572–7576 (2015).

[168] Furuseth, S., Brattas, L., and Kjekshus, A. On the crystal structures of tis_3, zrs_3, $zrse_3$, $zrte_3$, hfs_3, and $hfse_3$. *Acta Chem. Scand.*, **29a**:623–631 (1975).

[169] Gard, P., Cruege, F., Sourisseau, C., and Gorochov, O. Single-crystal micro-Raman studies of ZrS_3, TiS_3 and several $Zr_{1-x}Ti_xS_3$ compounds (0. *J. Raman Spectrosc.*, **17**(3):283–288 (1986).

[170] Li, S.-L., Komatsu, K., Nakaharai, S., Lin, Y.-F., Yamamoto, M., Duan, X., and Tsukagoshi, K. Thickness Scaling Effect on Interfacial Barrier and Electrical Contact to Two-Dimensional MoS_2 Layers. *ACS Nano*, **8**(12):12836–12842 (2014).

[171] Yang, R., Wang, Z., and X.-L. Feng, P. Electrical breakdown of multilayer MoS_2 field-effect transistors with thickness-dependent mobility. *Nanoscale*, **6**(21):12383–12390 (2014).

[172] Island, J. O., Holovchenko, A., Koole, M., Alkemade, P. F. A., Menelaou, M., Aliaga-Alcalde, N., Burzurí, E., and Zant, H. S. J. v. d. Fabrication of hybrid molecular devices using multi-layer graphene break junctions. *J. Phys.: Condens. Matter*, **26**(47):474205 (2014).

[173] S. Lau, C., A. Mol, J., H. Warner, J., and D. Briggs, G. A. Nanoscale control of graphene electrodes. *Phys. Chem. Chem. Phys.*, **16**(38):20398–20401 (2014).

[174] Molares, M. E. T., Hohberger, E. M., Schaeflein, C., Blick, R. H., Neumann, R., and Trautmann., C. Electrical characterization of electrochemically grown single copper nanowires. *Appl. Phys. Lett.*, **82**(13):2139–2141 (2003).

[175] Nie, A., Liu, J., Dong, C., and Wang, H. Electrical failure behaviors of semiconductor oxide nanowires. *Nanotechnol.*, **22**(40):405703 (2011).

[176] Wurz, J., Vj, L., Sarkar, A., and Islam, M. S. *8th IEEE Conf. Nanotechnol*, page DOI: 10.1109/NANO.2008.176 (2008).

[177] Westover, T., Jones, R., Huang, J. Y., Wang, G., Lai, E., and Talin, A. A. Photoluminescence, Thermal Transport, and Breakdown in Joule-Heated GaN Nanowires. *Nano Lett.*, **9**(1):257–263 (2009).

[178] Suzuki, M., Ominami, Y., Ngo, Q., Yang, C. Y., Cassell, A. M., and Li, J. Current-induced breakdown of carbon nanofibers. *J. of Appl. Phys.*, **101**(11):114307 (2007).

[179] Murali, R., Yang, Y., Brenner, K., Beck, T., and Meindl, J. D. Breakdown current density of graphene nanoribbons. *Appl. Phys. Lett.*, **94**(24):243114 (2009).

[180] Zhang, Q., Qi, J., Yang, Y., Huang, Y., Li, X., and Zhang, Y. Electrical breakdown of zno nanowires in metal-semiconductor-metal structure. *Appl. Phys. Lett.*, **96**(25):253112 (2010).

[181] Islam, S., Li, Z., Dorgan, V. E., Bae, M. H., and Pop, E. Role of Joule Heating on Current Saturation and Transient Behavior of Graphene Transistors. *IEEE Electron Device Letters*, **34**(2):166–168 (2013).

[182] Yigen, S., Tayari, V., Island, J. O., Porter, J. M., and Champagne, A. R. Electronic thermal conductivity measurements in intrinsic graphene. *Phys. Rev. B*, **87**(24):241411 (2013).

[183] Guilmeau, E., Berthebaud, D., Misse, P. R. N., Hébert, S., Lebedev, O. I., Chateigner, D., Martin, C., and Maignan, A. $ZrSe_3$-Type Variant of TiS_3: Structure and Thermoelectric Properties. *Chem. Mater.*, **26**(19):5585–5591 (2014).

[184] Iyikanat, F., Sahin, H., Senger, R. T., and Peeters, F. M. Vacancy Formation and Oxidation Characteristics of Single Layer TiS_3. *J. Phys. Chem. C*, **119**(19):10709–10715 (2015).

[185] Kissinger, H. E. Reaction Kinetics in Differential Thermal Analysis. *Anal. Chem.*, **29**(11):1702–1706 (1957).

[186] Voter, A. *Radiation Effects in Solids*, volume 235 (Springer, Netherlands, 2007).

[187] Kalos, M. H. and Whitlock, P. A. *Monte Carlo Methods*, volume 1 (Wiley-Interscience, New York, NY, USA, 1986).

[188] Zhang, S., Yan, Z., Li, Y., Chen, Z., and Zeng, H. Atomically Thin Arsenene and Antimonene: Semimetal‚ÄìSemiconductor and Indirect‚ÄìDirect Band-Gap Transitions. *Angew. Chem. Int. Ed.*, **54**(10):3112–3115 (2015).

[189] Akturk, O. U., Ozcelik, V. O., and Ciraci, S. Single-layer crystalline phases of antimony: Antimonenes. *Phys. Rev. B*, **91**(23):235446 (2015).

[190] Wang, G., Pandey, R., and Karna, S. P. Atomically Thin Group V Elemental Films: Theoretical Investigations of Antimonene Allotropes. *ACS Appl. Mater. Interfaces*, **7**(21):11490–11496 (2015).

[191] Xu, Y., Peng, B., Zhang, H., Shao, H., Zhang, R., and Zhu, H. First-principle calculations of optical properties of monolayer arsenene and antimonene allotropes. *ANNALEN DER PHYSIK*, **529**(4):1600152 (2017).

[192] Hsieh, D., Xia, Y., Wray, L., Qian, D., Pal, A., Dil, J. H., Osterwalder, J., Meier, F., Bihlmayer, G., Kane, C. L., Hor, Y. S., Cava, R. J., and Hasan, M. Z. Observation of Unconventional Quantum Spin Textures in Topological Insulators. *Science*, **323**(5916):919–922 (2009).

[193] Bian, G., Wang, X., Liu, Y., Miller, T., and Chiang, T.-C. Interfacial Protection of Topological Surface States in Ultrathin Sb Films. *Phys. Rev. Lett.*, 108(17):176401 (2012).

[194] Fu, L. and Kane, C. L. Time reversal polarization and a ${Z}_{2}$ adiabatic spin pump. *Phys. Rev. B*, **74**(19):195312 (2006).

[195] Kane, C. L. and Mele, E. J. ${Z}_{2}$ topological order and the quantum spin hall effect. *Phys. Rev. Lett.*, **95**(14):146802 (2005).

[196] Seo, J., Roushan, P., Beidenkopf, H., Hor, Y. S., Cava, R. J., and Yazdani, A. Transmission of topological surface states through surface barriers. *Nature*, **466**(7304):343–346 (2010).

[197] Akturk, O. U., Akturk, E., and Ciraci, S. Effects of adatoms and physisorbed molecules on the physical properties of antimonene. *Phys. Rev. B*, **93**(3):035450 (2016).

[198] Pizzi, G., Gibertini, M., Dib, E., Marzari, N., Iannaccone, G., and Fiori, G. Performance of arsenene and antimonene double-gate MOSFETs from first principles. *Nat. Commun.*, **7**:12585 (2016).

[199] Born, M. and Oppenheimer, R. Zur quantentheorie der molekeln. *Annalen der Physik*, **389**:457–484 (1927).

[200] Kohn, W. and Sham, L. J. Self-consistent equations including exchange and correlation effects. *Phys. Rev.*, **140**:A1133 (1965).

[201] Kohanoff, J. *Electronic structure calculations for solids and molecules: theory and computational methods*. Cambridge University Press (2006).

[202] Dirac, P. A. Note on exchange phenomena in the thomas atom. **26**:376–385 (1930).

[203] Ceperley, D. M. and Alder, B. Ground state of the electron gas by a stochastic method. *Phys. Rev. Lett.*, **45**:566 (1980).

[204] Perdew, J. P., Parr, R. G., Levy, M., and Balduz Jr, J. L. Density-functional theory for fractional particle number: derivative discontinuities of the energy. *Phys. Rev Lett.*, **49**:1691 (1982).

[205] Seidl, A., Görling, A., Vogl, P., Majewski, J., and Levy, M. Generalized kohn-sham schemes and the band-gap problem. *Phys. Rev. B*, **53**:3764 (1996).

[206] Becke, A. D. Density-functional thermochemistry. iii. the role of exact exchange. *The Journal of chemical physics*, **98**(7):5648–5652 (1993).

[207] Perdew, J. P., Ernzerhof, M., and Burke, K. Rationale for mixing exact exchange with density functional approximations. *The Journal of Chemical Physics*, **105**(22):9982–9985 (1996).

[208] Ashcroft, N. W. Nd mermin solid state physics. *Saunders College, Philadelphia*, page 120 (1976).

[209] Ernzerhof, M. and Scuseria, G. E. Assessment of the perdew–burke–ernzerhof exchange-correlation functional. *The Journal of chemical physics*, **110**(11):5029–5036 (1999).

[210] Adamo, C. and Barone, V. Toward reliable density functional methods without adjustable parameters: The pbe0 model. *The Journal of chemical physics*, **110**(13):6158–6170 (1999).

[211] Evangeli, C., Gillemot, K., Leary, E., González, M. T., Rubio-Bollinger, G., Lambert, C. J., and Agrait, N. Engineering the Thermopower of C60 Molecular Junctions. *Nano Lett.*, **13**(5):2141–2145 (2013).

[212] Rincón-García, L., Ismael, A. K., Evangeli, C., Grace, I., Rubio-Bollinger, G., Porfyrakis, K., Agrait, N., and Lambert, C. J. Molecular design and control of fullerene-based bi-thermoelectric materials. *Nat. Mater.*, **15**(3):289–293 (2016).

[213] Groenendijk, D. J., Buscema, M., Steele, G. A., Michaelis de Vasconcellos, S., Bratschitsch, R., van der Zant, H. S. J., and Castellanos-Gomez, A. Photovoltaic and Photothermoelectric Effect in a Double-Gated WSe2 Device. *Nano Lett.*, **14**(10):5846–5852 (2014).

[214] Ovsyannikov, S. V., Shchennikov, V. V., Cantarero, A., Cros, A., and Titov, A. N. Raman spectra of (PbS)1.18(TiS2)2 misfit compound. *Mater. Sci. and Eng.: A*, **462**(1,Äì2):422–426 (2007).

[215] Krauss, T. D. and Wise, F. W. Coherent Acoustic Phonons in a Semiconductor Quantum Dot. *Phys. Rev. Lett.*, **79**(25):5102–5105 (1997).

[216] Krauss, T. D. and Wise, F. W. Raman-scattering study of exciton-phonon coupling in PbS nanocrystals. *Phys. Rev. B*, **55**(15):9860–9865 (1997).

[217] Smith, A. J., Meek, P. E., and Liang, W. Y. Raman scattering studies of SnS_2 and $SnSe_2$. *J. Phys. C: Solid State Phys.*, **10**(8):1321 (1977).

[218] Price, L. S., Parkin, I. P., Hardy, A. M. E., Clark, R. J. H., Hibbert, T. G., and Molloy, K. C. Atmospheric Pressure Chemical Vapor Deposition of Tin Sulfides (SnS, Sn_2s_3, and SnS_2) on Glass. *Chem. Mater.*, **11**(7):1792–1799 (1999).

[219] Wang, C., Tang, K., Yang, Q., and Qian, Y. Raman scattering, far infrared spectrum and photoluminescence of SnS2 nanocrystallites. *Chem. Phys. Lett.*, **357**(5-6):371–375 (2002).

[220] Kang, J.-G., Lee, G.-H., Park, K.-S., Kim, S.-O., Lee, S., Kim, D.-W., and Park, J.-G. Three-dimensional hierarchical self-supported multi-walled carbon nanotubes/tin(IV) disulfide nanosheets heterostructure electrodes for high power Li ion batteries. *J. Mater. Chem.*, **22**(18):9330–9337 (2012).

[221] First- and second-order Raman spectra of galena (PbS). *J. of Appl. Phys.*, **92**(8):4375–4380 (2002).

[222] Mehner, H. Ḿossbauer Investigations on Minerals of the Franckeite - Cylindrite Group. *Hyperfine Interactions*, **112**(1-4):239–243 (1998).

[223] Hernandez, Y., Nicolosi, V., Lotya, M., Blighe, F. M., Sun, Z., De, S., McGovern, I. T., Holland, B., Byrne, M., Gun'Ko, Y. K., Boland, J. J., Niraj, P., Duesberg, G., Krishnamurthy, S., Goodhue, R., Hutchison, J., Scardaci, V., Ferrari, A. C., and Coleman, J. N. High-yield production of graphene by liquid-phase exfoliation of graphite. *Nat. Nanotechnol.*, **3**(9):563–568 (2008).

[224] Coleman, J. N. and et. al. Two-Dimensional Nanosheets Produced by Liquid Exfoliation of Layered Materials. *Science*, **331**(6017):568–571 (2011).

[225] Shen, J., He, Y., Wu, J., Gao, C., Keyshar, K., Zhang, X., Yang, Y., Ye, M., Vajtai, R., Lou, J., and Ajayan, P. M. Liquid Phase Exfoliation of Two-Dimensional Materials by Directly Probing and Matching Surface Tension Components. *Nano Lett.*, **15**(8):5449–5454 (2015).

[226] Zeng, H. and Cui, X. An optical spectroscopic study on two-dimensional group-VI transition metal dichalcogenides. *Chem. Soc. Rev.*, **44**(9):2629–2642 (2015).

[227] Zhang, W., Huang, J.-K., Chen, C.-H., Chang, Y.-H., Cheng, Y.-J., and Li, L.-J. High-Gain Phototransistors Based on a CVD MoS_2 Monolayer. *Adv. Mater.*, **25**(25):3456–3461 (2013).

[228] Engel, M., Steiner, M., and Avouris, P. Black Phosphorus Photodetector for Multispectral, High-Resolution Imaging. *Nano Lett.*, **14**(11):6414–6417 (2014).

[229] Castellanos-Gomez, A. Black Phosphorus: Narrow Gap, Wide Applications. *J. Phys. Chem. Lett.*, **6**(21):4280–4291 (2015).

[230] Buscema, M., Groenendijk, D. J., Steele, G. A., Zant, H. S. J. v. d., and Castellanos-Gomez, A. Photovoltaic effect in few-layer black phosphorus PN junctions defined by local electrostatic gating. *Nature Communications*, **5**:4651 (2014).

[231] Youngblood, N., Chen, C., Koester, S. J., and Li, M. Waveguide-integrated black phosphorus photodetector with high responsivity and low dark current. *Nat. Photon.*, **9**(4):247–252 (2015).

[232] Haraldsen, H., Kjekshus, A., Rost, E., and Steffensen, A. On the properties of TiS_3, ZrS_3, and HfS_3. *Acta Chem. Scand.*, **17**:1283–1292 (1963).

[233] Basu, S. K., Wakihara, M., and Taniguchi, M. Thermal analysis and kinetics of the oxidation of vanadium and titanium sulfides. *Thermochimica Acta*, **92**:223–226 (1985).